QUANTIFYING THE IMPACT OF COMPLEX PORE AND GRAIN STRUCTURES ON ESTIMATION OF HYDROCARBON SATURATION USING ELECTRICAL RESISTIVITY AND DIELECTRIC PERMITTIVITY MEASUREMENTS

A Dissertation

by

HUANGYE CHEN

Submitted to the Office of Graduate and Professional Studies of
Texas A&M University
in partial fulfillment of the requirements for the degree of

DOCTOR OF PHILOSOPHY

Chair of Committee,	Zoya Heidari
Committee Members,	Yuefeng Sun
	Yalchin Efendiev
	Eduardo Gildin
Head of Department,	Daniel Hill

May 2016

Major Subject: Petroleum Engineering

ABSTRACT

Complex rock composition and pore geometry, as well as anisotropic behavior and heterogeneity, can significantly affect formation electrical resistivity and dielectric permittivity, which are used to estimate *in situ* petrophysical properties, such as water/hydrocarbon saturation. The main research topic of this dissertation is to quantify the impact of complex pore and grain structures on electrical resistivity and dielectric permittivity measurements of rock samples. Through the quantification of these impacts, this dissertation proposes a new dielectric permittivity model and a joint interpretation model (combining dielectric permittivity and electrical resistivity measurements) to improve the assessment of petrophysical properties of formations such as water/hydrocarbon saturation. In addition to the main research topic, this dissertation also designs and conducts laboratory experiments to quantify the impact of water-filled porosity and salinity on the dielectric permittivity of brine-saturated rocks.

In this dissertation, pore-scale numerical simulations are implemented to estimate the effective electrical resistivity and dielectric permittivity of rock samples. Then, diffusive directional tortuosity, directional connectivity, and electrical directional tortuosity are introduced and applied to quantify the impact of pore and grain structures in rock samples on electrical resistivity and dielectric permittivity measurements. In the case of organic-rich mudrocks, the impacts of mature kerogen and pyrite networks are also quantified on electrical resistivity and dielectric permittivity of the rocks. The two proposed models in this dissertation, a new dielectric permittivity model and a joint interpretation model, take into account the spatial distribution of rock components and can provide more reliable estimation of water/hydrocarbon saturation in both conventional and unconventional formations when compared to conventional models such as the Complex Refractive Index Model. It is observed that formation water salinity affects the sensitivity of effective electrical resistivity to the connectivity of conductive components, as well as the sensitivity of dielectric permittivity to water-filled porosity. Experimental results showed that the impact of water salinity on high-frequency dielectric permittivity of brine-saturated rocks needs to be taken into account in the interpretation of dielectric permittivity measurements, especially for rock samples with water-filled porosity of higher than 15%. Overall, the outcomes of this dissertation improve the interpretation of electrical resistivity and dielectric permittivity measurements for reliable assessment of water/hydrocarbon saturation.

DEDICATION

To my parents, for continuously encouraging and inspiring me to pursue my dream

To my love, Zheng Gan, for his patience, unconditional love and support

ACKNOWLEDGEMENTS

First and foremost, I would like to thank my beloved parents for their unconditional love, encouragement, and support for my whole life, and I thank my husband for his deep love, meticulous care, and support since the first day we met. Without them, I couldn’t finish this journey.

I am deeply grateful to my advisor, Dr. Zoya Heidari, whose consistent encouragement and invaluable guidance enabled me to develop a deep understanding of the subject and finally finish my PhD dissertation. I would like to express my sincere appreciation to Dr. Yuefeng Sun, Dr. Yalchin Efendiev, and Dr. Eduardo Gildin for serving as my dissertation defense committee members. I also would like to thank Dr. Walter Ayers for his recommendation letters for my three scholarships, 2014 SPWLA Vicki King Memorial Scholarship, 2014 Unconventional Resources Special Interest Group Scholarship and 2015 SPWLA Foundation Scholarship.

I am grateful to Gia Alexander for her professional editorial inputs for my research publications. Her comments and feedback on my technical writing are very valuable and greatly appreciated. I would like to thank all of my friends and research teammates at Texas A&M University for their help and support, especially my co-authors, Nikhil Kethireddy, Gama Firdaus, and Chi Lu. I appreciate my co-authors’ technical contributions to my publications.

I spent one summer as an intern in the R&D department at Aramco Services Company, which expanded my skills and knowledge in ways that improved my research ability. For that, I am very grateful to my mentor, Dr. Jinhong Chen, and to my team leader, Dr. Daniel Georgi. I also would like to acknowledge W.D.Von Gonten Laboratories where I conducted my NMR and dielectric measurements.

Lastly, I would like to express my gratitude to my financial sponsors. My PhD research work was funded by the Texas A&M University Joint Industry Research Program on Multi-Scale Formation Evaluation and jointly sponsored by Aramco Services Company, BHP Billiton, BP, Chevron, ConocoPhillips, and Devon Energy, as well as the Crisman Institute for Petroleum Research at the Harold Vance Department of Petroleum Engineering.

TABLE OF CONTENTS

Page

LIST OF TABLES

LIST OF FIGURES

CHAPTER I

INTRODUCTION

This dissertation introduces a theoretical and computational quantification method to characterize the complexity of pore/grain structure and rock fabric and quantify the impact of theses on electrical resistivity and dielectric permittivity measurements for both conventional and unconventional formations. In order to improve the assessment of water/hydrocarbon saturation by taking into account complex pore/grain structure and rock fabric, a new dielectric permittivity model and a joint interpretation model (combining both dielectric permittivity and electrical resistivity measurements) are developed by incorporating the aforementioned rock structure impacts. Besides quantifying the impact of rock component structure on electrical resistivity and dielectric permittivity measurements, laboratory dielectric permittivity measurements are also carried out to investigate the impact of salinity and water-filled porosity on dielectric permittivity measurements of carbonate/ sandstone samples. In summary, this doctoral research could potentially improve the interpretation of electrical resistivity and dielectric permittivity measurements for more reliable assessment of water/hydrocarbon saturation.

1.1 Background

Electrical resistivity and dielectric permittivity measurements are widely used to assess the *in situ* petrophysical properties of formations, such as hydrocarbon/water saturation. However, complex pore and grain structures impact electrical resistivity and dielectric permittivity such that the existing interpretation method might not be reliable. Therefore, to accurately estimate hydrocarbon reserves in complex formations, investigation of the impact of complex pore and grain structures on electrical resistivity and dielectric permittivity is crucial.

1.1.1 Impact of pore and grain structures on electrical resistivity

Electrical resistivity measurements are used to classify lithology, specify fluid type, and assess water/hydrocarbon saturation (Schlumberger, 1972, 1974; Doveton, 1994). Resistivity-porosity-saturation models, such as Archie's (Archie, 1942), Dual-Water (Clavier et al., 1984), and Waxman-Smits (Waxman and Smits, 1968), correlate borehole electrical resistivity measurements to pore-scale petrophysical properties in conventional reservoirs. However, interpretation of electrical resistivity is challenging and involves significant uncertainty in complex formations. For instance, due to the digenetic processes of sedimentary rocks, such as compaction, dissolution, and cementation, there exist complex pore and grain structures in carbonate and organic-rich mudroks formations (Moore, 2001; Crutis et al., 2010).

Previous publications reported the influence of heterogeneity and anisotropy on electrical resistivity measurements in conventional reservoirs (Ellis et al. 2010; Garing et al. 2014; Jouniaux et al. 2006; Nabawy et al. 2010; Winsauer et al. 1952). Ellis et al. (2010) showed that the ratio between vertical and horizontal electrical resistivity can be as high as 5:1 in some conventional formations. Garing et al. (2014) showed that micrometer- to centimeter-scale heterogeneities strongly influence electrical resistivity measurements, which creates to uncertainty in estimating water/hydrocarbon saturation when using conventional interpretation models. Verwer et al. (2011) indicated that, in addition to porosity, the combined effect of micro-porosity, pore network complexity, macro-pore pore size, and absolute number of pores all influence for electrical resistivity measurements. Samples with small pores and an intricate pore network have a low Archie's cementation factor, m, whereas those with large pores and a simple pore network have higher values and those with separate-vug porosity, have the highest values (Verwer et al., 2011). Bae et al. (2006) investigated the effect of macro-pores on electrical resistivity behavior in a heterogeneous porosity system and report that the increase of vulgarity (vug percentage in the pores) increases Archie's cementation exponent, m, and saturation exponent, n. In the case of organic-rich mudrocks, heterogeneity and anisotropy affect the physical properties obtained from well logs even more significantly. Therefore, when interpreting electrical resistivity logs, failure to consider the spatial distribution of complex pore structures can introduce significantly uncertainty in well-log-based petrophysical evaluation of complex formations.

In addition to complex pore structure, the impact of other conductive components in complex formations, such as organic-rich mudrocks, has not been quantified yet. Wei (2005) showed that aromaticity and aromatic cluster size are increased as the thermal maturity of kerogen increases through solid-state nuclear magnetic resonance (NMR) measurement. As the kerogen's aromaticity increases, the accumulation of delocalization electrons around aromatic clusters of kerogen can lead to conductive behavior of the kerogen. Kethireddy et al. (2014) showed that an increase in volumetric concentration of kerogen decreases the total resistivity of organic-rich mudrocks. However, the impact of the connectivity of conductive components, such as kerogen, on electrical resistivity measurements has not yet been investigated. Likewise, the influence of pyrite network connectivity has not been quantified, especially in cases such as the Woodford shale, where the layered distribution of pyrite is dominant.

1.1.2 Impact of pore and grain structures on dielectric permittivity

In addition to electrical resistivity measurements, dielectric permittivity measurements have become attractive candidates for assessment of water and hydrocarbon saturation in organic-rich mudrocks and carbonate formations. Dielectric permittivity of rocks is defined as the ability of rocks to store electrical charge. Dielectric permittivity of rock-fluid systems is sensitive to water-filled porosity, especially in a high frequency range (e.g., GHz frequency range) because of the higher dielectric permittivity of water compared to other rock matrix components. In order to estimate fluid saturation, several studies have been previously conducted on interpreting the dielectric property of the porous medium (Calvert and Wells, 1977; Wharton et al., 1980; Dahlberg and Ference, 1984). Among previously published techniques, the Complex Refractive Index Model (CRIM) has been a widely used in the industry (Birchak et al., 1974; Dobson et al., 1985; Heimovaara et al., 1994). However, the applicability of CRIM is limited, as it oversimplifies pore structure and neglects geometrical distribution of rock components. Stroud et al. (1988) proposed an analytical model by taking into account the impact of grain geometry in interpretation of dielectric permittivity. They developed an analytical model for a family of brine-saturated rocks for which the contacting area of neighboring grains is negligible compared to the grain surface area. Feng and Sen (1985) also provided a geometry-dependent dielectric permittivity model for partially saturated rocks by assuming ideal shapes for grains, such as spherical and platy grains. Myers et al. (1996) introduced a pore-geometry-dependent dispersion model to improve the volumetric method, which assimilates the impact of vugs and interconnected pore space on rock dielectric permittivity. Seleznev et al. (2006) developed a dispersion dielectric model by incorporating textural characteristics (e.g., aspect ratio of grains and pores). However, they did not take into account spatial distribution, tortuosity, or connectivity of the pore and grain networks in their model. Therefore, a new interpretation method, especially a pore-scale model, is needed for better investigation of petrophysical properties of complex formations.

1.1.3 Impact of salinity on dielectric permittivity measurements

Not only are dielectric permittivity measurements influenced by pore/grain structure and water-filled porosity, they are also impacted by salinity, which needs to be taken into account in interpreting these measurements. Myer (1991) showed that dielectric permittivity is salinity and frequency dependent in a low measurement frequency domain (<0.5GHz). Rankin et al. (1985) discussed the effect of clay and salinity on the dielectric properties of sand-clay mixtures and consolidated sandstone. They showed that the increment of salinity increases crystallization, which leads to a decrease in dielectric constant. Wu et al. (2015) measured the dielectric properties of saline soil and develop an improved conventional dielectric model by taking into account salinity in the C-band frequency range (i.e., 4 to 8 GHz). Hizem et al. (2008) showed that dielectric permittivity is independent of salinity at 1-GHz frequency. However, for all the previous studies, the impact of water-filled porosity on the sensitivity of dielectric permittivity to water salinity or to critical frequency (where the dielectric permittivity measurement is independent of salinity) was not quantified. Therefore, dielectric permittivity measurements of saturated rocks corresponding to different frequencies, water-filled porosity, and salinity need to be conducted to quantify their impacts for the reliable assessment of petrophysical properties.

1.2 Statement of Problem

Electrical resistivity and dielectric permittivity measurements are typical methods for assessing *in situ* and real-time petrophysical properties of formations, such as hydrocarbon/water saturation. However, complex pore geometry and composition, as well as anisotropy and heterogeneity, impact electrical resistivity and dielectric permittivity, presenting a big challenge for interpretation methods. Thus, characterization of complex pore and grain structure at the pore scale is necessary to accurately predict hydrocarbon reserve in complex formations.

Conventional methods for interpreting electrical resistivity include resistivity-porosity-saturation models, such as Archie's equation (Archie, 1942), and shaly sand models, such as the Dual-Water model (Clavier et al., 1984) and the Waxman-Smits model (Waxman and Smits, 1968). However, none of these models takes into account other conductive components of the rocks, such as pyrite and highly mature kerogen. This limitation causes uncertainty in assessment of water saturation in formations with complex matrix components. In addition to the presence of conductive components, the spatial distribution of the conductive pathway (saline water, kerogen, and pyrite) can also impact electrical resistivity measurements. Several studies have been conducted to investigate the influence of heterogeneity and anisotropy on electrical resistivity measurements in conventional reservoirs (Ellis et al. 2010; Garing et al. 2014; Jouniaux et al. 2006; Nabawy et al. 2010; Winsauer et al. 1952). Ellis et al. (2010) showed that the ratio between vertical and horizontal electrical resistivity can be as high as 5:1 in some conventional formations. Compared to the conventional formation, heterogeneity and anisotropy can be even more significant in organic-rich mudrocks. Therefore, the impact of spatial distribution of conductive rock components on electrical resistivity measurements needs to be studied and quantified.

In addition to electrical resistivity measurements, dielectric permittivity measurements have become attractive candidates for assessing hydrocarbon/water saturation in formations with complex structure, such as organic-rich mudrock and carbonate formations. Compared with electrical resistivity measurement that is affected by all conductive components, dielectric permittivity measurement is more sensitive to water-filled porosity, especially in the high frequency range (e.g., GHz frequency range), due to the high dielectric permittivity of water (usually one order of magnitude higher than the other rock matrix components). Conventional methods to analyze dielectric permittivity include the volumetric model (Calvert and Wells, 1977; Dahlberg and Ference, 1984; Linde et al., 2006; Wharton et al., 1980), Stroud-Milton-De (SMD) (Stroud et al., 1986), and CRIM (Feng and Sen, 1985; Pirrone et al., 2011). However, interpretation of dielectric measurements can still be challenging because none of these models takes into account the impact of complex pore structure and spatial distribution of rock components. As for dielectric permittivity laboratory measurements, the impact of water-filled porosity on the sensitivity of dielectric permittivity to water salinity or to critical frequency (where dielectric permittivity measurement is independent of salinity) is still not quantified, bringing uncertainty to the interpretation of dielectric permittivity measurements.

In summary, the complex spatial distributions of rock components, such as water, pyrite, and kerogen networks, significantly impact electrical resistivity and dielectric permittivity measurements. Characterizing the impact of these factors while interpreting electrical resistivity and dielectric permittivity measurements is still a challenge in the petroleum industry. This dissertation quantifies the impact of these factors on electrical resistivity and dielectric permittivity measurements. It also proposes a new dielectric permittivity model and a new joint interpretation model (through combining dielectric permittivity and electrical resistivity measurements) to improve estimates of petrophysical properties (e.g., hydrocarbon saturation) of complex formations. Furthermore, understanding the impact of salinity on dielectric permittivity measurements can assist in accurately estimating hydrocarbon/water saturation, especially for formations with high salinity. Therefore, this dissertation includes laboratory measurements of dielectric permittivity to quantify the impact of water-filled porosity on the sensitivity of dielectric permittivity to water salinity and to critical measurement frequency.

1.3 Research Objectives

This dissertation aims to quantify the impact of complex pore and grain structures on the electrical resistivity and dielectric permittivity measurements of rock samples. With the quantification of such impact, this dissertation proposes a new dielectric permittivity model and a new joint interpretation model (combining dielectric permittivity and electrical resistivity measurements) to improve the assessment of formation petrophysical properties such as water/hydrocarbon saturation. Furthermore, regarding dielectric permittivity laboratory measurements, this dissertation conducts experiments to quantify the impact of water-filled porosity and water salinity on dielectric permittivity measurements. The detailed objectives achieved in this dissertation include the following:

1) Develop numerical simulators to calculate directional tortuosity, directional connectivity of rock components to quantify the complex pore/grain structure, and heterogeneous and anisotropic properties of the rock.
2) Develop numerical simulators to calculate effective electrical resistivity and dielectric permittivity of rock samples.
3) Quantify the impact of diffusive directional tortuosity and directional connectivity of rock components on electrical resistivity and dielectric permittivity measurements.
4) Improve the assessment of hydrocarbon/water saturation through dielectric permittivity measurements by developing a structure-dependent dielectric permittivity method.
5) Propose a joint interpretation model that incorporates both electrical resistivity and dielectric permittivity measurements to better estimate hydrocarbon saturation by taking into account the impact of spatial distribution of rock components.

6) Quantify the impact of water-filled porosity on the sensitivity of dielectric permittivity to water salinity and to the critical frequency by conducting dielectric permittivity laboratory measurements on brine-saturated rock samples.

1.4 Method Overview

This section outlines the method used to pursue the aforementioned objectives. The method consists of four major steps: (1) 3D pore-scale digital rock construction; (2) effective electrical resistivity and dielectric permittivity simulation; (3) directional tortuosity and connectivity quantification; and (4) dielectric permittivity laboratory measurements. The method section in each chapter contains an explicit description of the methods applied to pursue each objective.

3D pore-scale digital images, which are obtained from X-ray Microscope or Scanning Electron Microscope (SEM), reveal the internal pore and grain structures of rock samples. In this dissertation, 3D digital sandstone and carbonate rocks are constructed from actual X-ray computed tomography (CT), and 3D digital organic-rich mudrocks are synthesized based on petrophysical parameters in actual rock samples and actual 2D pore-scale rock images.

Local electrical resistivity and dielectric permittivity are then assigned to each rock component of 3D digital rocks as inputs into the pore-scale numerical simulations. The pore-scale numerical simulations are aim to calculate the effective electrical resistivity and dielectric permittivity of rocks. The key step in these numerical simulations is to calculate the distribution of the electrical potential field by solving the Laplace's equation.

Next, three quantitative factors, diffusive directional tortuosity, directional connectivity, and electrical directional tortuosity, are introduced and calculated to quantify the complexity of pore and grain structures of these digital rock samples. Through dielectric permittivity simulation and diffusive directional tortuosity calculation, a new dielectric permittivity interpretation model that incorporates diffusive directional tortuosity is proposed and used to better estimate water/hydrocarbon saturation. Furthermore, through electrical resistivity/dielectric permittivity simulation and electrical directional tortuosity calculation, a joint interpretation model that combines the electrical resistivity and dielectric permittivity measurements is proposed and used to improve the accuracy in estimates of water/hydrocarbon saturation.

Lastly, actual dielectric permittivity measurements are conducted to investigate the impact of salinity on the dielectric permittivity of the brine-saturated rocks. During the laboratory measurements, NMR, an impedance network analyzer, vacuum pressure/core flood systems, and a centrifuge were used. The experiment procedures include preparation of fully and partially bine-saturated rock samples, water-filled porosity measurements, and high-frequency dielectric permittivity measurements.

1.5 Outline of Dissertation

This dissertation has six chapters, including the present introductory chapter and the final summary and recommendation chapter. Chapter I includes the research background, research objectives, and methods. The following main body of the dissertation covers five parts.

Chapter II introduces a method to quantify the directional tortuosity and connectivity of rock matrix constituents and applies this method to investigate the heterogeneous and anisotropic properties of the rock samples using 3D pore-scale images. Correlations between directional connectivity of rock components and electrical resistivity of organic-rich mudrocks are investigated to better understand the conductive mechanism in organic-rich mudrocks. Fluid saturation estimation using the conventional method is provided to confirm the importance of anisotropy and directional connectivity of conductive rock components for assessing hydrocarbon saturation of organic-rich mudrocks.

Chapter III investigates the complexity of pore and grain structure on dielectric permittivity measurements and develops a new dielectric permittivity model to better estimate water-filled porosity. A diffusive directional tortuosity factor is calculated from the 3D pore-scale rock images to quantify the geometry and spatial distribution of the pore and grain network. The introduced new permittivity model is applied to sandstone, carbonate, and organic-rich mudrocks to estimate fluid saturation. The results are compared with the ones obtained from the CRIM.

Chapter IV introduces an analytical method, which is a joint interpretation of electrical resistivity and dielectric permittivity measurements, for a better estimate of water-filled porosity and hydrocarbon saturation. 3D pore-scale numerical simulation of electrical resistivity and dielectric permittivity is conducted on both conventional sandstone and unconventional organic-rich mudrocks. The application of this joint method significantly enhances water-filled porosity prediction in comparison with the conventional method of CRIM.

Chapter V focuses on the laboratory dielectric permittivity measurements and investigates the impact of water salinity on the high-frequency dielectric permittivity measurements of brine-saturated rocks. Core-flood and vacuum pressure systems are used to saturate rock samples, and NMR and an impedance network analyzer are used to measure water-filled porosity and dielectric permittivity of the bine-saturated rock samples. It discusses the impact of water-filled porosity on the sensitivity of dielectric permittivity to water salinity. In addition, it introduces the definition of critical frequency at which interfacial polarization is negligible and discusses the impact of water-filled porosity and salinity on this critical frequency.

Finally, Chapter VI presents the summary and conclusions of the dissertation and provides recommendations regarding the future research.

1.6 List of Publications

Below is a list of journal and conference papers that have been published or submitted for review as a result of this dissertation research.

1.6.1 Refereed journal papers

Chen, H. and Heidari, Z. (2016). Impact of water salinity on high-frequency dielectric measurements in brine-saturated rocks. Submitted to Water Resource Research.

Chen, H. and Heidari, Z., (2016). Pore-scale joint evaluation of dielectric permittivity and electrical resistivity for assessment of hydrocarbon saturation using numerical simulations. Preprint, SPE Journal.

Chen, H. and Heidari, Z. (2015). Quantifying the directional connectivity of rock constituents and its impact on electrical resistivity measurement of organic-rich mudrocks. Mathematical Geosciences: DOI 10.1007/s11004-015-9595-9, April 28.

Chen, H. and Heidari, Z. (2014). Pore-scale evaluation of dielectric permittivity of rock-fluid mixture with complex pore and grain structures. Petrophysics 55(6): 587-597.

1.6.2 Refereed conference papers

Chen, H. and Heidari, Z. (2015). Impact of water salinity on high-frequency dielectric measurements in rock-fluid mixtures. Presented at SPWLA 56th Annual Well Logging Symposium, Long Beach, California, July 18-22, 2015.

Chen, H. and Heidari, Z. (2014). Assessment of hydrocarbon saturation in organic-rich source rocks using combined Interpretation of dielectric and electrical resistivity measurements. SPE 170973. Presented at SPE Annual Technical Conference and Exhibition held in Amsterdam, the Netherlands, October 27-29.

Chen, H. and Heidari, Z. (2014). Pore-scale evaluation of dielectric measurements in formations with complex pore and grain structures. Presented at SPWLA 55th Annual Well Logging Symposium, Abu Dhabi, May 18-22.

Chen, H., Firdaus, G., and Heidari, Z. (2014). Impact of anisotropic nature of organic-rich source rocks on electrical resistivity measurements. Presented at SPWLA 55th Annual Logging Symposium, Abu Dhabi, May 18-22.

CHAPTER II

QUANTIFYING THE DIRECTIONAL CONNECTIVITY OF MATRIX CONSTITUENTS AND ITS IMPACT ON ELECTRICAL RESISTIVITY OF ORGANIC-RICH MUDROCKS

Quantifying the hydrocarbon transport mechanism in organic-rich mudrocks is still a challenge. Scientific consensus holds that the directional connectivity of organic matter within organic-rich mudrocks significantly affects production in such unconventional reservoirs. Furthermore, the directional connectivity of matrix constituents has a significant impact on the physical properties of organic-rich mudrocks such as electrical resistivity. The latter causes a significant uncertainty in assessment of petrophysical properties such as hydrocarbon saturation. A quantitative approach is, however, required to improve formation evaluation of organic-rich mudrocks. This chapter first introduces a method to quantify directional connectivity of the matrix constituents. Electrical resistivity of three-dimensional pore-scale rock images is then numerically simulated using the finite difference method. The results of numerical simulations for synthetic organic-rich mudrocks with different levels of directional connectivity of kerogen network confirm that (a) the presence of conductive mature kerogen can significantly impact the electrical resistivity of the rock in different directions and the corresponding estimates of fluid saturations and (b) the directional connectivity of the kerogen network has a measurable impact on electrical resistivity of rocks. The synthetic examples, including pyrite, confirm that pyrite's presence and its directional connectivity affect electrical resistivity of rocks even in a low concentration (e.g. 4 vol%). Neglecting the presence of conductive kerogen and pyrite can result in up to a 17.9% and 23% overestimate in water saturation, respectively. The results show up to 31% and 37% variation in electrical resistivity caused by variation in directional connectivity (i.e., ranging from dispersed to layered distribution) of kerogen and pyrite networks, respectively. Furthermore, a measurable difference is observed in the effective electrical resistivity of organic-rich mudrocks between horizontal and vertical directions. Finally, the results confirm the importance of taking into account anisotropy and directional connectivity of conductive rock components for enhanced assessment of hydrocarbon saturation in organic-rich mudrocks.

2.1 Introduction

Electrical resistivity logs are typically used for assessment of fluid saturations in conventional reservoirs. Resistivity-porosity-saturation models, such as Archie's (Archie 1942), Dual-Water (Clavier et al. 1984) and Waxman-Smits (Waxman and Smits 1968), correlate borehole electrical resistivity measurements to pore-scale petrophysical properties in conventional reservoirs. All the conventional resistivity-porosity-saturation models assume that water is the only conductive component of the rock-fluid mixtures. Connectivity of the water network has been considered in the aforementioned models using empirical constants. In the case of organic-rich mudrocks, however, highly mature conductive kerogen and pyrite affect borehole electrical resistivity measurements.

Passey et al. (2010) noted that in highly mature shale-gas reservoirs, the overall electrical resistivity can be 1 to 2 orders of magnitude less than that measured in the same formation at relatively lower thermal maturities. Current scientific consensus held that formation of intermediary compounds in highly mature organic matter at high temperatures may contribute to the increase of electrical conductivity in addition to the presence of formation water, clay and pyrite (Passey et al., 2010). Although several publications documented the conductive behavior of organic matter at high temperature (Li et al., 2007; Mao et al., 2010; Rajeshwar et al., 1980), the correlation among maturity, temperature, chemical structure and electrical properties of organic matter has not been quantified.

Kethireddy et al. (2014) showed that conventional resistivity-porosity-saturation models underestimate hydrocarbon saturation by 20% to 40% in the zones with high volumetric concentration of kerogen. The same work quantified the impact of kerogen concentration and electrical conductivity on electrical resistivity of organic-rich mudrocks. The reported results suggested that not only the volumetric concentration but also the connectivity of the kerogen network affect electrical resistivity measurements. However, the impact of the connectivity of the conductive components, such as kerogen, on electrical resistivity measurements has not yet been investigated. Likewise, the influence of pyrite network connectivity has not been considered in conventional resistivity-porosity-saturation models. Previous research has established that the impact on electrical resistivity of pyrite-bearing rocks is negligible in the presence of a small volumetric concentration of pyrite. Although this assumption could be correct in dispersed or local distribution of pyrite, the impact of pyrite cannot be neglected in the cases such as the Woodford shale, where the layered distribution of pyrite is dominant.

Additional publications investigated the influence of heterogeneity and anisotropy on electrical resistivity measurements in conventional reservoirs (Ellis et al., 2010; Garing et al., 2014; Jouniaux et al., 2006; Nabawy et al., 2010; Winsauer et al., 1952). Ellis et al. (2010) showed that the ratio between vertical and horizontal electrical resistivity can be as high as 5:1 in some conventional formations. In the case of organic-rich mudrocks, heterogeneity and anisotropy can significantly affect the physical properties obtained from well logs, which are used to estimate the hydrocarbon reserves. Therefore, in interpretation of electrical resistivity logs, failure to consider the spatial distribution of conductive rock components can cause large uncertainty in well-log-based petrophysical evaluation for both horizontal and vertical wells.

This chapter uses directional connectivity factor that incorporates diffusive directional tortuosity to quantify network connectivity and distribution of desired rock components (e.g., formation water, kerogen, and pyrite) for any given porous media. The next step includes quantifying the impact of directional connectivity (i.e., dispersed vs. layered) of kerogen and pyrite on electrical resistivity of organic-rich mudrocks. The following sections describe the method and its application to organic-rich mudrocks in two synthetic examples. The results include (a) estimates of the directional connectivity of conductive matrix components, (b) quantifying the impact of the directional connectivity of kerogen and pyrite on electrical resistivity of organic-rich mudrocks, (c) quantifying anisotropic properties of the rocks by calculating the directional connectivity of conductive matrix components and directional electrical resistivity of the rock in both horizontal and the vertical directions, and (d) quantifying the impact of the directional connectivity of conductive matrix components on electrical resistivity in both horizontal and vertical directions, and, consequently, on the accuracy of water saturation assessment if conventional resistivity-porosity-saturation methods are applied.

Section 2.2 introduces the method used in this chapter. Section 2.3 presents the results of the model application on synthetic organic-rick mudrocks including kerogen and pyrite, and discusses the impact of spatial distribution of kerogen and pyrite on the measurement of effective electrical resistivity.

2.2 Method

This section describes the method for investigating the impact of spatial distribution of conductive matrix components on estimates of water-filled porosity from electrical resistivity measurements. It introduces how to construct synthetic digital organic-rich mudrocks and the assumed petrophysical model, define diffusive directional tortuosity of a spatial network, and explains how to calculate diffusive directional tortuosity based on 3D pore-scale digital rock images. The directional connectivity is defined, which incorporates three main parameters: (a) the number of connected clusters of a particular conductive rock component, (b) the volumetric concentration of each connected conductive cluster, and (c) the diffusive directional tortuosity of each connected conductive cluster. Finally, the numerical simulation, which is used to calculate the effective electrical resistivity of porous media, is described, and the workflow showing how to investigate complexities of spatial distribution of a rock matrix and their impact on interpretation of electrical resistivity measurements, is summarized.

2.2.1 Digital rock samples

In this dissertation, 3D digital pore-scale images of rock samples are inputs to the numerical simulators. Every cubic voxel of the images represents either some rock matrix constituent or pore space. The 3D digital image is converted into a 3D grid structure where the grid size is the resolution of the image (e.g., 10nm for the synthetic organic-rich mudrocks used in this dissertation). After implementing numerical grids to the rock images, the local physical properties (e.g., electrical conductivity and dielectric permittivity) of the rocks are assigned to each grid. In this chapter, the 3D digital organic-rich mudrocks are synthesized based on petrophysical parameters in actual rock samples and actual 2D pore-scale FIB-SEM (Focused Ion Beam Scanning Electron Microscope) rock images.

In order to generate the synthetic organic-rich mudrock sample, a 2D FIB-SEM digital image of organic-rich mudrock is first converted into a 2D grid of pixels. This 2D grid of pixels is treated as the starting points of a random walk algorithm to generate synthetic samples with variable spatial distribution of rock components. For instance, to generate pore networks, the number of walkers is assigned to be equal to the number of voxels representing pores in the first layer (i.e., obtained from the 2D FIB-SEM image), with set theses voxels the starting positions for the walkers. The common random walk is given equal walk probability, 1/6, to all six directions, denoted by X-, X+, Y-, Y+, Z-, and Z+ (X- means negative X direction while X+ means positive X direction, and so do the other notations). Assigning weighted probability to different directions can generate samples with variable directional connectivity of different components. The process of synthetic case generation includes following enforced constraints: (a) starting from the first layer, all the walkers are forced to take one step to the second layer; (b) the walkers in the second layer cannot travel back to the first layer; (c) the walkers in the boundary layer will travel inside the grid from the mirror position of the opposite boundary layer when they are assigned to travel out of the boundary; and (d) all the walkers will stop travelling once the assigned porosity has been reached. The same algorithm can be used to generate spatial distribution of other conductive mudrock components such as kerogen and pyrite networks.

2.2.2 Petrophysical model

Before the study of petrophysical properties of rock samples, a petrophysical model is first needed to define the petrophysical terminologies. **Figures 2.1(a)** and **2.1(b)** show the assumed petrophysical models in this dissertation for conventional sandstone and carbonate rocks and organic-rich mudrocks, respectively. In the assumed petrophysical model for organic-rich mudrocks, the total volume of hydrocarbon, the total porosity, water-filled porosity, kerogen porosity, volumetric concentration of kerogen, and volumetric concentration of pyrite are defined as

$$V_{HC} = V_{HC,k} + V_{HC,nk}, \tag{2.1}$$

$$\phi_t = \frac{V_{HC} + V_w}{V_R}, \tag{2.2}$$

$$\phi_w = \frac{V_w}{V_R}, \tag{2.3}$$

$$\phi_k = \frac{V_{HC,k}}{V_k}, \tag{2.4}$$

$$C_k = \frac{V_k}{V_R}, \tag{2.5}$$

and

$$C_P = \frac{V_P}{V_R}, \tag{2.6}$$

respectively, where $V_{HC,k}$ is the volume of hydrocarbon in the kerogen pore space, $V_{HC,nk}$ is the volume of hydrocarbon outside the kerogen pore space, V_w is the volume of water, V_R is the volume of rock, V_k is the volume of kerogen, and V_P is the volume of pyrite. In the case of carbonate and sandstone rocks there is no kerogen volume in the model.

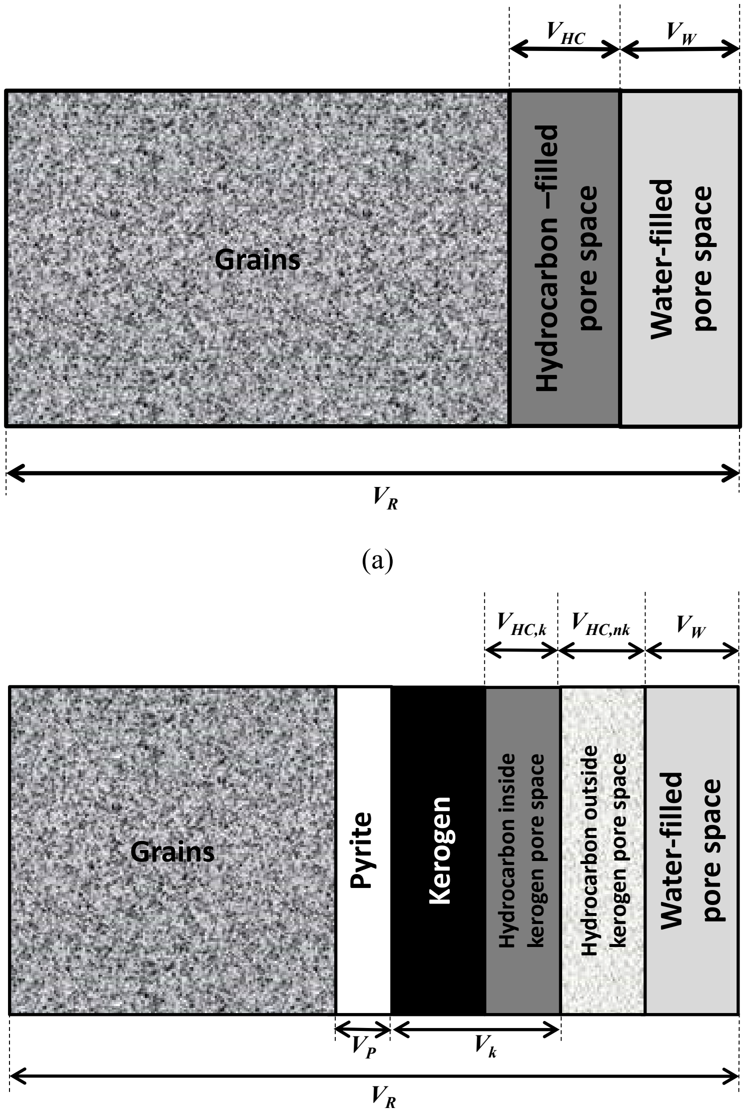

(a)

(b)

Figure 2.1: Assumed petrophysical rock models for numerical simulations of electric potential field in (a) conventional carbonate and sandstone rocks and (b) organic-rich mudrocks.

2.2.3 Diffusive directional tortuosity

The diffusive directional tortuosity of a network of rock components (e.g., water, kerogen, etc.) is defined as the ratio of the diffusion coefficient in the free space (i.e., 100% porosity) to the diffusion coefficient in the network. The basic concept of diffusion coefficients comes from the NMR measurements (Kimmich, 1997). Variable diffusive tortuosity of the pore structure in different directions can be used to quantitatively reflect the anisotropic properties of many formations (Pfleiderer and Halls, 1990; Siegesmund et al., 1991). Nakashima and Kamiya (2007) introduced an algorithm to estimate tortuosity based on pore-scale images of volcanic rocks, which is used to calculate the diffusive directional tortuosity in this dissertation.

The algorithm for the diffusive tortuosity assessment uses 3D CT-scan images as an input. The first step is to distinguish the pore space and other rock constituents and digitize the pore-scale images. The next step includes generating random walkers in each rock component (i.e., either pore space or certain mineral). To compute the diffusive tortuosity of the pore structure, random walkers are assigned inside the percolated pore space that can move around in the percolated pore space within a certain amount of time, *t*. The walkers take a random step to one of the nearest voxels and *t* is incremented by 1 after the step. If the walkers choose the solid voxel to jump, the time, *t*, still increases by 1, but the jump is not executed. When the walkers hit the boundary, they bounce back using the mirror operation rule. The same algorithm can be applied to other rock components such as pyrite and kerogen. We calculate the directional mean square displacement in the X, Y, and Z directions through

$$\langle x(t)^2 \rangle = \frac{1}{n} \sum_{i=1}^{n} (x_i(t) - x_i(0))^2, \tag{2.7}$$

$$\langle y(t)^2 \rangle = \frac{1}{n} \sum_{i=1}^{n} (y_i(t) - y_i(0))^2, \tag{2.8}$$

and

$$\langle z(t)^2 \rangle = \frac{1}{n} \sum_{i=1}^{n} (z_i(t) - z_i(0))^2, \tag{2.9}$$

where $x_i(t)$, $y_i(t)$, and $z_i(t)$ denote the position of the ith random walker in each direction at time t, and n is the number of random walkers employed in the simulation. The overall mean-square displacement is given by

$$\langle r(t)^2 \rangle = \frac{1}{n} \sum_{i=1}^{n} \left[(x_i(t) - x_i(0))^2 + (y_i(t) - y_i(0))^2 + (z_i(t) - z_i(0))^2 \right] \tag{2.10}$$

In an extreme case where we have a void cube without grains (i.e., 100% porosity), the directional mean-square displacement is given by

$$\langle x^2 \rangle_{nograin} = \langle y^2 \rangle_{nograin} = \langle z^2 \rangle_{nograin} = \frac{1}{3} \langle r^2 \rangle_{nograin}. \tag{2.11}$$

We define and calculate the diffusive tortuosity of the pore network by comparing the time derivative of displacement covered by the walkers via

$$\tilde{\tau} = \frac{l^2 dt}{d\langle r(t)^2 \rangle}, \qquad \text{as } t \to \infty \tag{2.12}$$

where $\tilde{\tau}$ is the dimensionless tortuosity factor and l is the lattice constant of the simple cubic lattice (i.e., the dimension of a cubic voxel). The diffusive directional tortuosity of rock components are defined by

$$\tilde{\tau}_x = \frac{l^2 dt}{3d\langle x(t)^2 \rangle}, \qquad \text{as } t \to \infty \qquad (2.13)$$

$$\tilde{\tau}_y = \frac{l^2 dt}{3d\langle y(t)^2 \rangle}, \qquad \text{as } t \to \infty \qquad (2.14)$$

and

$$\tilde{\tau}_z = \frac{l^2 dt}{3d\langle z(t)^2 \rangle}, \qquad \text{as } t \to \infty \qquad (2.15)$$

where $\tilde{\tau}_x$, $\tilde{\tau}_y$, and $\tilde{\tau}_z$ are the diffusive directional tortuosity along the X, Y, and Z directions, respectively. In a symmetric and isotropic media, $\tilde{\tau}_x$, $\tilde{\tau}_y$, and $\tilde{\tau}_z$ are equal to each other.

2.2.4 Directional connectivity

The directional connectivity along *i* direction (X, Y, or Z) is first introduced by this dissertation and defined as

$$\Psi_i = \sum_{j=1}^{M} \frac{C_j}{\alpha \tilde{\tau}_{j,i}^{\beta}}, \qquad (2.16)$$

where *j* is the order index for the connected clusters of some conductive component, *M* is the total number of the connected conductive clusters along *i* direction, C_j is the volumetric concentration of the *j*th connected conductive cluster, α and β are connectivity parameters, and $\tilde{\tau}_{j,i}$ is the diffusive directional tortuosity of the *j*th connected cluster of this conductive component along *i* direction. **Figure 2.2** shows the schematic description of connected clusters used in the definition of directional connectivity in **Equation 2.16**. **Figures 2.2(a)** and **2.2(b)** represent example cases with one and two connected clusters in y direction, respectively. All the connected clusters are labeled through (a) searching for the next unlabeled voxel, p; (b) using a flood-fill algorithm (Bond, 2011) to label all the voxels in the connected component containing p; and (c) repeating steps 1 and 2 until all the connected components are labeled. **Equation 2.14** is then applied on each connected cluster to calculate its tortuosity. The introduced directional connectivity is a dimensionless index, which is a function of volumetric concentration and tortuosity of each network. According to the directional connectivity index defined in **Equation 2.16**, the increase in volumetric concentration of a given component network increases the directional connectivity while the increase in directional tortuosity decreases the directional connectivity of that network. The connectivity parameters, α and β, are affected by pore structure, grain shapes and cementation.

In this chapter, for **Equation 2.16**, α and β are assumed to be 0.48 and 1, respectively, for synthetic example no. 1. For synthetic example no. 2, α and β are assumed to be equal to 0.92 and 1, respectively. These fitting parameters can be adjusted for different rock types when processing three-dimensional pore-scale rock images and applied to the entire formation. Then, the effective electrical resistivity is numerically simulated by solving the Laplace's equation which is explained in the next subsection.

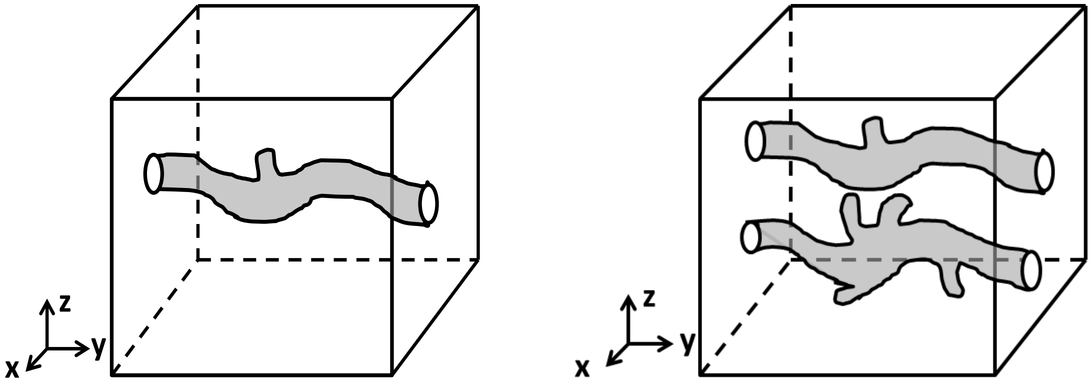

(a) (b)

Figure 2.2: The schematic diagram showing (a) one connected cluster and (b) two connected clusters along *y* direction.

2.2.5 Assessment of effective electrical resistivity using numerical simulations

For a rock sample, if the electric currents are in a steady state, the charge conservation equation is given by

$$\nabla \cdot \vec{J} = 0, \tag{2.17}$$

where $\vec{J}$ is the electric current and ∇ is the divergence operator. Using the constitution equation, $\vec{J}$ can be written as

$$\vec{J} = \sigma\vec{E}, \tag{2.18}$$

where $\vec{E}$ is the electric field and σ is the local electrical conductivity (that is, $\sigma(i, j, k)$ is the electrical conductivity for the (i, j, k) point). The electric field $\vec{E}$ can be written as

$$\vec{E} = -\nabla U, \tag{2.19}$$

where U is the electric field potential (that is, $U(i, j, k)$ is the electric potential for the (i,j,k) point). By substituting **Equations 2.18** and **2.19** into **Equation 2.17**, the charge conservation equation can be written as

$$\nabla \cdot (\sigma \nabla U) = 0, \tag{2.20}$$

which is also called the Laplace's equation.

In order to estimate the effective electrical resistivity of digital rock samples in the static potential field, the distribution of the electrical potential field is first calculated by solving the Laplace's equation using a finite difference method. **Figure 2.3** shows the mesh grid used in the finite difference method. The discretization of **Equation 2.20** is implemented via

$$\nabla \cdot (\sigma \nabla U) = \frac{\partial(\sigma \nabla U)}{\partial x} + \frac{\partial(\sigma \nabla U)}{\partial y} + \frac{\partial(\sigma \nabla U)}{\partial z} \tag{2.21}$$

where

$$\begin{aligned}\frac{\partial(\sigma \nabla U)}{\partial x} &= \frac{(\sigma(i+1,j,k)+\sigma(i,j,k))(U(i+1,j,k)-U(i,j,k))}{2\Delta x^2} \\ &- \frac{(\sigma(i-1,j,k)+\sigma(i,j,k))(U(i,j,k)-U(i-1,j,k))}{2\Delta x^2},\end{aligned} \tag{2.22}$$

$$\begin{aligned}\frac{\partial(\sigma \nabla U)}{\partial y} &= \frac{(\sigma(i,j+1,k)+\sigma(i,j,k))(U(i,j+1,k)-U(i,j,k))}{2\mathit{\Delta} y^2} \\ &- \frac{(\sigma(i,j-1,k)+\sigma(i,j,k))(U(i,j,k)-U(i,j-1,k))}{2\mathit{\Delta} y^2},\end{aligned} \tag{2.23}$$

and

$$\frac{\partial(\sigma\nabla U)}{\partial z}=\frac{(\sigma(i,j,k+1)+\sigma(i,j,k))(U(i,j,k+1)-U(i,j,k))}{2\Delta z^2}-\frac{(\sigma(i,j,k-1)+\sigma(i,j,k))(U(i,j,k)-U(i,j,k-1))}{2\Delta z^2}. \tag{2.24}$$

where $U(i, j, k)$ is the electrical potential at the grid point (i, j, k), $\sigma(i, j, k)$ is the electrical resistivity at the grid point (i, j, k), and Δx, Δy, and Δz are the grid sizes along the X, Y, and Z directions, respectively. The corresponding electrical conductivity of each rock component is assigned to the cubic voxels representing those rock components.

The boundary conditions for calculating the effective electrical resistivity along the Y direction include Dirichlet and Neumann boundary conditions, given by

$$U\big|_{Y=1}=0 \text{ and } U\big|_{Y=N}=U_0, \tag{2.25}$$

and

$$\left.\frac{\partial U}{\partial Y}\right|_{X=1,N}=0 \text{ and } \left.\frac{\partial U}{\partial Y}\right|_{Z=1,N}=0, \tag{2.26}$$

respectively. N represents the number of grids in the digitized pore-scale rock images, U_0 is the potential imposed at the last layer. Using the output of spatial distribution of electric potential, U, we can calculate the local current, $I(i,j,k)$, and the total current, I_t, via

$$I(i,j,k)=((U(i,j+1,\ k)-U(i,j,k))\cdot\frac{(\sigma(i,j+1,k)+\sigma(i,j,k))}{2} \tag{2.27}$$

and

$$I_t=\frac{1}{N}\sum_{i,j,k}I(i,j,k). \tag{2.28}$$

The effective resistivity can be finally calculated via

$$R_t = \frac{U_0}{I_t}. \tag{2.29}$$

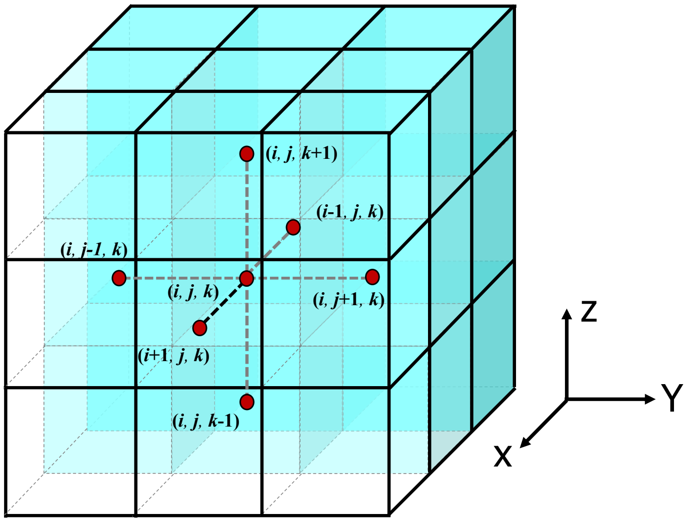

Figure 2.3: Seven-point finite difference stencil used for discretization of the Laplace's equation in a 3D domain.

2.2.6 Workflow

Figure 2.4 shows the workflow used in this chapter for the study on complexity of spatial structure of rock matrix and its impact on the interpretation of electrical resistivity measurements. Several organic-rich mudrocks with different directional connectivity are synthesized based on the real 3D pore-scale images. The electrical properties for each rock components are used as inputs into the pore-scale simulation. The numerical simulation includes (a) solving the Laplace's equation to get electrical potential distribution, and (b) using a random-walk algorithm to estimate diffusive directional tortuosity of pore and grain network in a porous medium. Next, the directional connectivity of a conductive component such as kerogen and pyrite is estimated. The relative error in estimated water saturation is used by applying the conventional Archie's method. Finally, the impact of the directional connectivity of the conductive rock components is quantified on the effective electrical resistivity of the rock, as well as the relative error in estimation of water saturation

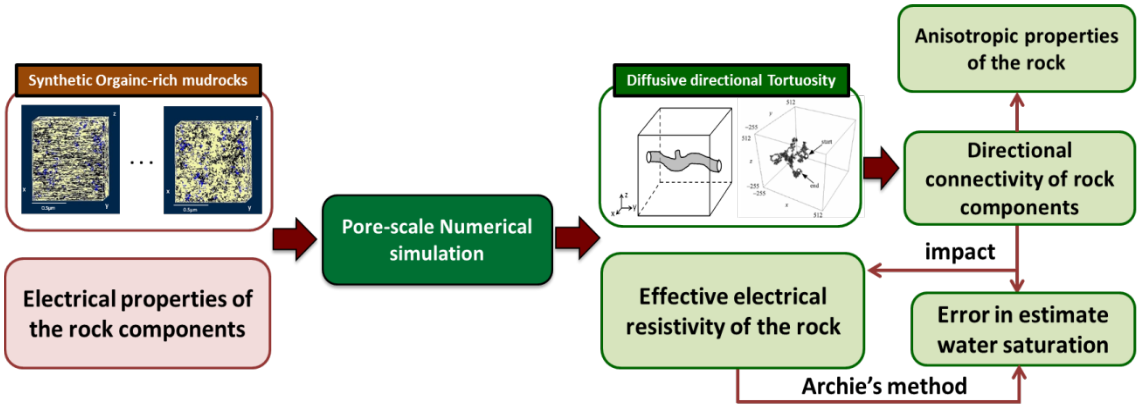

Figure 2.4: The workflow for the study on complexity of spatial structure of rock matrix and its impact on the interpretation of electrical resistivity measurements in this chapter.

2.3 Results

2.3.1 Synthetic example no. 1: spatial distribution of kerogen

In this subsection, a set of eight synthetic organic-rich mudrocks is designed to quantify the impact of directional connectivity of the kerogen network on the vertical and horizontal electrical resistivity values. To pursue our objective above, eight synthetic cases are generated with similar porosity, fluid saturation, and volumetric concentration of kerogen, but different kerogen network connectivity. Developing synthetic cases enables sensitivity analysis on directional connectivity of different matrix components in a wide range. The spatial distribution and directional connectivity of matrix components such as kerogen and pyrite can be extremely variable in organic-rich mudrocks, ranging from dispersed to parallel layers. The spatial distribution of the kerogen depends on factors such as the sedimentary deposition, organic matter maturity stages, and environment changes. For instance, a dispersed distribution of kerogen and a layered distribution of kerogen are often observed in the Haynesville shale and in the Woodford shale, respectively. The synthetic cases are developed based on pore-scale images and rock fabric observed in different mudrocks. A random walk algorithm is used to generate the kerogen networks with different spatial distributions in synthetic cases. The random walker is controlled to go to different directions with prescribed probability. **Table 2.1** summarizes the input petrophysical and modeling parameters for the eight synthetic cases. These eight synthetic cases, denoted as R1-0 to R1-7, have different directional connectivity and tortuosity of the kerogen network. The synthetic rock R1-0 has no connectivity in the kerogen network so that the only connected conducting phase in all the directions is formation water. R1-1 and R1-7 represent dispersed kerogen distribution (e.g., the Haynesville shale-gas formation) and layered kerogen distribution (e.g., the Woodford shale-gas formation) along the horizontal direction, respectively. These synthetic cases only contain one connected cluster of the kerogen network. Electrical resistivity of gas-bearing kerogen at reservoir temperature is assumed to be 50 ohm-m. Water network distribution is considered to be the same in all seven synthetic cases. **Figure 2.5** shows two of the synthetic pore-scale rock images with two levels (i.e., layered and dispersed) of kerogen spatial connectivity along the Y direction. In **Figure 2.5(a)**, the Y directional connectivity is 0.42 and the corresponding tortuosity is 1.26. In **Figure 2.5(b)**, the Y directional connectivity is 0.18 and the corresponding tortuosity is 2.99. The effective electrical resistivity (R_t) of the synthetic rock samples was estimated using numerical simulation of electric field spatial distribution.

Figure 2.6 shows the impact of directional tortuosity of the kerogen network on electrical resistivity in the horizontal direction, R_h, where formation water salt concentration is 60 kppm NaCl. The electrical resistivity of the synthetic organic-rich mudrocks increases in the horizontal direction as the directional tortuosity of the kerogen network increases in the horizontal direction.

Table 2.1: Summary of the assumed petrophysical, electrical, and modeling parameters for synthetic examples no. 1.

Input parameters	**Value**	**Units**
Total volume of the rock	1x1x1	μm^3
Network grid size	10	nm
Water-filled porosity	5	vol%
Kerogen porosity	35	vol%
Volumetric concentration of kerogen	26	vol%
Formation water salt concentration	60, 116, 196	Kppm NaCl
Electrical conductivity of non-clay minerals at 175 ^{o}F	0	S/m
Electrical conductivity of kerogen at 175 ^{o}F	0.02	S/m
Archie's saturation exponent , *n*	2.3	-
Archie's cementation exponent , *m*	2.3	-
Archie's factor, *a*	1.4	-

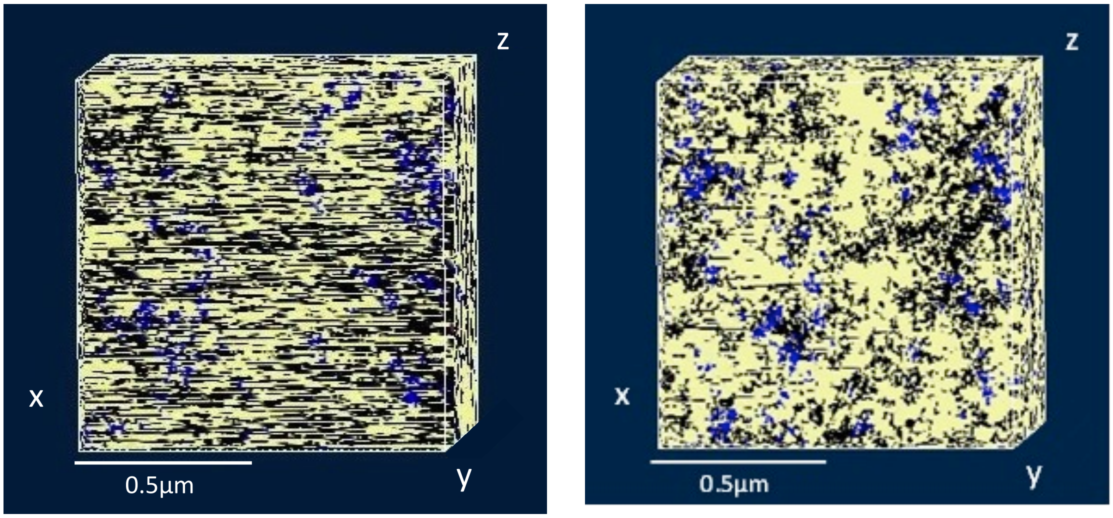

(a) (b)

Figure 2.5: Synthetic three-dimensional pore-scale images of two organic-rich mudrocks with (a) high kerogen connectivity (0.42) in Y direction, where layered kerogen distribution is dominated and (b) low kerogen connectivity (0.18) in Y direction, where dispersed kerogen distribution is dominated. Yellow, blue, and black regions represent the grains, water, and kerogen, respectively

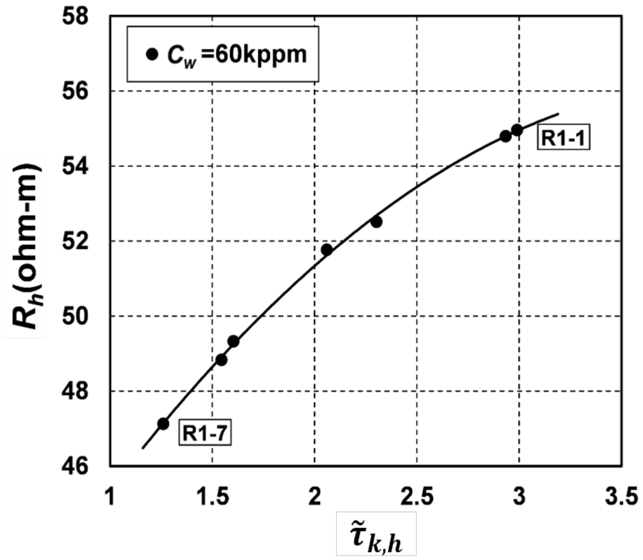

Figure 2.6: Synthetic example no. 1: the impact of directional tortuosity of the kerogen network on electrical resistivity of synthetic organic-rich mudrocks in the horizontal direction. The directional tortuosity decreases from the first (R1-1) to the seventh (R1-7) rock sample.

Equation 2.16 is used to calculate the directional connectivity of the kerogen network from the synthetic rock R1-1 to R1-7 in the horizontal direction. **Table 2.2** summarizes the directional tortuosity of the kerogen network and the corresponding electrical resistivity of the synthetic rocks with different formation water salt concentrations. **Figure 2.7** shows the impact of directional connectivity of the kerogen network on electrical resistivity of synthetic organic-rich mudrocks in the horizontal direction with different formation water salt concentrations: (a) 60 Kppm NaCl, (b) 116 Kppm NaCl, and (c) 196 Kppm NaCl. The sensitivity of electrical resistivity of the rock to the kerogen network's directional connectivity is largely affected by the salt concentration of formation water. This increase in salt concentration decreases the sensitivity of the electrical resistivity to the kerogen network's connectivity. **Figure 2.8** shows the correlation between the effective electrical resistivity and the directional connectivity in the (a) horizontal and (b) vertical directions for one connected kerogen cluster. The results confirm that the increase in the directional connectivity causes a decrease in the electrical resistivity of the rock.

Table 2.2: Summary of the diffusive directional tortuosity of the kerogen network in the horizontal direction, and corresponding electrical resistivity of kerogen-fluid system under different formation water salt concentration.

Synthetic Rock Samples	$\tilde{\tau}_{k,h}$	R_t **@** C_w**=60Kppm NaCl**	R_t**@** C_w**=116Kppm NaCl**	R_t**@** C_w**=196 Kppm NaCl**
R1-1	2.990	54.96	39.84	25.02
R1-2	2.934	54.80	39.75	25.00
R1-3	2.302	52.52	38.54	24.50
R1-4	2.059	51.77	38.13	24.34
R1-5	1.603	49.33	36.79	23.79
R1-6	1.544	48.83	36.52	23.67
R1-7	1.260	47.13	35.56	23.26

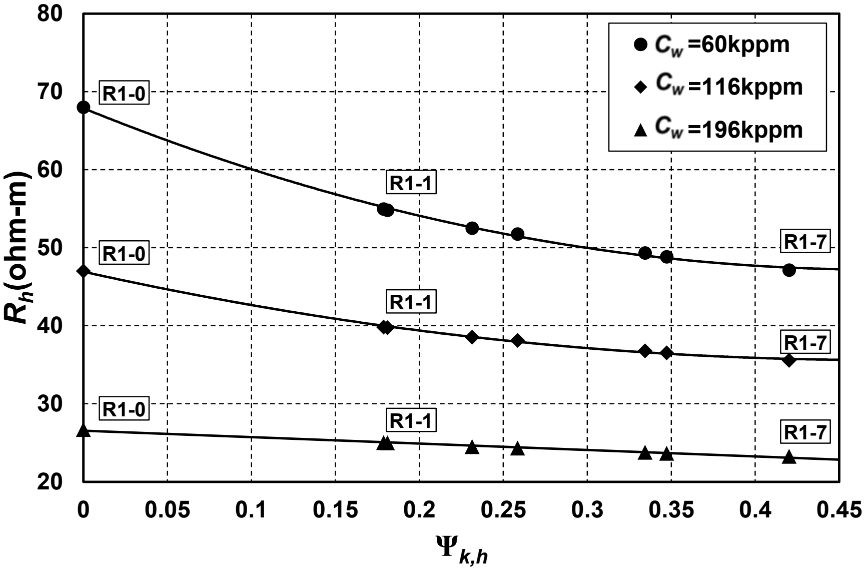

Figure 2.7: Synthetic example no. 1: the impact of directional connectivity of the kerogen network on electrical resistivity of synthetic organic-rich mudrocks in the horizontal direction with different formation water salt concentrations: (a) 60 Kppm NaCl (circle), (b) 116 Kppm NaCl (diamond), and (c) 196 Kppm NaCl (triangle).

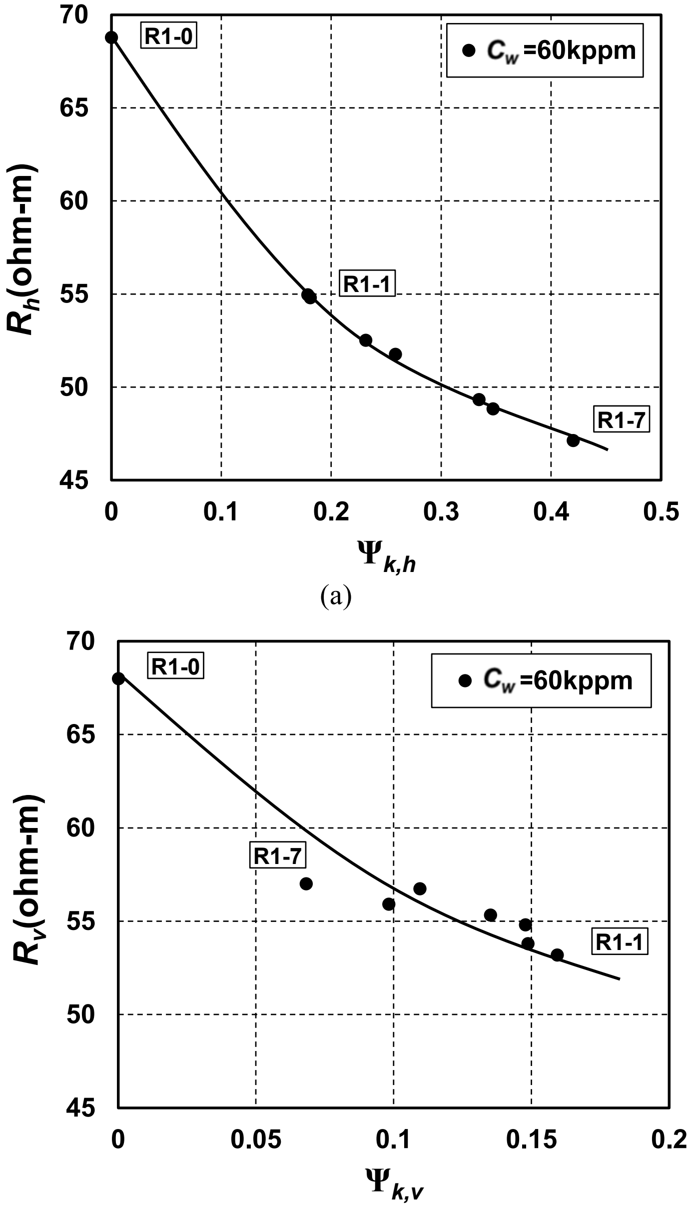

(a)

(b)

Figure 2.8: Synthetic example no. 1: the correlation between the effective electrical resistivity and the directional connectivity in the (a) horizontal and (b) vertical directions for one connected kerogen cluster. R_v represents the electrical resistivity in the vertical direction.

Table 2.3 lists the directional tortuosity of the kerogen network for the synthetic rock R1-1 to R1-7 in the horizontal and vertical directions. The volumetric concentration of kerogen remains 26% in the synthetic rocks. **Table 2.3** shows that the directional tortuosity of the kerogen network in the horizontal direction is increasing from the synthetic rock R1-1 to R1-7. Inversely, the directional tortuosity of the kerogen network in the vertical direction is decreasing from the synthetic rock R1-1 to R1-7.

Table 2.3: Synthetic example no. 1: diffusive directional tortuosity of kerogen network in the horizontal and vertical directions for each rock sample.

Synthetic Rock Sample	$\tilde{\tau}_{k,h}$	$\tilde{\tau}_{k,v}$
R1-1	2.990	3.274
R1-2	2.934	3.509
R1-3	2.302	3.512
R1-4	2.059	3.853
R1-5	1.603	4.789
R1-6	1.544	5.342
R1-7	1.260	7.610

The next step includes quantifying the impact of directional connectivity of kerogen network on the electrical resistivity in the horizontal and vertical directions. **Figures 2.8(a)** and **2.8(b)** show the impact of the directional connectivity of the kerogen network on electrical resistivity of the synthetic rock samples in both the horizontal and vertical directions. $\Psi_{k,h}$ and $\Psi_{k,v}$ represent the directional connectivity of the kerogen network in the horizontal and vertical directions, respectively. A significant variation of effective electrical resistivity occurs in the vertical and horizontal directions due to the spatial distribution of kerogen. The directional connectivity of the kerogen network in the horizontal direction increases from the synthetic rock R1-1 to R1-7, while the directional connectivity in the vertical direction declines from R1-1 to R1-7. For instance, in the horizontal direction, the increase of the directional connectivity of the kerogen network from 0.18 to 0.42 results in the decrease of the horizontal electrical resistivity of the synthetic rocks from 55 to 47 ohm-m, in the presence of 26% volumetric concentration of kerogen. Meanwhile, the decrease in the directional connectivity of the kerogen network in the vertical direction from 0.16 to 0.06 leads to an increase of vertical electrical resistivity of the synthetic rocks from 53 to 57 ohm-m.

This measurable variation of effective electrical resistivity in each direction impacts estimates of water saturation from electrical resistivity. **Figures 2.9(a)** and **2.9(b)** illustrate the impact of directional connectivity of the kerogen network in the horizontal and vertical directions on relative errors in estimates of water saturation, respectively. This error is calculated by comparing the water saturation estimated from Archie's equation against the prescribed model values shown in **Table 2.1**. **Figure 2.9** shows an overestimate of 10.2% to 17.9% in water saturation when the horizontal electrical resistivity is used for water saturation assessment. When applying the vertical electrical resistivity, these errors decrease to 8.5% to 12%. In other words, the errors in estimates of water saturation decrease when the directional connectivity of the kerogen network decreases.

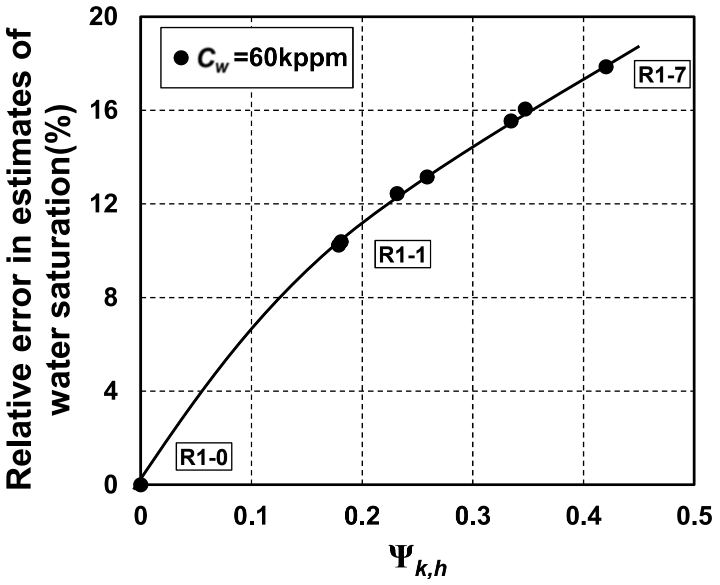

(a)

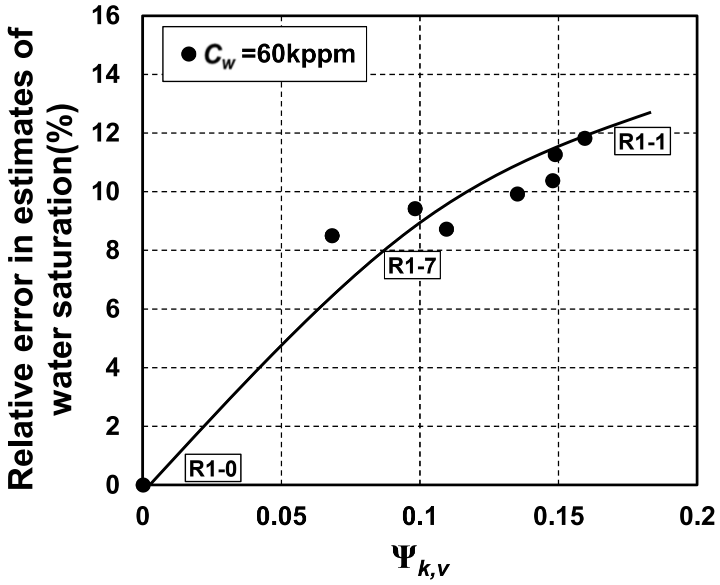

(b)

Figure 2.9: Synthetic example no. 1: the impact of the directional connectivity of the kerogen network in the (a) horizontal and (b) vertical directions on the relative errors in estimates of water saturation (using Archie's equation) compared to the prescribed model value.

Finally, it is shown that the directional connectivity can be calculated when the number of connected conductive clusters is more than one. The seven synthetic rock samples, R2-1 to R2-7, are comprised of more than one connected cluster of the kerogen network. R2-0 is a synthetic rock with no connectivity in the kerogen network. Synthetic case R2-1 includes two clusters of connected kerogen networks. The directional tortuosity values of the two kerogen networks along the Y direction are 1.54 and 1.76, and the directional connectivity values estimated along the Y direction are 0.015 and 0.02, respectively. **Figure 2.10** shows the relationship between the horizontal electrical resistivity and the corresponding directional connectivity for these seven synthetic rocks with 20% volumetric concentration of kerogen. The directional connectivity of the kerogen network in the horizontal direction appears inversely proportional to the horizontal electrical resistivity of the rock samples. The results are consistent with those from previous synthetic rock samples, which only included one connected cluster of the kerogen network.

2.3.2 Synthetic example no. 2: spatial distribution of pyrite

Pyrite can impact electrical properties of the rocks because of its high electrical conductivity. The impact of pyrite on electrical conductivity of rocks has been typically assumed to be negligible because of its low concentration. Average volumetric concentration of pyrite in organic-rich mudrocks is usually less than 4%. However, spatial distribution of pyrite is unpredictable and can vary from isolated to layered. The generated synthetic cases described in this section are designed to investigate the impact of pyrite and its spatial connectivity on electrical resistivity of organic-rich mudrocks.

The primary objective of this section is to quantify the impact of volumetric concentration of pyrite on electrical resistivity of rocks. To achieve this objective, three groups of rock matrices with different directional connectivity of the pyrite network are used while keeping the krogen network isotropic. **Table 2.4** summarizes the petrophysical properties, modeling parameters and rock properties assumed for the synthetic cases shown in this section. Electrical conductivity of N-type pyrite is assumed to be 0.5 S/m (Abraitis et al., 2004) in the input models for the numerical simulations.

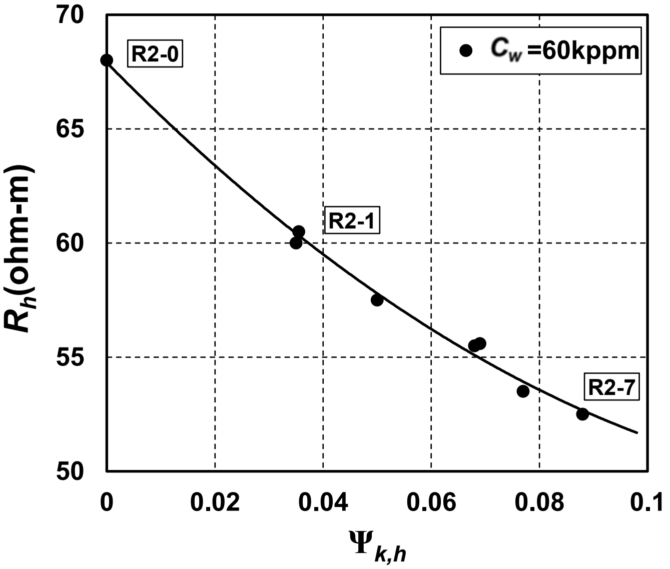

Figure 2.10: Synthetic example no. 1: the relationship between the effective directional resistivity and the directional connectivity for more than one connected kerogen clusters.

Table 2.4: Synthetic example no. 2: the assumed input parameters for the numerical simulation.

Input Parameters	**Value**	**Units**
Total volume of the rock	1x1x1	μm^3
Mesh grid dimension	10	nm
Water-filled porosity	5	vol%
Gas-filled porosity	9	vol%
Volumetric concentration of pyrite	2-16	vol%
Formation Water salt concentration	60	Kppm NaCl
Electrical conductivity of non-clay minerals at 175 ^{o}F	0	S/m
Electrical conductivity of water network at 175 ^{o}F	20	S/m
Electrical conductivity of pyrite network at 175 ^{o}F	0.5	S/m
Archie’s saturation exponent , n	2.3	-
Archie’s cementation exponent , m	2.3	-
Archie’s factor, a	1.4	-

Figure 2.11 shows the impact of volumetric concentration of pyrite with different levels of horizontal connectivity (high, low, and none) on horizontal electrical resistivity of the synthetic rock samples. The results confirm that the impact of volumetric concentration of pyrite on electrical resistivity of the synthetic rock samples becomes more significant as the directional connectivity of the pyrite network increases. For the case of high connectivity in the horizontal direction (layered distribution), the horizontal electrical resistivity changes considerably from 45 ohm-m to around 10 ohm-m (i.e., a 78% decrease in electrical resistivity), when the volumetric concentration of

pyrite increases from 2% to 16%. Meanwhile, for the case of low connectivity in the horizontal direction (dispersed distribution), the horizontal electrical resistivity decreases from 60 ohm-m to around 40 ohm-m (i.e., a 33% decrease in electrical resistivity).

The secondary objective of this section is to quantify the impact of the directional connectivity of the pyrite network on the electrical resistivity of rock samples in the same direction. Six synthetic organic-rich mudrocks with 4% volumetric concentration of pyrite but different directional connectivity of the pyrite network are considered for sensitivity analysis. **Figure 2.12** shows the impact of the directional connectivity of the pyrite network in the horizontal direction on the electrical resistivity of the synthetic rock samples in the horizontal direction. The six synthetic rock matrices are denoted as R3-1 to R3-6. The rock sample R3-0 contains no connectivity in the pyrite network. The results confirm that the increase in the directional connectivity of the pyrite network in the horizontal direction leads to the decrease of horizontal electrical resistivity of the synthetic rocks. The connectivity of the pyrite network in the vertical direction is zero for these six synthetic rocks. Therefore, the contribution of the pyrite to the vertical electrical resistivity is negligible.

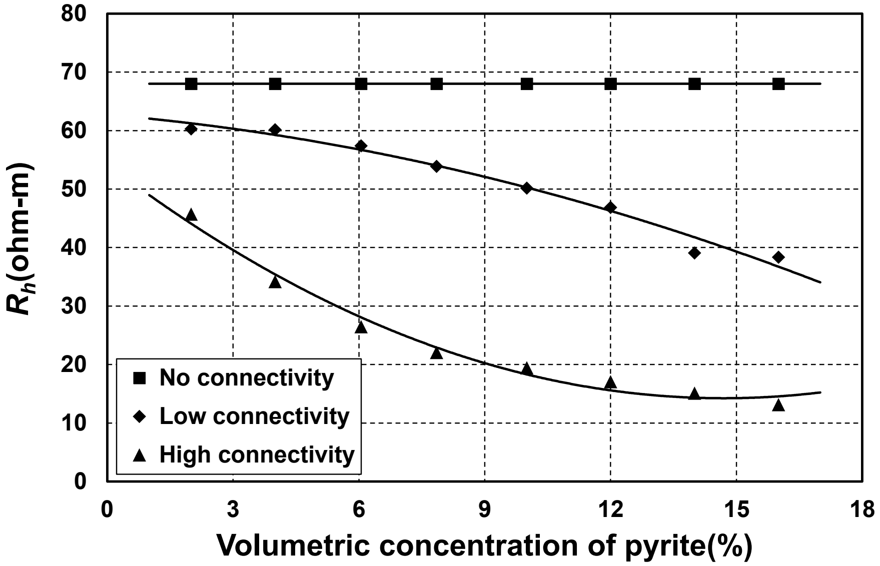

Figure 2.11: Synthetic examples no. 2: the impact of directional connectivity and volumetric concentration of pyrite on the electrical resistivity of organic-rich mudrocks. Rectangular, diamond, and triangle dots represent the electrical resistivity in the horizontal direction with no connectivity, low connectivity, and high connectivity of pyrite network in the horizontal direction, respectively.

Figure 2.13 shows the relative errors in estimates of water saturation using Archie's equation. As the directional connectivity of the pyrite network increases, it results in up to a 23% overestimation of water saturation. Based on the results in **Figure 2.8** and **Figure 2.12**, the estimates of water saturation are more sensitive to the presence of connected pyrite than to the kerogen network. However, this claim cannot be generalized and depends on many other factors, including volumetric concentration of these components, as well as maturity of kerogen.

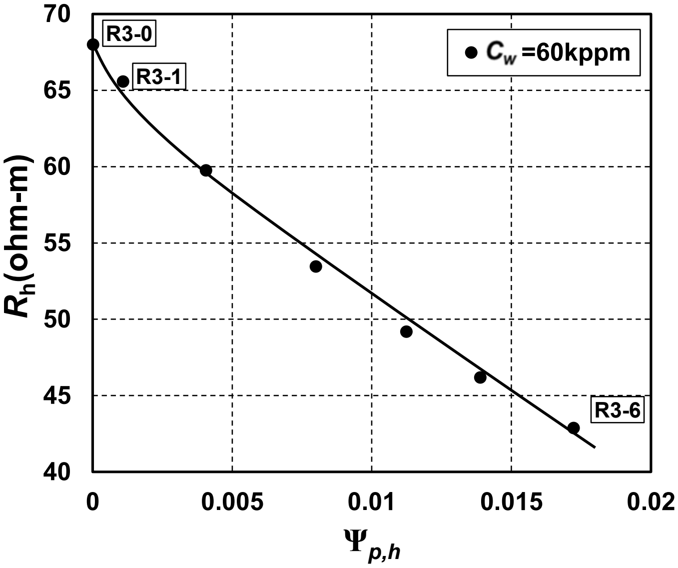

Figure 2.12: Synthetic example no. 2: the impact of the directional connectivity of the pyrite network in the horizontal direction on the horizontal electrical resistivity.

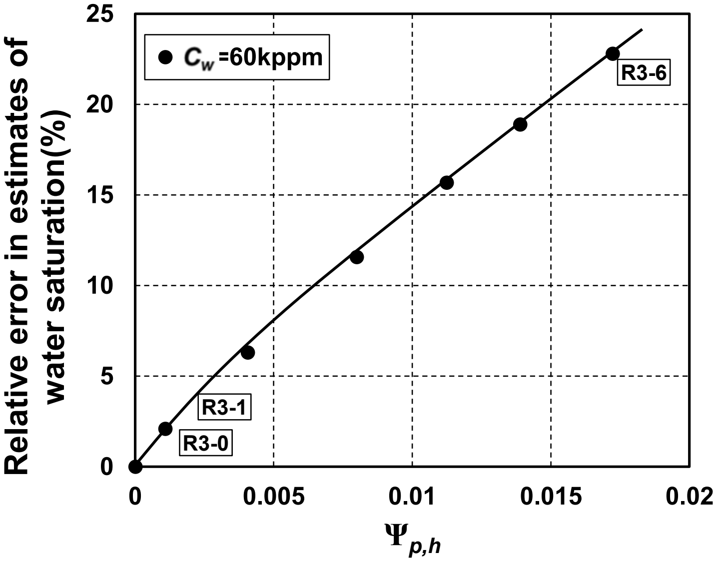

Figure 2.13: Synthetic example no. 2: the relative errors of water saturation estimated upon Archie's equation against the directional connectivity of the pyrite network in the horizontal direction.

2.4 Conclusions

In organic-rich mudrocks, in addition to formation water and clay minerals, kerogen and pyrite can contribute to electrical conductivity of the rock. Consequently, electrical conductivity, directional connectivity, and diffusive directional tortuosity of these conductive rock components should be taken into account when interpreting horizontal or vertical electrical resistivity for assessment of fluid saturations.

This chapter calculated directional connectivity of conductive components in organic-rich mudrocks. This parameter is calculated based on diffusive directional tortuosity, which is estimated using three-dimensional pore-scale rock volumes. It then quantified the impact of directional connectivity and diffusive directional tortuosity of mature kerogen and pyrite networks on the electrical resistivity of organic-rich mudrocks using numerical simulations (i.e., solving Laplace's equation in porous media). Furthermore, the results showed that the formation water salinity affects the sensitivity of rock electrical resistivity to connectivity of the kerogen-fluid network. This chapter has also documented a comparison on the influence of the directional connectivity and diffusive tortuosity of conductive components (e.g., kerogen and pyrite networks) on horizontal and vertical electrical resistivity of synthetic organic-rich mudrocks using pore-scale numerical simulations.

Synthetic cases of organic-rich mudrocks were demonstrated with different levels of connectivity and tortuosity of mature kerogen and pyrite in different directions. Pore-scale numerical simulations showed that directional tortuosity and connectivity of the conductive components could significantly affect electrical resistivity of the rock. The horizontal electrical resistivity drops from 55 to 47 ohm-m, as the directional connectivity of the kerogen network increases from 0.18 to 0.42, respectively, in the horizontal direction. For the same synthetic rock (with the presence of 26% volumetric concentration of kerogen), the vertical electrical resistivity increases from 53 to 57 ohm-m as the directional connectivity of the kerogen network in the vertical direction decreased from 0.16 to 0.06, respectively.

The results confirmed that pyrite can influence electrical resistivity of the rock in certain conditions and needs to be taken into account when interpreting borehole electrical resistivity measurements for water saturation assessment. It has been shown that the increase in the volumetric concentration of the pyrite network decreases the electrical resistivity of the rock. Furthermore, a higher decline in the estimated electrical resistivity of the rock occurs for the case of layered pyrite distribution compared with the dispersed case. The results confirmed that even a small concentration of pyrite (about 4 vol%) could significantly affect electrical resistivity of the rock in a particular direction, if well connected in that direction.

Failure to consider the contribution of directional connectivity and diffusive directional tortuosity of kerogen and pyrite leads to significant errors when estimating water saturation using electrical resistivity measurements in organic-rich mudrocks. The results showed that Archie’s equation overestimates water saturation by 17.9% and 23% in the presence of horizontally layered connected kerogen (26 vol%) and pyrite (4 vol%), respectively, if horizontal electrical resistivity is used for the estimation of water saturation. Directional borehole resistivity measurement tools can be used to provide vertical and horizontal resistivity. Taking into account the quantified directional connectivity of rock components at different scales can potentially improve interpretation of these measurements for reliable assessment of water/hydrocarbon saturation. Although this chapter focuses on pore-scale evaluation of electrical properties of the rock, the work can be further extended to log-scale applications in the future.

The results shown in this chapter are influenced by the assumed conductivity for pure kerogen and gas-bearing kerogen at reservoir temperature. Further laboratory measurements are required for reliable assessment of conductivity values for pure kerogen at different temperatures and different levels of maturity. In general, the results are promising for the possible application of electrical resistivity logs in assessment of kerogen network connectivity in organic-rich mudrocks in certain conditions where kerogen is highly mature.

CHAPTER III

PORE-SCALE EVALUATION OF DIELECTRIC MEASUREMENTS IN FORMATIONS WITH COMPLEX PORE AND GRAIN STRUCTURES

Dielectric permittivity measurements are typically used to estimate water-filled porosity. The dielectric interpretation methods such as Complex Refractive Index Model (CRIM) (i.e., volumetric techniques) are extensively used to correlate dielectric permittivity of fluid-bearing rocks to petrophysical properties such as water-filled porosity. However, volumetric techniques usually oversimplify the rock structure and do not take into account the impact of spatial distribution of solid and fluid components on dielectric properties of the rock. The lack of reliable rock physics models to interpret dielectric permittivity measurements can lead to significant uncertainty in estimates of water-filled porosity.

This chapter applies a pore-scale numerical simulation method to quantify the impact of pore and grain structures and anisotropy on dielectric permittivity measurements, and introduces a new dielectric permittivity model to improve assessment of water-filled porosity in formations with complex pore and grain structures. A diffusive directional tortuosity factor is used to quantify the geometry of pore and grain networks.

The introduced techniques are applied on 3D CT-scan images of sandstone and carbonate samples as well as synthetic organic-rich mudrocks. It is shown that the new dielectric permittivity model is more reliable for assessing water-filled porosity compared to the conventional CRIM, in the twelve sandstone and carbonate samples evaluated in this chapter. In the case of synthetic organic-rich mudrocks, it is observed that (a) despite the change of the overall dielectric permittivity, accuracy in estimates of water-filled porosity is not affected in the presence of kerogen, if the influence of kerogen is correctly taken into account by the CRIM, and (b) the presence of pyrite and its spatial distribution significantly affect the dielectric permittivity of organic-rich mudrocks. Failure to consider influence of pyrite and its spatial distribution on dielectric permittivity may cause large uncertainty in estimating water-filled porosity.

3.1 Introduction

Borehole electrical resistivity measurements have been traditionally applied for assessment of water and hydrocarbon saturation. However, interpretation of electrical resistivity is challenging and involves significant uncertainty in organic-rich and carbonate formations, resulting from complex pore structure and the presence of conductive pyrite and mature kerogen (Passey et al., 2010; Kethireddy et al., 2014). Because of challenges and uncertainties associated with interpretation of electrical resistivity measurements, dielectric permittivity measurements have become attractive candidates for assessment of water and hydrocarbon saturation in organic-rich mudrocks and carbonate formations. Several studies have been previously conducted on the interpretation of the dielectric property of the porous medium (Calvert and Wells, 1977; Wharton et al., 1980; Dahlberg and Ference, 1984). Among previously published techniques, Complex Refractive Index Model (CRIM) has been the most widely used approach (Birchak et al., 1974; Dobson et al., 1985; Heimovaara et al., 1994). However, applicability of the CRIM is limited, as it oversimplifies the pore structure and neglects geometrical distribution of rock components. Stroud et al. (1986) proposed an analytical model to take into account the impact of grain geometry when interpreting dielectric permittivity. They develop an analytical model for a family of brine-saturated rocks in which the contacting area of neighboring grains is negligible compared to the grain surface area. Feng and Sen (1985) also provided a geometry-dependent dielectric permittivity model for partially saturated rocks by assuming ideal grain shapes such as spherical and platy grains. Toumelin et al. (2009) pointed out that rock morphology and pore connectivity affect dielectric permittivity measurements. Myers et al. (1996) introduced a pore-geometry-dependent dispersion model to improve the volumetric method, which assimilates the impact of vugs and interconnected pore space on dielectric permittivity of rocks. However, they do not take into account the spatial distribution, tortuosity, and connectivity of pore and grain networks in their model.

This chapter conducts pore-scale numerical simulations to (a) estimate the effective dielectric permittivity of rock-fluid mixture by taking into account pore and grain structures and spatial distributions of rock and fluid constituents, (b) improve interpretation of dielectric measurements for assessing water-filled porosity, and (c) quantify uncertainty in estimates of water-filled porosity by interpreting dielectric measurements using the CRIM. Assessment of water-filled porosity in complex formations is improved by taking into account pore/grain structures in the CRIM.

The introduced new dielectric permittivity model is first applied on 3D pore-scale images of sandstone and carbonate core samples as well as synthetic examples of organic-rich mudrocks, all with complex pore structure. Next, the diffusive directional tortuosity of rock samples is calculated based on pore-scale images to reflect the rock's anisotropic and heterogeneous characteristic. The diffusive directional tortuosity is then incorporated into the CRIM to improve estimates of the effective dielectric permittivity and water-filled porosity. Furthermore, the impact of kerogen and pyrite networks is studied on dielectric permittivity measurements in the case of organic-rich mudrocks.

The upcoming sections describe the methods for pore-scale numerical simulations and directional tortuosity assessment, the new dielectric permittivity model, and the results from examples of sandstone, carbonate, and organic-rich mudrocks.

3.2 Method

Micro computed tomography (micro-CT) is a quick and non-destructive method used to generate 3D digital pore-scale images of internal structure of rock samples, which has many advantages over conventional core analysis methods. In this chapter, the 3D digital rock images of sandstones and carbonates, which are taken from Imperial College London (Dong, 2007), are generated by micro-CT. Each digital image is converted into a 3D grid structure where the grid size is 3.875 μm in the case of sandstone rocks and 2.857 μm in the case of carbonate rocks. The organic-rich mudrocks are synthetized based on petrophysical parameters in actual rock samples and actual 2D pore-scale FIB-SEM rock images (the construction procedures are described in detail in Chapter II, Subsection 2.2.1) and the grid size is 10 nm. The assumed petrophysical models are the same as those introduced in Chapter II, Subsection 2.2.2. Diffusive directional tortuosity (Chapter II, Subsection 2.2.3) is applied to quantify complexity of the spatial structure of conductive matrix components.

The following subsections first introduce the high-frequency dielectric permittivity measurement and numerical simulation procedures for calculating the effective relative dielectric permittivity of 3D pore-scale images. Next, a new dielectric permittivity model that takes into account diffusive directional tortuosity to improve assessment of water-filled porosity is proposed. Finally, a workflow is summarized for the study on pore-scale evaluation of dielectric permittivity measurements in formations with complex pore and grain structures.

3.2.1 High-frequency dielectric measurements

The measurement frequencies affect the application of dielectric permittivity measurements. Hizem et al. (2008) proposed a multi-frequency dielectric permittivity measurement from 20MHz to 1GHz to estimate formation water saturation, invaded zone water salinity, and rock texture. In the low-frequency range ($\omega < 1$GHz) dielectric permittivity of formations is affected by interfacial polarization, which is generated from cation exchange capacity (CEC), ions (Maxwell Wagner effect), and rock texture. Thus, in the low-frequency range, dielectric permittivity measurements can reveal textural information such as Archie's cementation exponent, and assess clay volume and water salinity of the formation. In the high-frequency range (ω > 1GHz), interfacial polarization is largely attenuated and water molecule polarization becomes the dominant parameter affecting dielectric permittivity. Therefore, dielectric measurements at high-frequency are widely used to estimate water-filled porosity (Bittar et al., 2010). In this chapter, we focus on the single high-frequency (i.e., 1GHz) dielectric numerical simulations for assessing water-filled porosity.

3.2.2 Assessment of relative dielectric permittivity using pore-scale numerical simulations

The relative dielectric permittivity is the ability of a body to store electric charges. It is a complex value given by

$$\varepsilon(\omega)= \varepsilon'(\omega)+i\frac{\sigma(\omega)}{2\pi\varepsilon_0\omega}, \tag{3.1}$$

where ω is frequency, ε is relative dielectric permittivity vector where $\varepsilon(\omega, i, j, k)$ is the relative dielectric permittivity value for the (i, j, k) grid point at frequency ω, ε' is the real part of ε, ε_0 is the dielectric permittivity of the vacuum space, which is equal to $8.854\text{x}10^{-12}$ F/m, and $\sigma(\omega)$ is the conductivity vector at frequency ω. The real and imaginary components correspond to the dielectric constant and dielectric loss, respectively.

To estimate spatial distribution of electric potential field in a non-steady state condition, we solve the continuity equation in the time domain given by

$$\nabla \cdot \vec{J} + \frac{\partial \rho}{\partial t} = 0, \tag{3.2}$$

where ρ is electric current density which can be written as

$$\rho = \varepsilon \nabla \cdot \vec{E}, \tag{3.3}$$

where ε is local relative dielectric permittivity. By substituting **Equations 2.19** and **3.3** into **Equation 3.2**, the continuity equation in time domain can be written as

$$\nabla \cdot \left(\sigma \nabla U\right) + \frac{\partial}{\partial t}\left(\nabla \cdot \left(\varepsilon \nabla U\right)\right) = 0. \tag{3.4}$$

where σ is electrical conductivity and ε is relative dielectric permittivity such that $\sigma(i, j, k)$ and $\varepsilon(i, j, k)$ are the electrical conductivity and relative dielectric permittivity for the (i, j, k) point in the digitized pore-scale images.

Through the Fourier transform, **Equation 3.4** can be rewritten as

$$\nabla \cdot (\varepsilon(\omega) \nabla \hat{U}(\omega)) = 0, \tag{3.5}$$

where $\hat{U}$ is electric potential distribution at frequency domain. In the simulation that is presented in this dissertation, ω is assumed to be 1 GHz. However, dielectric permittivity can be estimated at other frequencies. Spatial distribution of electrical potential field is calculated by solving **Equation 3.5** using the finite difference method. Boundary conditions for calculating the effective relative dielectric permittivity along the Y direction include Dirichlet and Neumann boundary conditions, given by

$$\hat{U}\Big|_{Y=1} = 0 \text{ and } \hat{U}\Big|_{Y=N} = U_0, \tag{3.6}$$

and

$$\frac{\partial \hat{U}}{\partial Y}\bigg|_{X=1,N} = 0 \text{ and } \frac{\partial \hat{U}}{\partial Y}\bigg|_{Z=1,N} = 0, \tag{3.7}$$

respectively. The effective dielectric permittivity along the Y direction is then calculated via

$$\varepsilon_{eff}^{Y} = \frac{l_Y}{l_Z l_X U_0^2} \int \varepsilon(r) \left| \nabla \hat{U}(r) \right|^2 dV, \tag{3.8}$$

where l_X, l_Y, and l_Z are the length of rock sample in the X, Y, and Z directions (which are all equal to N-1 in the simulation), respectively, and U_0 is the initial potential difference along the Y direction. **Equation 3.8** can be used to estimate the effective dielectric permittivity along the X and Z directions, if Y is replaced by X and Z, respectively. The discretized form of **Equation 3.8** is given by

$$\varepsilon_{eff}^{Y} = \frac{1}{N-1} \sum_{i,j,k} \left\{ \begin{array}{l} \left(\hat{U}(\omega=1,i+1,j,k) - \hat{U}(\omega=1,i,j,k)\right)^2 \cdot \dfrac{\varepsilon(\omega=1,i+1,j,k) + \varepsilon(\omega=1,i,j,k)}{2} \\ + \left(\hat{U}(\omega=1,i,j+1,k) - \hat{U}(\omega=1,i,j,k)\right)^2 \cdot \dfrac{\varepsilon(\omega=1,i,j+1,k) + \varepsilon(\omega=1,i,j,k)}{2} \\ + \left(\hat{U}(\omega=1,i,j,k+1) - \hat{U}(\omega=1,i,j,k)\right)^2 \cdot \dfrac{\varepsilon(\omega=1,i,j,k+1) + \varepsilon(\omega=1,i,j,k)}{2} \end{array} \right\}. \tag{3.9}$$

3.2.3 The new dielectric permittivity model

The CRIM is a common approach applied to interpret dielectric measurements for assessment of water saturation, expressed as

$$\sqrt{\varepsilon} = \sum_{i=1}^{n} C_i \sqrt{\varepsilon_i}\,, \tag{3.10}$$

where n is the number of components in a rock-fluid mixture, ε is the effective relative dielectric permittivity, and ε_i and C_i are the relative dielectric permittivity and volumetric concentration of ith rock component, respectively. In the case of reservoir rocks, the CRIM is usually expressed as

$$\sqrt{\varepsilon} = S_w \phi_t \sqrt{\varepsilon_w} + (1 - S_w)\phi_t \sqrt{\varepsilon_{HC}} + (1 - \phi_t)\sqrt{\varepsilon_{matrix}}\,, \tag{3.11}$$

where S_w is water saturation, ϕ_t is total porosity, and ε_w, ε_{HC}, and ε_{matrix} are the relative dielectric permittivity of water, hydrocarbon, and rock matrix, respectively. Water saturation can be estimated via

$$S_w = \frac{\sqrt{\varepsilon} - (1 - \phi_t)\sqrt{\varepsilon_{matrix}} - \phi_t \sqrt{\varepsilon_{HC}}}{\phi_t(\sqrt{\varepsilon_w} - \sqrt{\varepsilon_{HC}})}\,. \tag{3.12}$$

While, this model does not take into account structure and spatial distribution of rock components. Therefore, we modify it to a new dielectric model that includes the structure of pore and matrix constituents via

$$\sqrt{\varepsilon_x} = f_{w,x} S_w \phi_t \sqrt{\varepsilon_w} + f_{HC,x}(1 - S_w)\phi_t \sqrt{\varepsilon_{HC}} + f_{matrix,x}(1 - \phi_t)\sqrt{\varepsilon_{matrix}}\,, \tag{3.13}$$

where ε_x, $f_{w,x}$, $f_{HC,x}$, and $f_{matrix,x}$ are the relative dielectric permittivity, tortuosity-dependent coefficients for water, hydrocarbon, and rock matrix components along the X direction, respectively. In this chapter, it is assumed that these tortuosity-dependent coefficients are power functions of diffusive directional tortuosity. For example, $f_{w,x}$ can be defined by

$$f_{w,x} = a_{w,x} \tilde{\tau}_{w,x}^{q_{w,x}} + d_{w,x}, \tag{3.14}$$

where $\tilde{\tau}_{w,x}$ is the diffusive directional tortuosity of water network in the X direction, and $a_{w,x}$, $q_{\mathrm{w,x}}$ and $d_{w,x}$ are the coefficients dependent on pore structure, grain shapes, and cementation, respectively. The same definition can also be applied to the Y and Z directions.

3.2.4 Workflow

Figure 3.1 summarizes the workflow for the pore-scale evaluation of dielectric permittivity measurements in formations with complex pore and grain structures. 3D digitalized images including sandstone, carbonate, and synthetic organic-rich mudrocks are used for pore-scale numerical simulation. For rock samples without pyrite and kerogen, the simulation is directly implemented to get the effective dielectric permittivity of rocks and tortuosity-dependent coefficient of pore/water network. For rock samples with pyrite and kerogen, the simulation is implemented, first to get the tortuosity-dependent coefficient of the pore/water network by treating pyrite and kerogen as normal grain, and second, to estimate tortuosity-dependent coefficient of pyrite and kerogen networks by restoring kerogen and pyrite back to the rock matrix. The tortuosity-dependent coefficient for the pore and grain networks is applied to the same rock types in estimates of the water-filled porosity by using the new developed dielectric permittivity model. Finally, the estimated water-filled porosity is compared using the newly developed dielectric permittivity model and the Complex Refractive Index Model.

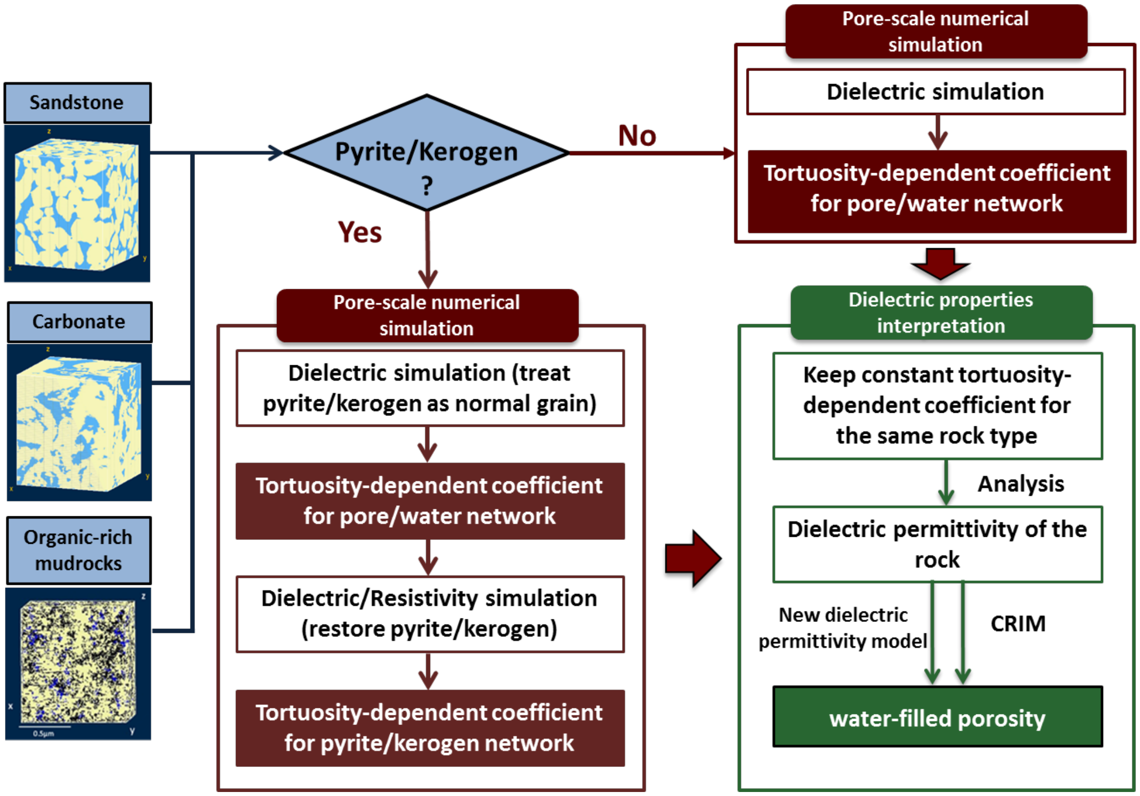

Figure 3.1: The workflow for the study on pore scale evaluation of the dielectric measurement in the formation with complex pore and grain structure.

3.3 Results

This section includes the results from our pore-scale numerical simulations. It first shows the correlation between the relative dielectric permittivity and the diffusive directional tortuosity of the pore space (fully saturated by water) for six sandstone samples (from the same rock type) and six carbonate samples (from the same rock type). Then, it compares the relative errors in assessment of water-filled porosity using the

CRIM and the new dielectric permittivity model. For synthetic examples of organic-rich mudrocks, it shows the relative error in estimates of water-filled porosity from the CRIM in the presence of different amounts of total organic content (TOC). This section also show the impact of the diffusive directional tortuosity of the pyrite network on the effective relative dielectric permittivity along the same direction and the corresponding estimates of water-filled porosity.

3.3.1 The effect of tortuosity on relative dielectric permittivity of sandstone and carbonate rock samples

3D CT-scan images of six sandstone samples and six carbonate samples from different formations are used in the research. These images are taken from the Petroleum Engineering & Rock Mechanics Group at Imperial College London (Dong, 2007). The image resolution for the sandstone and carbonate samples is 3.85μm and 2.857μm, respectively (Dong, 2007). The voxel size used for numerical simulations in all the rock samples is 100x100x100. **Figure 3.2** shows examples of the 3D pore-scale images in two of the rock samples. The interconnected and isolated pore spaces are both calculated using 3D pore-scale images of the rocks. **Table 3.1** lists the diffusive directional tortuosity of the water network and the calculated total and interconnected pore space for six-sandstone samples and six carbonate samples. It’s observed that the tested carbonate samples have more isolated small pore clusters compared to the sandstone samples.

Table 3.1: Total (ϕ_t) and interconnected (ϕ_c) porosity estimated for the six sandstone and carbonate rock samples calculated based on 3D pore-scale images

Samples	Dir.	$\tilde{\tau}_w$	ϕ_t (%)	ϕ_c (%)	Samples	Dir.	$\tilde{\tau}_w$	ϕ_t (%)	ϕ_c (%)
Sandstone 1	X	2.90	22.4	21.8	Carbonate 1	X	2.90	21.7	18.6
	Y	2.47				Y	15.6		
	Z	4.34				Z	2.36		
Sandstone 2	X	2.27	27.0	26.0	Carbonate 2	X	3.57	27.4	22.7
	Y	1.91				Y	3.02		
	Z	3.00				Z	2.32		
Sandstone 3	X	7.85	23.0	22.4	Carbonate 3	X	40.46	13.2	10.1
	Y	10.2				Y	84.2		
	Z	11.4				Z	59.64		
Sandstone 4	X	8.90	24.0	23.2	Carbonate 4	X	23.98	15.0	13.1
	Y	12.2				Y	11.03		
	Z	12.4				Z	7.34		
Sandstone 5	X	2.78	35.6	33.1	Carbonate 5	X	8.42	15.1	11.6
	Y	2.78				Y	5.85		
	Z	1.96				Z	21.79		
Sandstone 6	X	2.05	21.1	20.3	Carbonate 6	X	4.12	20.7	17.8
	Y	3.05				Y	8.64		
	Z	3.12				Z	3.81		

In the numerical simulations, it is assumed that all the pore space is fully saturated with water. The Klein-Swift model (Klein and Swift, 1977) is applied to estimate the relative dielectric permittivity of saline water by assuming that the formation water has salt concentration of 3000 ppm and temperature of 86°F. The resulting relative dielectric permittivity value for water is 76+10*j*. It is also assumed that relative dielectric permittivity of carbonate and sandstone grains are 7.5+0.01*j* and 4.65+0.1*j*, respectively, which are within the reasonable range provided by Schmitt et al. (2011) and Quirein et al. (2012).

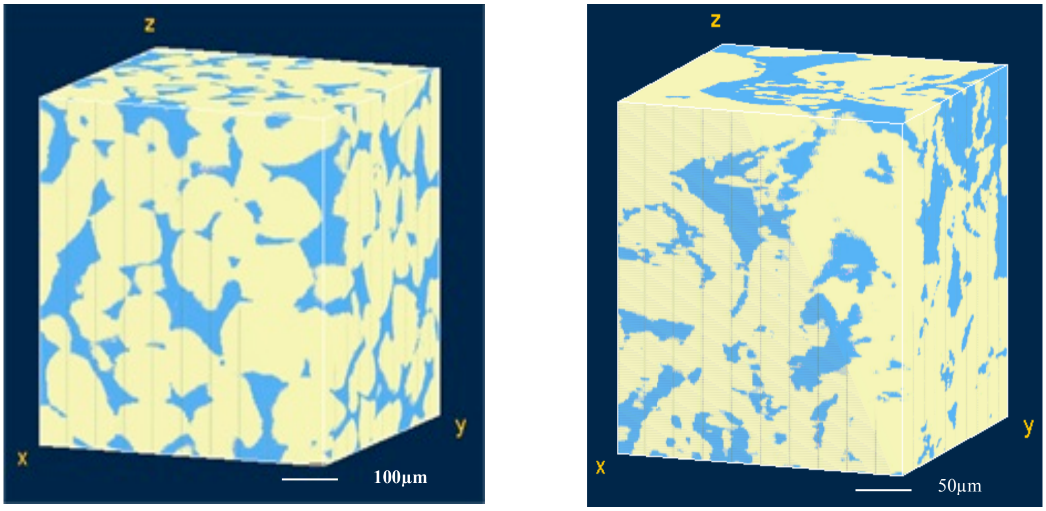

(a) (b)

Figure 3.2: 3D CT-scan images of (a) sandstone and (b) carbonate rock samples. Yellow and blue areas represent grains and pore space, respectively.

Next, the effective relative dielectric permittivity of the rock samples are calculated in the X, Y, and Z directions using numerical simulations. The diffusive directional tortuosity is also calculated for each sandstone and carbonate sample. **Figure 3.3** shows the impact of the diffusive directional tortuosity of the water network on the relative dielectric permittivity in two rock samples. It is observed that the diffusive directional tortuosity changes in each direction for these rock samples, which significantly impacts the directional relative dielectric permittivity. The results shown in

Figure 3.3 verify that the relative dielectric permittivity decreases as the result of increase in the diffusive directional tortuosity. The other sandstone and carbonate samples also show the same relationship between the diffusive directional tortuosity and the relative dielectric permittivity. Generally, the diffusive directional tortuosity value for the tested carbonate samples is larger than the sandstone samples, which indicates more complex pore structures in these carbonate samples.

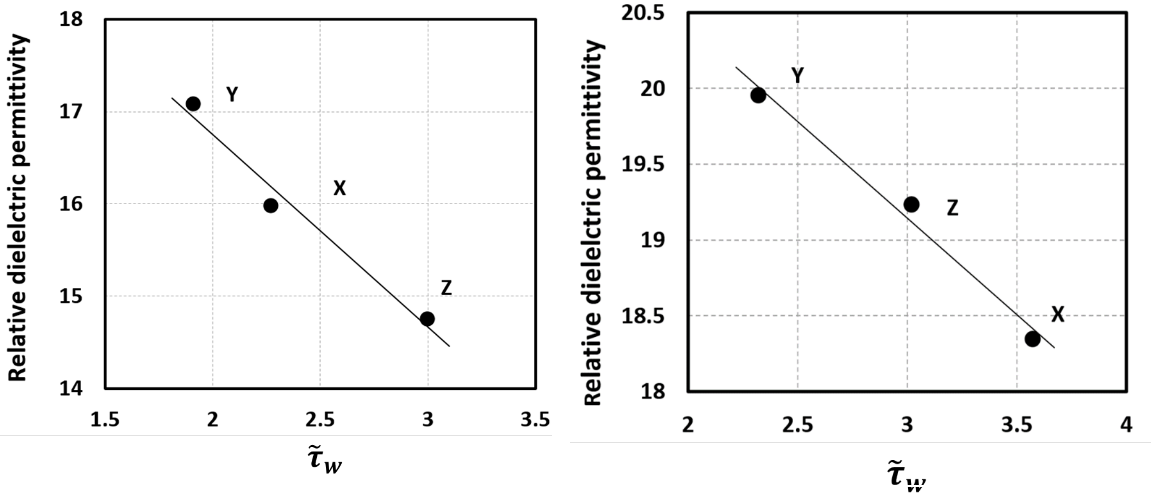

(a) (b)

Figure 3.3: Correlation between the diffusive directional tortuosity of the water network and the relative dielectric permittivity for (a) sandstone sample 2 and (b) carbonate sample 2. X, Y, and Z represent the direction along which the tortuosity and the relative dielectric permittivity are calculated.

3.3.2 The application of the new modified dielectric permittivity model to the sandstone and carbonate rock samples

For the case of sandstone and carbonate samples, it is assumed that f_{matrix} is equal to one, since the tortuosity of the rock matrix is close to tortuosity of the free space, especially in low-porosity rocks. However, this assumption is not valid in the presence of matrix components with high permittivity values, such as pyrite. Also, it is assumed that f_{HC} is equal to one, because of its low permittivity value. Thus, we can simplify **Equation 3.13** to

$$\sqrt{\varepsilon} = (a_w \tilde{\tau}_w^{\,q_w} + d_w) S_w \phi_t \sqrt{\varepsilon_w} + (1 - S_w)\phi_t \sqrt{\varepsilon_{HC}} + (1 - \phi_t)\sqrt{\varepsilon_{matrix}} \,. \tag{3.15}$$

Three sandstone samples (sandstone samples 1-3) and three carbonate samples (carbonate samples 1-3) are used as calibration samples to calculate the correlation between the tortuosity and the tortuosity-dependent coefficient. This coefficient will then be used in the new dielectric permittivity model (**Equation 3.15**) to estimate water-filled porosity in all the rock samples. **Figure 3.4** shows the relationship between the tortuosity-dependent coefficient and the diffusive directional tortuosity of the water network for sandstone 1-3 and carbonate 1-3 samples. Based on the calibration results shown in **Figure 3.4**, the correlation between the tortuosity-dependent coefficient and diffusive directional tortuosity of the water network for sandstone 1-3 and carbonate 1-3 samples can be written as

$$f_w = 0.7\tilde{\tau}_w^{\,-0.95} + 0.7 \tag{3.16}$$

and

$$f_w = 0.58\tilde{\tau}_w^{-0.42} + 0.65. \tag{3.17}$$

Next, **Equations 3.16** and **3.17** are applied to estimate f_w for sandstone 4-6 and carbonate 4-6 samples, respectively. Furthermore, the estimated f_w is used in the introduced new model to estimate the water-filled porosity in the corresponding sandstone 4-6 and carbonate 4-6 samples.

Figure 3.5 shows the correlation between the tortuosity-dependent coefficient and the relative errors in estimates of water-filled porosity from the CRIM and the new model. The decrease in f_w increases the relative error in estimates of water-filled porosity from the CRIM. In other words, increase in calculated complexity of pore structure leads to increase in the possible errors in dielectric-based assessment of water-filled porosity using volumetric methods such as the CRIM. It is also observed that the relative error in estimates of water-filled porosity using the CRIM is up to 27% and 26% for sandstone and carbonate samples, respectively. By using the new model, the relative errors are all within 10%. The decrease in uncertainty of dielectric permittivity assessment improves the estimates of water-filled porosity from dielectric measurements.

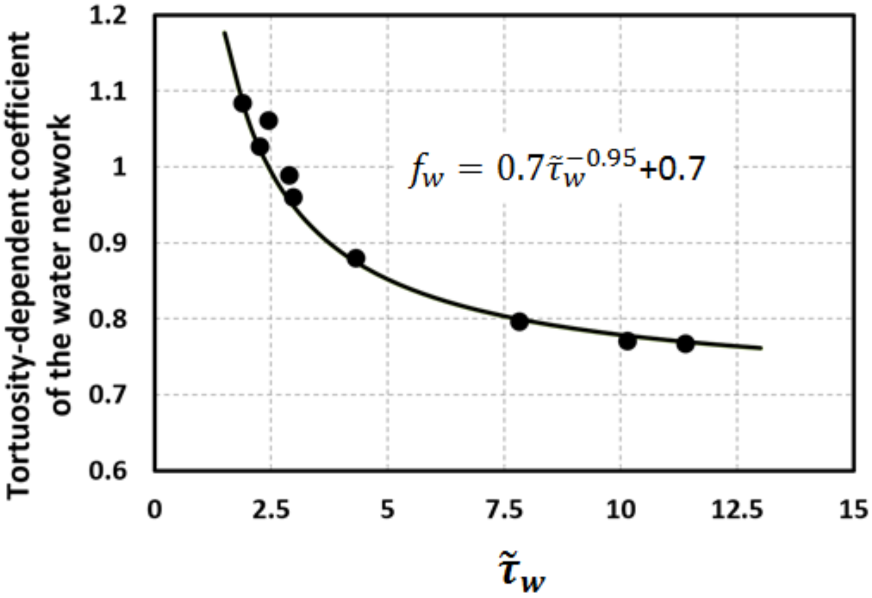

(a)

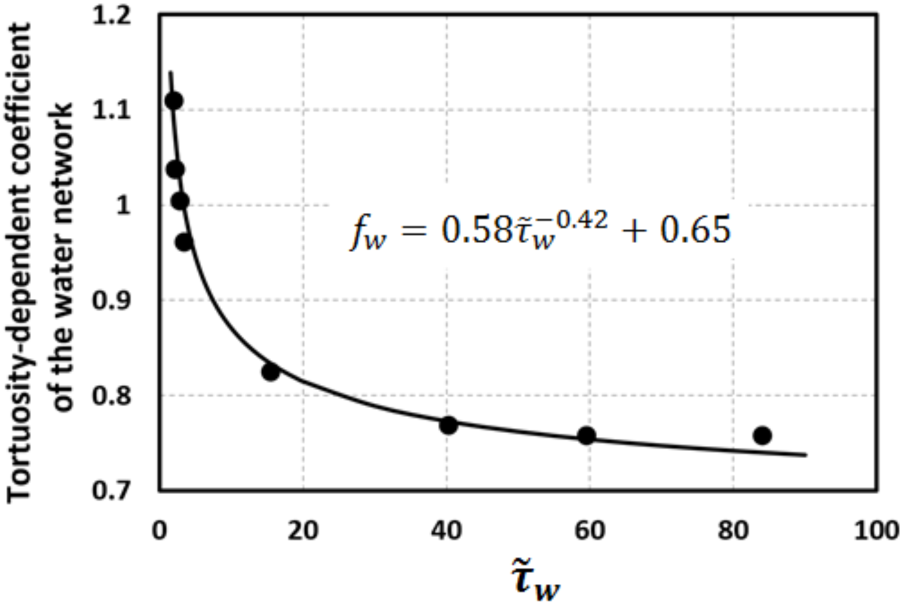

(b)

Figure 3.4: Correlation between the tortuosity-dependent coefficient, f_w, and the diffusive directional tortuosity of the water network for (a) sandstone samples 1, 2, and 3 and (b) carbonate samples 1, 2, and 3.

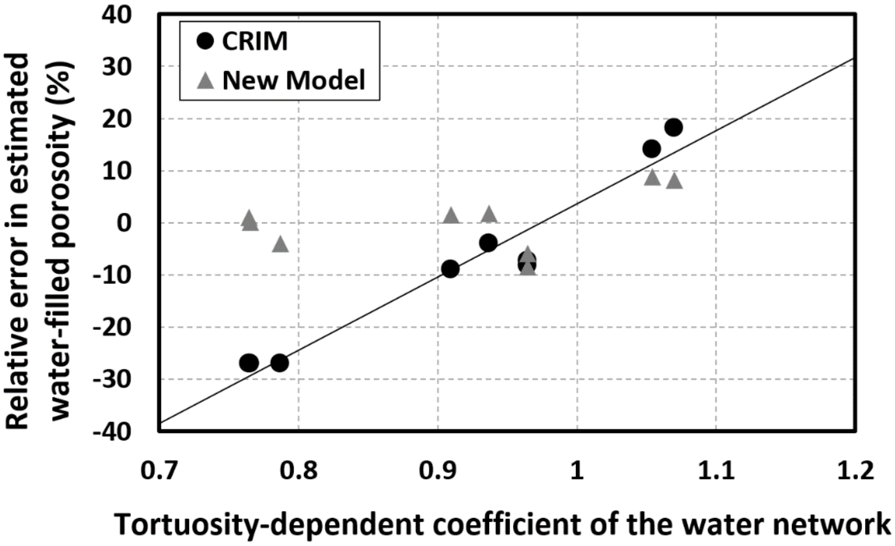

(a)

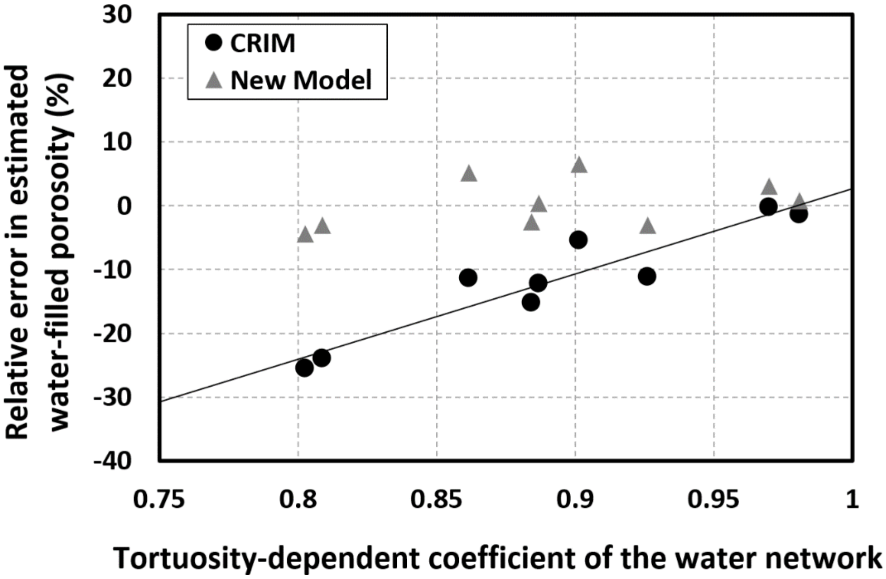

(b)

Figure 3.5: The impact of the tortuosity-dependent coefficient for the water network on relative errors in estimates of water-filled porosity using the CRIM and the new model for (a) sandstone samples 4, 5, and 6 and (b) carbonate samples 4, 5, and 6.

3.3.3 Dielectric permittivity of organic-rich mudrocks

3.3.3.1 Synthetic case no. 1: the impact of TOC on relative dielectric permittivity

A set of synthetic organic-rich mudrock examples containing variable TOC is designed to investigate the impact of TOC on the accuracy of the CRIM. **Table 3.2** summarizes the assumed petrophysical properties for synthetic case no. 1. In this set of synthetic rocks, water-filled porosity and the structure of pore space remain the same, while TOC varies between 1wt% and 10.5wt% in the seven synthetic examples. The diffusive directional tortuosity of the kerogen network remains almost constant in the seven synthetic examples. The kerogen pore space is assumed to be fully saturated by gas. **Figure 3.6(a)** compares the impact of TOC on the relative dielectric permittivity, estimated from the CRIM and from the numerical simulations. **Figure 3.6(b)** illustrates the relative errors in estimates of water-filled porosity obtained from the CRIM.

Table 3.2: Organic-rich Mudrock, synthetic case no.1: the assumed parameters in the petrophysical model.

Parameters	**Value**	**Units**
ϕ_w	3	vol%
ϕ_k	30	vol%
ϕ_t	3.9-9.3	vol%
TOC	1-10.5	wt%
Salt concentration of formation water	35000	ppm
Formation temperature	86	^{o}F
ε_w @1GHz	70+10j	-
ε_k @1GHz	2.5	-
ε_g @1GHz	7.5+0.01j	-

The increase in TOC causes the decrease in relative dielectric permittivity of the organic-rich mudrock samples from 8.22 to 6.3, which is within the reasonable range reported in previous publications (Clennell et al., 2010; Seleznev et al., 2011). There is not a significant difference between the results of water-filled porosity obtained from the CRIM and the prescribed model values. The reason for this observation is the relatively close dielectric permittivity of kerogen (2.5) and grains (7.5+0.01*j*), when comparing against dielectric permittivity of saline water of (76+10*j*). Thus, the performance of CRIM is not significantly affected by the presence of kerogen.

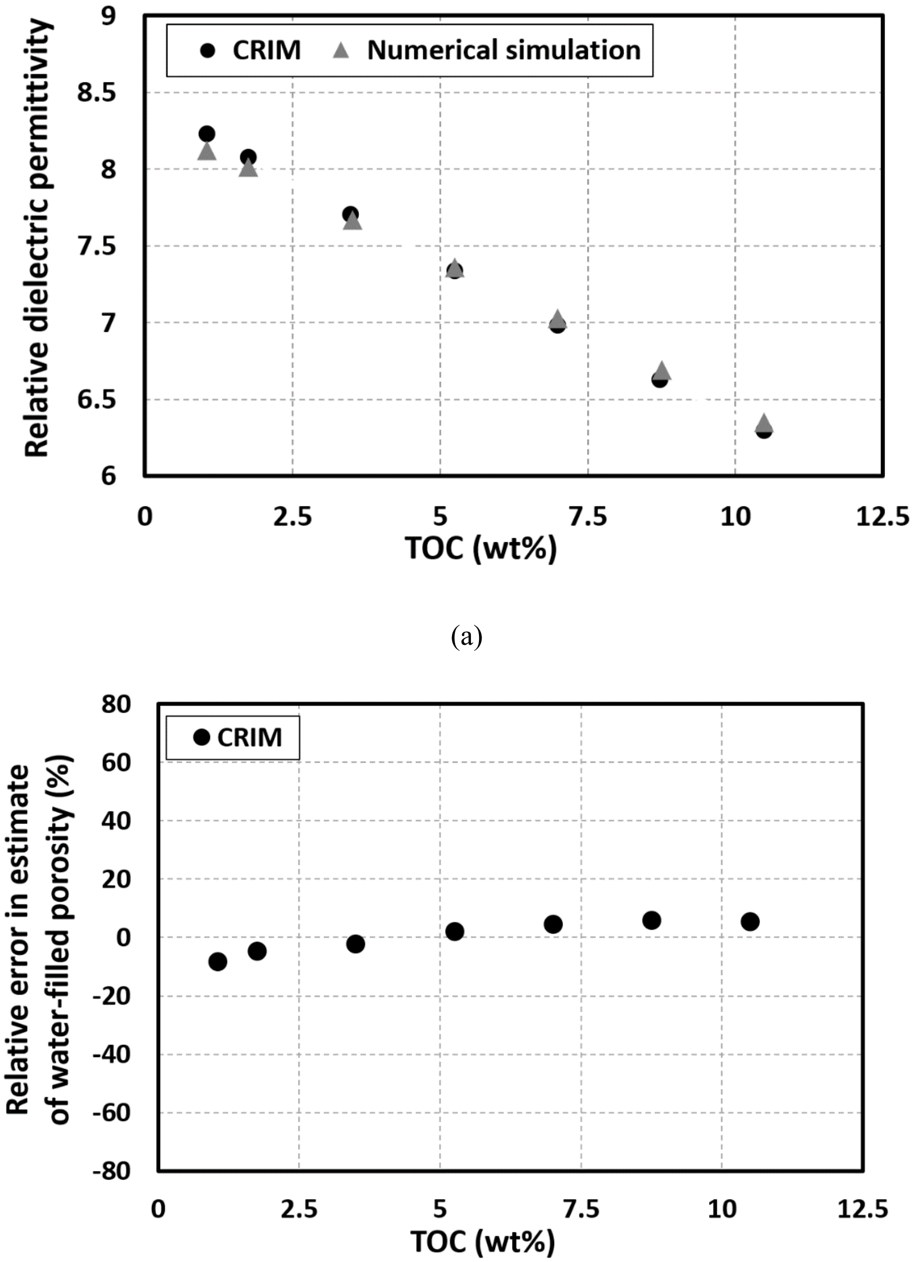

(a)

(b)

Figure 3.6: Impact of TOC on (a) the relative dielectric permittivity of the synthetic organic-rich mudrock samples and (b) the relative errors in estimates of water-filled porosity obtained from the CRIM.

3.3.3.2 Synthetic case no. 2: the impact of pyrite on relative dielectric permittivity

This set of synthetic organic-rich mudrock samples is designed to quantify the impact of volumetric concentration of the pyrite and its tortuosity on dielectric permittivity. Pyrite has a high relative dielectric permittivity value and typically exists in organic-rich formations. Because of the high relative dielectric permittivity, pyrite can influence effective relative permittivity of the rock, even with low volumetric concentration. Failure to consider the impact of pyrite can cause significant overestimation of water-filled porosity in organic-rich mudrocks.

This set of synthetic examples contains 7.5wt% TOC, 3vol% water-filled porosity, and the same spatial distribution of organic content, water, and pore space. The only variable factor in these synthetic rock samples is the pyrite. **Table 3.3** summarizes the petrophysical properties of synthetic organic-rich mudrocks in this set of examples. Pyrite is known to have a relatively high conductivity compared to other minerals. The dielectric permittivity of pyrite, $40+0.1j$, is used based on lab measurements documented in a previous publication (Peng and et al., 2014). This section quantifies the impact of (a) volumetric concentration of the pyrite and (b) spatial distribution of the pyrite network (i.e., layered vs. dispersed) on relative dielectric permittivity of the rock. Last, it quantifies the influence of the aforementioned parameters on the estimates of water-filled porosity using the CRIM and the new dielectric permittivity model.

Table 3.3: Organic-rich Mudrock, synthetic case no. 2 and 3: the assumed parameters in the petrophysical model

Parameters	Value	Units
ϕ_w	3	vol%
ϕ_k	30	vol%
ϕ	9.5	vol%
C_p	1-10	vol%
TOC	7.5	wt%
Salt concentration of formation water	35000	ppm
Formation temperature	86	^{o}F
ε_{w} @1GHz	$70+10j$	-
ε_{pyrite} @1GHz	$40+0.1j$	-
$\varepsilon_{kerogen}$ @1GHz	2.5	-
ε_{grains} @1GHz	$7.5+0.01j$	-

Figure 3.7(a) compares the impact of the volumetric concentration of pyrite on relative dielectric permittivity of the rock, estimated from the CRIM and from the numerical simulations in both dispersed and layered spatial distribution of the pyrite network. **Figure 3.7(b)** shows the relative errors in estimates of water-filled porosity obtained from the CRIM. The numerical simulation results shown in **Figure 3.7(b)** verify that failure to consider the impact of pyrite in organic-rich mudrocks results in significant overestimation of water-filled porosity using the CRIM. The error in estimates of water-filled porosity is larger in the case of layered spatial distribution of pyrite compared to the case of dispersed distribution.

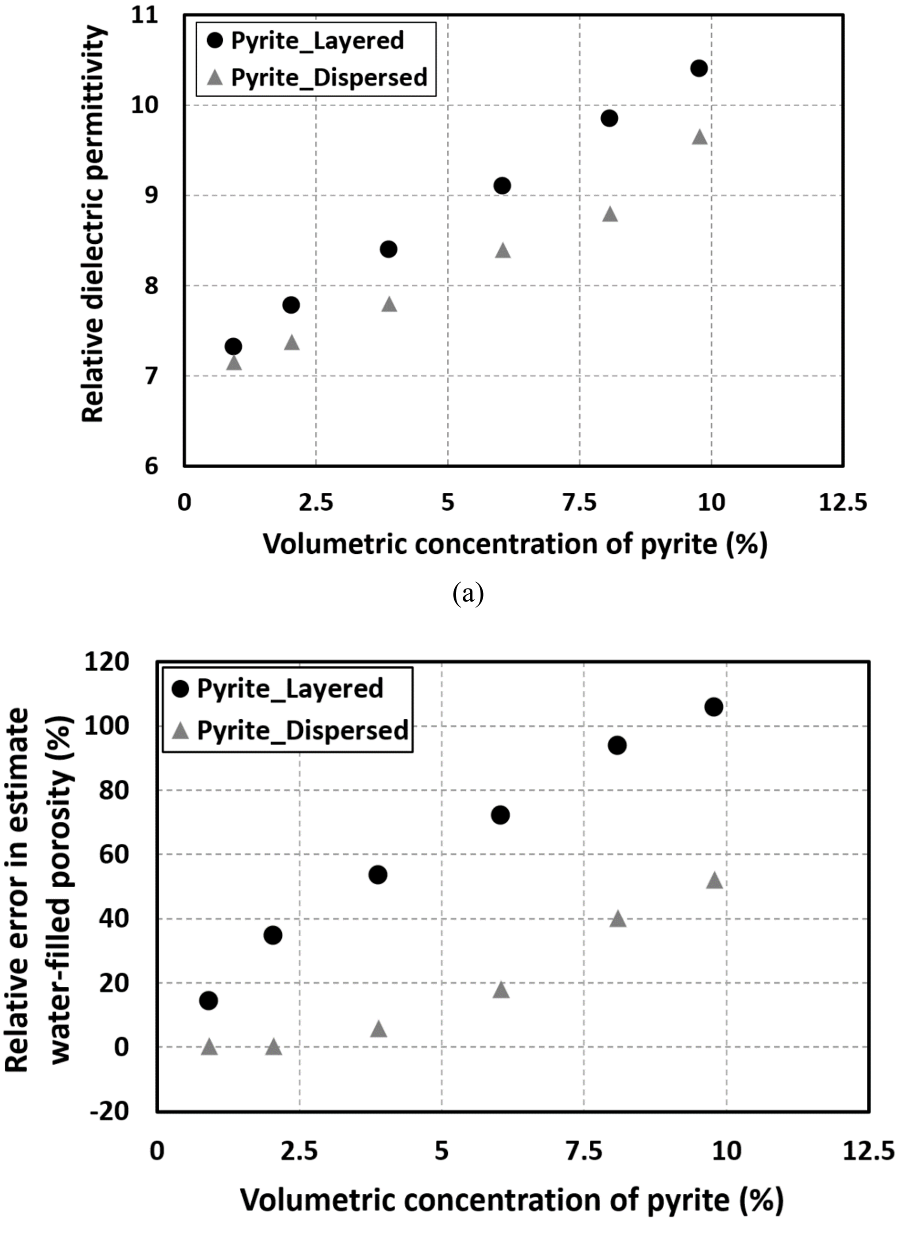

(a)

(b)

Figure 3.7: Impact of volumetric concentration of pyrite on (a) the relative dielectric permittivity of the synthetic organic-rich mudrocks and (b) the corresponding estimates of water-filled porosity using the CRIM for both the cases of layered and dispersed distributions of the pyrite network.

3.3.3.3 The impact of the pyrite network tortuosity on dielectric permittivity

Synthetic case no. 2 shows the sensitivity of dielectric permittivity measurements and the corresponding estimates of water-filled porosity to volumetric concentration and spatial distribution of pyrite network. This synthetic case aims to quantify the impact of tortuosity of pyrite network on dielectric permittivity measurements and the corresponding estimates of water-filled porosity using the CRIM and the new model. To this end, six synthetic cases is developed with the same volume and spatial distribution of the water and kerogen networks, but variable tortuosity of the pyrite network. In these cases, the volumetric concentration of pyrite is 6%.

Table 3.3 summarizes the assumed petrophysical properties of the synthetic organic-rich mudrocks in this set of examples. **Figure 3.8** illustrates the impact of pyrite network tortuosity on the relative dielectric permittivity of synthetic cases. **Figure 3.9** shows the relationship between the tortuosity-dependent coefficient and the diffusive directional tortuosity of pyrite network. The constant parameters *a*, *q* and *d* (**Figure 3.9)** are used in the new dielectric permittivity model to improve the estimates of water-filled porosity. **Figure 3.10** compares the relative error in the estimates of water-filled porosity using the CRIM and the new model. The results of numerical simulations (**Figure 3.10**) show that in the presence of 6vol% pyrite, the increase in the diffusive directional tortuosity of pyrite network causes up to a 6% decrease in the relative dielectric permittivity and up to a 64% overestimation of the water-filled porosity using the CRIM

(**Figure 3.10**). Meanwhile, the application of the new model reduces the relative errors in estimation of water-filled porosity to less than 10%.

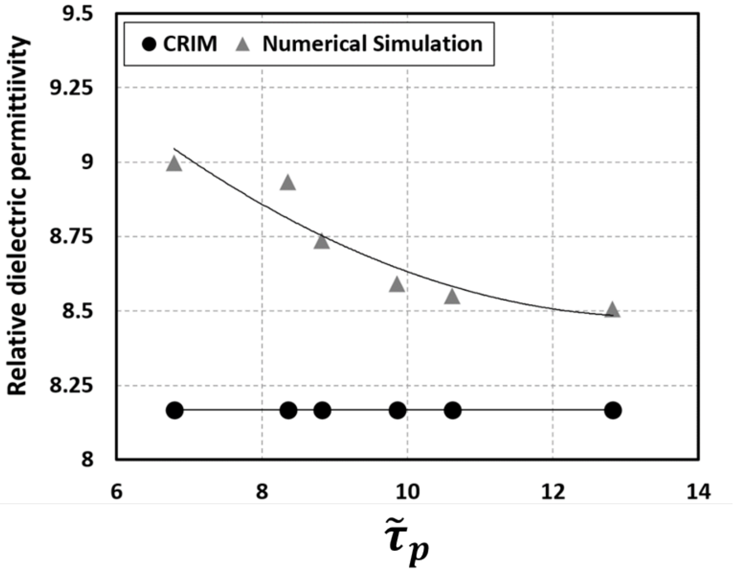

Figure 3.8: Impact of the diffusive directional tortuosity of the pyrite network on the relative dielectric permittivity of the synthetic organic-rich mudrocks along the same direction.

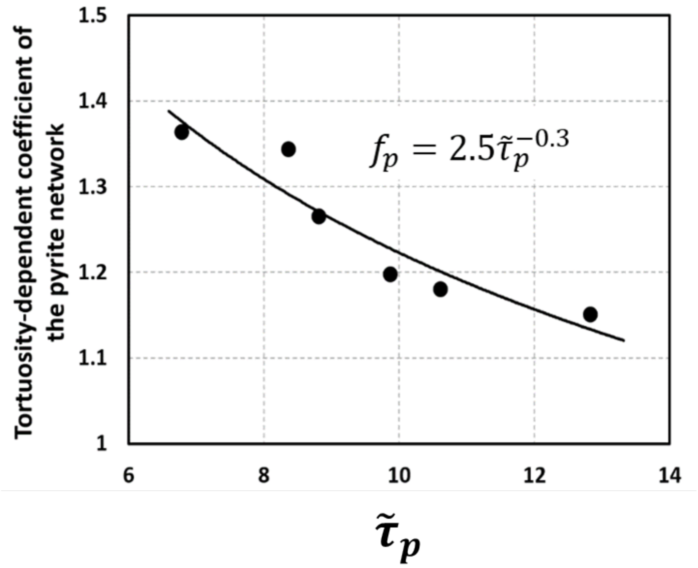

Figure 3.9: Correlation between the tortuosity-dependent coefficient and the diffusive directional tortuosity of the pyrite network in the synthetic organic-rich mudrocks.

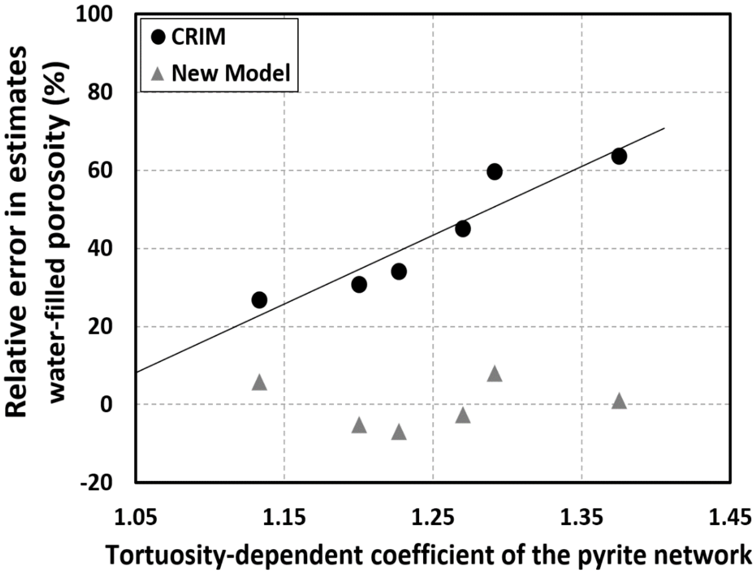

Figure 3.10: Impact of pyrite network tortuosity-dependent coefficient on the corresponding estimates of water-filled porosity in the synthetic organic-rich mudrocks using the CRIM and the new model, respectively**.**

3.4 Conclusions

This chapter quantified the impact of pore structure and spatial distribution of other rock components on effective dielectric permittivity of fluid-bearing rocks using pore-scale numerical simulations of spatial distribution of electric potential. Spatial distribution and structure of pore space and matrix components were quantified using a tortuosity factor estimated based on pore-scale images. It was shown that dielectric permittivity of the same rock along the three orthogonal directions can vary by up to 16%, while the directional tortuosity changes from 1.9 to 3 in one of the sandstone rock samples. It was observed that the pore space in the simulated carbonate samples generally more tortuous in each direction compared to the sandstone samples.

Furthermore, it was shown that the conventional CRIM for interpretation of relative dielectric permittivity and water-filled porosity are not reliable, due to failure in taking into account the impact of spatial distribution of rock components (either fluids or solid components). The relative errors are up to 27% and 26% for the sandstone and carbonate samples evaluated in this chapter, respectively, in the water-filled porosity estimated using the conventional CRIM. To improve the assessment of water-filled porosity using dielectric permittivity measurements, a new dielectric permittivity model was introduced by taking into account the diffusive directional tortuosity of the solid and fluid components of the rock samples. The new dielectric permittivity model decreases the relative error in estimates of water-filled porosity from the largest relative error of approximately 27% (using the CRIM) to less than 10% error for both sandstone and carbonate samples.

Dielectric property of synthetic organic-rich mudrocks was investigated, where the presence of organic matter and pyrite significantly affect dielectric permittivity of the rock. It has been shown that an increase in TOC from 1wt% to 10.5wt% causes a 23% decrease in dielectric permittivity. However, the impact of kerogen on estimates of water-filled porosity is not significant using the CRIM. Instead, the presence of pyrite substantially influences effective relative dielectric permittivity as well as estimates of water-filled porosity. The simulation results showed that the dielectric permittivity of organic-rich mudrocks is not only affected by the volumetric concentration of pyrite, but also by the diffusive directional tortuosity of pyrite network. It was found that with the presence of 6vol% pyrite, the increase in the directional tortuosity can result in up to a 64% overestimation of water-filled porosity by the CRIM. This error is decreased to be within 10% using the new dielectric permittivity method.

The new dielectric permittivity model introduced in this chapter relies on the input of tortuosity-dependent parameters that are used to quantify pore/grain structure. The tortuosity-dependent parameters are calculated using pore-scale rock image representatives each rock type of formations. Furthermore, this model does not take into account the effect of textual polarization. This impact can be negligible at high frequency measurements in low-salinity environments. However, in the presence of high-salinity water in a formation, the textural polarization can have a significant impact on dielectric permittivity measurements and needs to be taken into account in the interpretation method. Overall, the outcomes of this pore-scale research in this chapter are promising for improvements in interpretation of dielectric well logs in the presence of complex pore structure and variable spatial distribution of matrix constituents.

CHAPTER IV

PORE-SCALE JOINT EVALUATION OF DIELECTRIC PERMITTIVITY AND ELECTRICAL RESISTIVITY FOR ASSESSMENT OF HYDROCARBON SATURATION USING NUMERICAL SIMULATIONS[*]

Complex pore geometry and composition, as well as anisotropic behavior and heterogeneity can affect physical properties of rocks such as electrical resistivity and dielectric permittivity. The aforementioned physical properties are used to estimate *in situ* petrophysical properties of formations such as hydrocarbon saturation. In application of conventional methods for interpretation of electrical resistivity (e.g., Archie's equation and the dual-water model) and dielectric permittivity measurements (e.g., Complex Refractive Index Model, CRIM) the impacts of complex pore structure (e.g., kerogen porosity and inter-granular pores), pyrite, and conductive mature kerogen have not been taken into account. These limitations cause significant uncertainty in estimating water saturation. In this chapter, a new method is introduced that combines interpretation of dielectric and electrical resistivity measurements to improve assessment of hydrocarbon saturation. The combined interpretation of dielectric and electrical resistivity measurements enables assimilating spatial distribution of rock components (e.g., pore, kerogen, and pyrite networks) in conventional models.

---

[*] Reprinted with permission from "Assessment of Hydrocarbon Saturation in Organic-Rich Source Rocks using Combined Interpretation of Dielectric and Electrical Resistivity Measurements" by Huangye Chen and Zoya Heidari, 2014. SPE Conference Paper, 170973-MS. Copyright 2014 by the Society of Petroleum Engineers.

This chapter starts with pore-scale numerical simulations of electrical resistivity and dielectric permittivity of fluid-bearing porous media to investigate the structure of pore and matrix constituents on these measurements. The inputs to these simulators are three-dimensional (3D) pore-scale images. An analytical model is then introduced that combines resistivity and permittivity measurements to assess water-filled porosity and hydrocarbon saturation. The new joint model is applied to actual digital sandstones and synthetic digital organic-rich mudrocks. The relative errors (compared to actual value estimated from image processing) in estimates of water-filled porosity through the new joint model are all within 10% range. In the case of digital sandstone samples, the CRIM provides reasonable estimates of water-filled porosity, with only four out of twenty-one estimates beyond 10% relative error, with the maximum error of 30%. However, in the case of synthetic digital organic-rich mudrocks, six out of ten estimates for water-filled porosity are beyond 10% using the CRIM, with the maximum error of 40%. Therefore, the improvement is more significant in the case of organic-rich mudrocks with complex pore structure. In the case of synthetic digital organic-rich mudrock samples, the simulation results confirm that not only the pore structure, but also spatial distribution and tortuosity of water, kerogen, and pyrite networks, affect the measurements of dielectric permittivity and electrical resistivity. Taking into account these parameters through the joint interpretation of dielectric and electrical resistivity measurements significantly improves the assessment of hydrocarbon saturation.

4.1 Introduction

Unconventional reservoirs such as organic-rich mudrocks, contain complex pore geometry and composition, as well as a strong anisotropic and heterogeneous nature. These characteristics significantly affect physical properties such as electrical resistivity and dielectric permittivity as measured by well logs. Electrical resistivity logs are typical measurements for assessment of fluid saturations in conventional reservoirs. Conventional methods for interpreting electrical resistivity logs include resistivity-porosity-saturation models such as Archie's law (Archie, 1942) and shaly sand models such as the dual-water model (Clavier et al., 1984) and the Waxman-Smits model (Waxman and Smits, 1968). For instance, dual-water model is given by

$$\frac{1}{R_t} = \frac{\phi_t^m S_{wt}^n}{a} \cdot \left(\frac{1}{R_w} + \frac{S_{wb}}{S_{wt}} \left(\frac{1}{R_{wb}} - \frac{1}{R_w} \right) \right), \tag{4.1}$$

where R_t, R_w, R_{wb} are electrical resistivity of the rock, formation water, and clay-bound water, respectively. S_{wt} and S_{wb} are total water saturation and clay-bound water saturation, respectively. ϕ_t is the total porosity and a, m, and n are constants. The conventional resistivity-porosity-saturation models such as the one shown in **Equation 4.1**, can cause uncertainty in estimates of water saturation in organic-rich mudrocks because of the extra charge arising from other conductive component such as pyrite and mature kerogen (Passey et al., 2010; Kethireddy et al., 2014; Chen et al., 2014). Therefore, dielectric measurements have become attractive candidates to assess water/hydrocarbon saturation in organic-rich mudrocks.

Previous publications introduced methods for analyzing dielectric permittivity measurements of saturated porous media, such as the effective medium theories (Miller, 1969; Sen et al., 1981; Bussian, 1983) and volumetric models (Calvert and Wells, 1977; Wharton et al., 1980; Dahlberg and Ference, 1984; Pride, 1994; Linde et al., 2006). Among the conventional methods, the Complex Refractive Index Model (CRIM) (Birchack et al., 1974; Dobson et al., 1985; Roth et al., 1990; Heimovaara et al., 1994) is one of the typically used methods for interpretation of dielectric measurements. The CRIM model is reliable at frequency larger (e.g., > 1GHz) where interfacial polarization is negligible (Donadille and Faivre, 2015; Hizem et al., 2008; West et al., 2003). However, interpretation of dielectric measurements can be challenging because none of the conventional models takes into account the impacts of complex pore structure and spatial distribution of solid and fluid components on dielectric properties of the rock. Chapter III has shown that the use of conventional volumetric dielectric permittivity methods could result in up to 22% overestimate of water-filled porosity compared to the actual value in conventional sandstone and carbonate formations, because of complex pore structure and rock fabric. Unconventional organic-rich mudrocks are typically even more heterogeneous and anisotropic compared to conventional formations. Organic-rich mudrocks usually consist of complex lithology and show highly variable spatial distribution of water, kerogen, and pyrite networks. All of these factors affect electrical resistivity and dielectric permittivity measurements in unconventional formations. Thus, a reliable method is needed for accurate assessment of fluid saturations using electrical resistivity and dielectric measurements.

Electrical resistivity and high-frequency dielectric permittivity are both affected by rock fabric (e.g., spatial distribution of each rock component) and pore structure (e.g., tortuosity and pore network connectivity). Thus, a combined interpretation of electrical resistivity and dielectric permittivity is a powerful tool to estimate rock fabric, fluid saturation, and soil salinity (Malicki and Walczak, 1999; Binley et al., 2001; Hamed et al., 2003; Linde et al., 2006). Brovelli and Cassiani (2011) developed an analytical model to estimate the effective dielectric permittivity of the rock by combining the Hashin Shtrikman bounds and Archie's law. However, their model might not be suitable for estimating water-filled porosity in organic-rich mudrocks, because first it does not take into account spatial distribution of rock components and pore network. Second, it does not take into account the impact of conductive components in organic rich mudrocks such as mature kerogen and pyrite on electrical resistivity and dielectric permittivity of the rock. Passey et al. (2010) showed that electrical resistivity in high thermally mature organic-rich source rocks can be 1-2 orders of magnitude less than that of the same formation with a low thermal maturity zone. The low resistivity values in shale can lead to significant underestimation of hydrocarbon saturation, if conventional models are applied for interpretation of resistivity logs (Kethireddy et al., 2014). Meng et al. (2012) and Rajeshwar et al. (1980) indicated that the thermal maturity of kerogen might affect the conductivity of organic-rich mudrocks as a function of temperature. Furthermore, Mao et al. (2010) indicated a correlation between thermal maturity and aromaticity from solid-state nuclear magnetic resonance (NMR) studies on kerogen. Walters et al. (2014) observed that graphite-like turbostratic nanostructures are proportionally more prevalent in the electrically conductive highly mature shale samples. These studies indicate the possible presence of graphite-like nano-scale features in highly mature kerogen. Consequently, the highly mature kerogen might provide graphite-like electrical properties including presence of delocalized electrons, which makes the interpretation of electrical resistivity measurements challenging.

Chapter III proposes a new dielectric permittivity model that incorporates the diffusive directional tortuosity. In the new dielectric permittivity model, the effective relative dielectric permittivity of the rock along the *i* direction, ε_i, is given by

$$\sqrt{\varepsilon_i} = \begin{bmatrix} f_{w,i} S_w \phi_t \sqrt{\varepsilon_w} + f_{HC,i}(1 - S_w)\phi_t \sqrt{\varepsilon_{HC}} + f_{k,i} C_k \sqrt{\varepsilon_k} \\ + f_{p,i} C_p \sqrt{\varepsilon_p} + f_{g,i}(1 - S_w \phi_t - C_k - C_p)\sqrt{\varepsilon_g} \end{bmatrix}, \tag{4.2}$$

where ε_w, ε_{HC}, ε_p, ε_k, ε_g are the relative dielectric permittivity values of water, hydrocarbon, pyrite, kerogen and non-conductive grains, respectively. S_w is the water saturation, ϕ_t is the total porosity, and C_k and C_p are the volumetric concentrations of kerogen and pyrite, respectively. $f_{w,i}$ is the tortuosity-dependent coefficient of the water network in the *i* direction and can be defined as

$$f_{w,i} = a_w \tilde{\tau}^{q_w}{}_{w,i} + d_w, \tag{4.3}$$

where $\tilde{\tau}_{w,i}$ is the diffusive directional tortuosity of the water network in the *i* direction, a_w, q_w and d_w are the coefficients determined by the structure of water network. The same definition applies to hydrocarbon, kerogen, pyrite, and non-conductive grains. Because the relative dielectric permittivity of water and pyrite are higher than that of hydrocarbon and non-conductive grains, we can usually assume that f_{HC} and f_g are equal to one. f_k is also close to one when kerogen is not highly mature. Chapter III shows that this new model improves the estimates of water-filled porosity in both conventional and unconventional reservoirs compare to the CRIM.

In this chapter, we propose a new method that combines electrical resistivity and dielectric permittivity measurements to improve the assessment of water-filled porosity. The following sections include the detailed description of the proposed method, as well as application of the method to digital sandstone and synthetic digital organic-rich mudrock samples.

4.2 Method

This section summarizes the method used to do the joint interpretation of both the electrical resistivity and dialectical permittivity measurements to improve the accuracy of estimation of water-filled porosity. The concept of 3D pore-scale digital rock is introduced in Chapter II, Subsection 2.2.1, and the petrophysical models for digital rocks are described in Chapter II, Subsection 2.2.2. Diffusive directional tortuosity (Chapter II, Subsection 2.2.3) is used to validate the concept of electrical directional tortuosity in this chapter. The frequency of dielectric measurements is 1 GHz, and the effective relative dielectric permittivity is numerically simulated based on 3D pore-scale images by solving the Laplace's equation in the frequency domain (Chapter III, Subsection 3.2.2). The following subsections first define electrical directional tortuosity, and then proposed a new interpretation method that combines electrical resistivity and dielectric permittivity to estimate water-filled porosity and water/hydrocarbon saturation. At the end is found the workflow for the study on quantifying the complexity of pore and grain structure and its impact on the combined interpretation of the electric resistivity and dielectric permittivity measurements for rock samples.

4.2.1 Electrical directional tortuosity

As introduced in Chapter II, the directional connectivity of the *j*th conductive component along the *i* direction (X, Y, or Z) can be written as

$$\Psi_{i,j} = \frac{C_j}{\alpha(\tilde{\tau}_{j,i})^{\beta}} = \frac{(\sigma_{t,j})_i}{\sigma_j}, \tag{4.4}$$

where C_j is the volumetric concentration of the *j*th conductive component, and $\tilde{\tau}_{j,i}$ is the diffusive direction tortuosity of the *j*th conductive component along the *i* direction. *j* can be any rock component such as water, pyrite, or kerogen. σ_j and $\sigma_{t,j}$ represent the conductivity of the *j*th conductive component and the part of total conductivity of the rock sample contributed by the *j*th conductive component, respectively. α and β are constant parameters that are dependent on pore geometry, shapes, and rock fabric. The parameters α and β are close to one in the examples presented in this chapter.

The electrical directional tortuosity of the *j*th conductive component along the *i* direction is obtained via

$$\tau_{j,i} = \frac{C_j}{\psi_{j,i}}. \tag{4.5}$$

After substituting **Equation 4.4** in **Equation 4.5**, the electrical directional tortuosity can be estimated via

$$\tau_{j,i} = \alpha(\tilde{\tau}_{j,i})^{\beta} = \frac{\sigma_j C_j}{(\sigma_{t,j})_i}. \tag{4.6}$$

4.2.2 Combined interpretation of electrical resistivity and dielectric permittivity for water saturation assessment

Chapter III proposes a new dielectric permittivity model which improves assessment of water saturation by taking into account the diffusive directional tortuosity of pore space and matrix components. In this chapter, we take a step further and combine interpretation of electrical resistivity and dielectric permittivity measurements. To this end, we introduce a new joint model that includes electrical resistivity measurements as indicators of directional tortuosity of pore network for assessment of water saturation. The addition of electrical resistivity measurements enables quantifying directional tortuosity of pore network (in the presence of directional resistivity measurements), which is required to be taken into account in interpretation of dielectric measurements for assessment of water/hydrocarbon saturation.

First, **Equation 4.3** is generalized as

$$f_{j,i} = a_j(\tilde{\tau}_{j,i})^{q_j} + d_j, \tag{4.7}$$

where a_j, q_j, and d_j are the coefficients determined by the spatial distribution of the jth component network. The electrical directional tortuosity of the water network along the i direction, $\tau_{w,i}$, is then calculated using **Equation 4.6** via

$$\tau_{w,i} = \alpha(\tilde{\tau}_{w,i})^{\beta} = \frac{\sigma_w \phi_t S_w}{(\sigma_{t,w})_i}. \tag{4.8}$$

where w stands for water. After substituting **Equations 4.8** and **4.3** into **Equation 4.2**, we have

$$\begin{aligned}\sqrt{\varepsilon_i} &= (e_w \left(\frac{\sigma_w \phi_t S_w}{(\sigma_{t,w})_i} \right)^{b_w} + d_w)\phi_t S_w \sqrt{\varepsilon_w} + f_{HC,i}(1 - S_w)\phi_t \sqrt{\varepsilon_{HC}} + f_{k,i} C_k \sqrt{\varepsilon_k} \\ &+ f_{p,i} C_p \sqrt{\varepsilon_p} + f_{g,i}(1 - \phi_t - C_k - C_p)\sqrt{\varepsilon_g}\end{aligned} \tag{4.9}$$

where $e_w, b_w,$ and d_w are coefficients determined by the structure of the water network. These parameters can be obtained by core calibration for different rock types. It is assumed that they remain almost constant in each rock type, where rock fabric and spatial distribution of rock components remain the same. Because $\varepsilon_{\mathrm{w}} >> \varepsilon_{HC}$, $\varepsilon_{\mathrm{w}} >> \varepsilon_g$, and $\varepsilon_{\mathrm{w}} >> \varepsilon_k$, we assume that f_{HC}, f_g, and f_k are close to one. In the presence of pyrite, $f_{p,i}$ is computed via **Equation 4.7** and approximate $(\sigma_{t,w})_i$ by

$$(\sigma_{t,w})_i = (\sigma_t)_i - \frac{\sigma_p C_p}{\tilde{\tau}_{p,i}}. \tag{4.10}$$

In the case of digital sandstone samples, there is no pyrite and kerogen. Thus, **Equation 4.9** can be further simplified by assigning zero values to C_k and C_p.

Equation 4.9 is used to estimate water-filled porosity. Hydrocarbon saturation can finally be estimated via

$$S_{HC} = 1 - \frac{\phi_w}{\phi_t}, \tag{4.11}$$

where S_{HC} is hydrocarbon saturation. The new joint model incorporates parameters which quantify the structure and directional connectivity of all the conductive components of the rock, which is important to be taken into account in rock samples with significant anisotropic properties.

4.2.3 Workflow

Figure 4.1 shows the workflow for quantifying the complexity of pore and grain structure and its impact on the combined interpretation of the electric resistivity and dielectric permittivity measurements for rock samples. In this research, 3D pore-scale rock images are first generated from rocks of different formations. Next, electrical and dielectric properties are assigned to each rock component as an input into the pore-scale numerical simulation. The outputs of the numerical simulations include effective electric resistivity and dielectric permittivity of the rocks, and electrical directional tortuosity of the pore and grain network. The research concludes with a proposed electrical resistivity/dielectric permittivity joint interpretation model that incorporates the electrical directional tortuosity of the pore and grain structures to improve the assessment of water-filled porosity.

4.3 Results

This section shows the application of the introduced method on examples of actual digital sandstones and synthetic digital organic-rich mudrocks to demonstrate the performance of the model for assessment of water-filled porosity in rocks with different pore structures and matrix components. The resistivity and dielectric permittivity are numerically simulated from these digital rock samples.

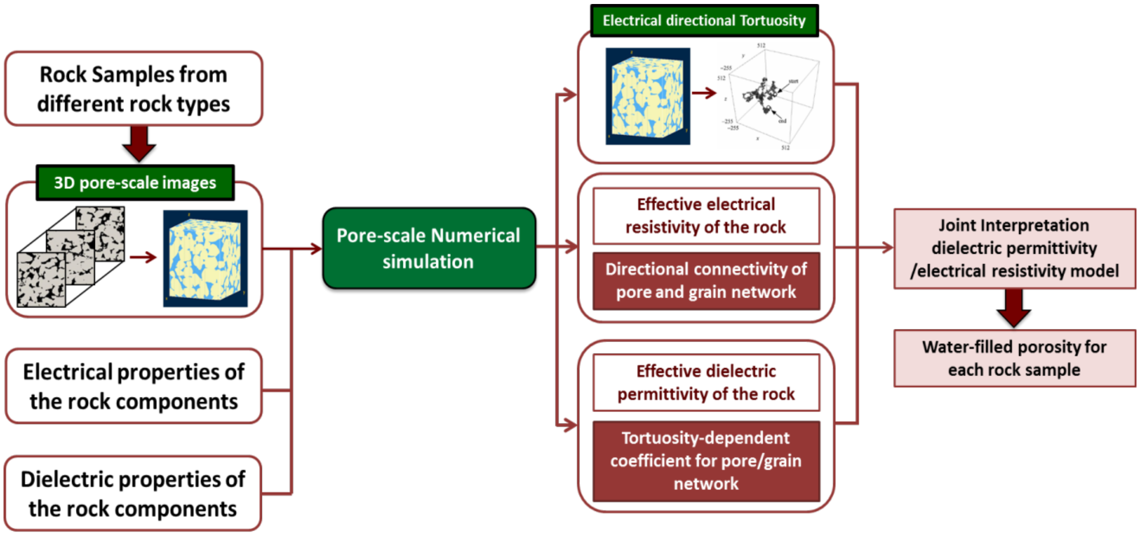

Figure 4.1: The workflow for the study on quantifying the complexity of pore and grain structure and its impact on the combined interpretation of the electric resistivity and dielectric permittivity measurements of rock samples.

4.3.1 Validation of dielectric permittivity numerical simulations using laboratory experiments

The reliability of the developed numerical simulator for assessment of effective dielectric permittivity is validated in the case of Berea sandstone. Dielectric permittivity is numerically estimated in a 3D pore-scale digital image of a Berea sandstone sample when it is fully saturated with distilled water and when it was dried. The laboratory measurements of dielectric permittivity on the same samples are carried out. **Figure 4.2** shows the Berea sandstone core sample and its 3D pore-scale digital image obtained from a micro CT-scanner. **Figure 4.3** compares the dielectric constant values estimated from numerical simulations against those measured in the laboratory in both cases of dry and fully water saturated rock samples. The results confirm that the dielectric constant values obtained from numerical simulations are in agreement with laboratory measurements with relative errors of less than 5%.

4.3.2 Sandstone rock samples

3D CT-scan images (Dong, 2007) of seven sandstone rock samples are used which have different total porosity (fully water saturated) and diffusive directional tortuosity of the pore network. These seven sandstone rock samples are denoted by S1 to S7. **Table 4.1** lists the assumed petrophysical properties used for the numerical simulations.

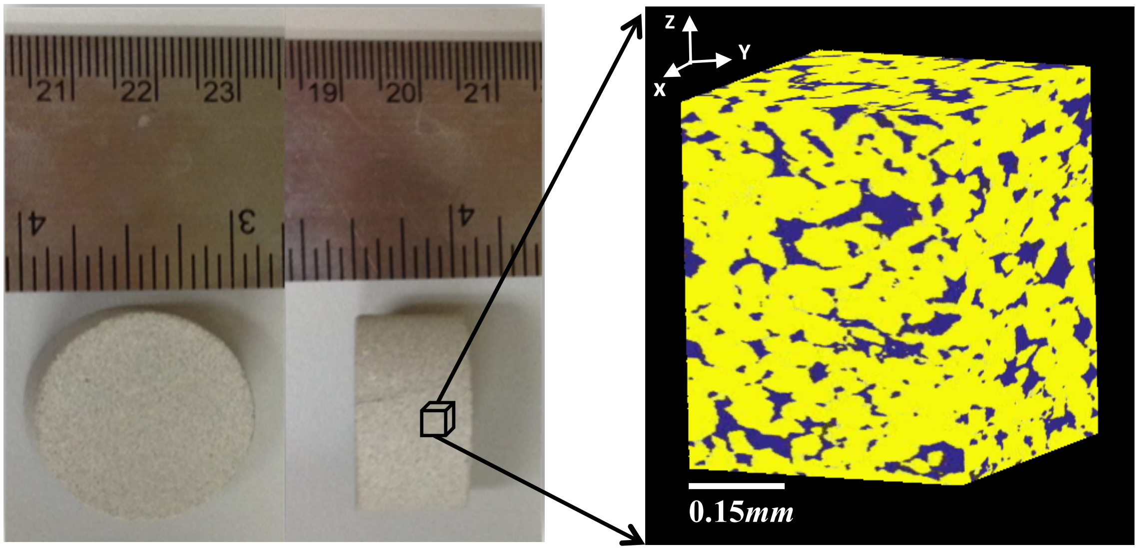

Figure 4.2: Berea sandstone core samples used for laboratory measurements and the 3D pore-scale CT-scan image taken from these rock samples. Blue and yellow regions represent the grain and pore space, respectively.

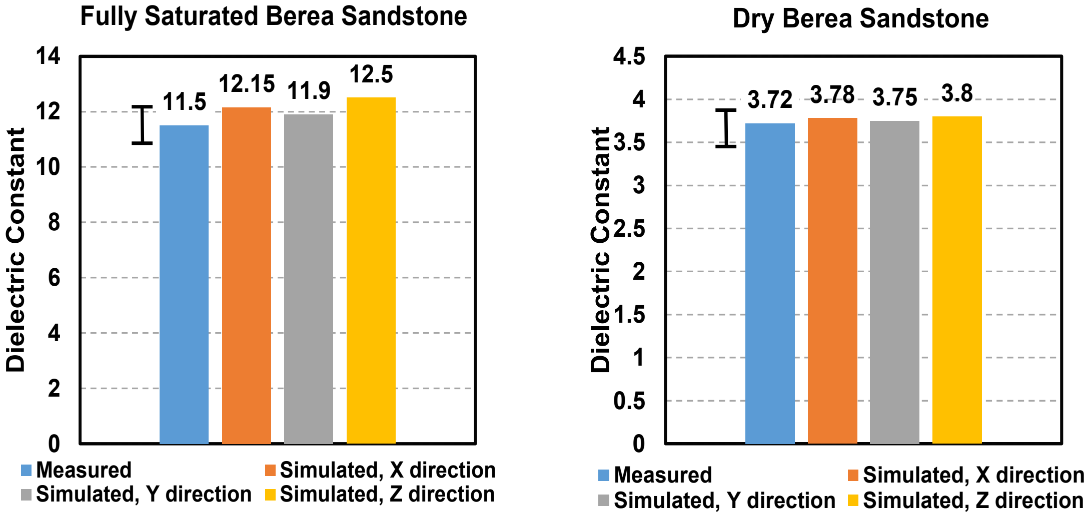

(a) (b)

Figure 4.3: Comparison of dielectric constant of the Berea sandstone obtained from numerical simulation and laboratory measurements in (a) dry rock samples, (b) fully water saturated rock samples.

Table 4.1: Sandstone rock samples: summary of the assumed petrophysical properties.

Parameters	Value	Units
Electrical conductivity of formation water at 175 ^{o}F	20	S/m
Electrical conductivity of non-conductive grains at 175 ^{o}F	0	S/m
Electrical conductivity of hydrocarbon at 175 ^{o}F	0	S/m
Dielectric permittivity of formation water at 1 GHz	$76+10i$	-
Dielectric permittivity of non-conductive grains at 1 GHz	$4.65+0.1i$	-
Dielectric permittivity of hydrocarbon at 1 GHz	1	-
Salt concentration of formation water	60	Kppm
Size of digital sandstone rock samples	465 x 465 x 465	μm
Mesh grid of digital sandstone rock samples	120 x 120 x 120	-

The diffusive directional tortuosity of all seven sandstone samples along the X, Y, and *Z* directions are first numerically calculated using the algorithm introduced by Nakashima and Kamiya (2007). The effective electrical resistivity and the effective relative dielectric permittivity of these samples in the X, Y, and Z directions are then calculated by solving the Laplace's equation of **Equations 2.20** and **3.5**. **Figure 4.4** shows the correlation between the electrical directional tortuosity (**Equation 4.6**) and the diffusive directional tortuosity (**Equation 2.14**) of the water network in these seven rock samples. This correlation is given by

$$\tau_w = (\tilde{\tau}_w)^{0.95}, \tag{4.12}$$

which provides the coefficients α and β in **Equation 4.8** equal to 1 and 0.95 for all seven sandstone samples, respectively.

Table 4.2 summarizes rock properties and the simulation results for all the sandstone rock samples, including the total porosity, ϕ_t, the effective electrical resistivity, Rt, the effective relative dielectric permittivity, ε, and the electrical directional tortuosity in the X, Y, and Z directions. It is observed that the electrical resistivity increases with the increase in the electrical directional tortuosity (**Table 4.2**). Results show as well that the amplitude of the complex relative dielectric permittivity decreases with the increase in the electrical directional tortuosity.

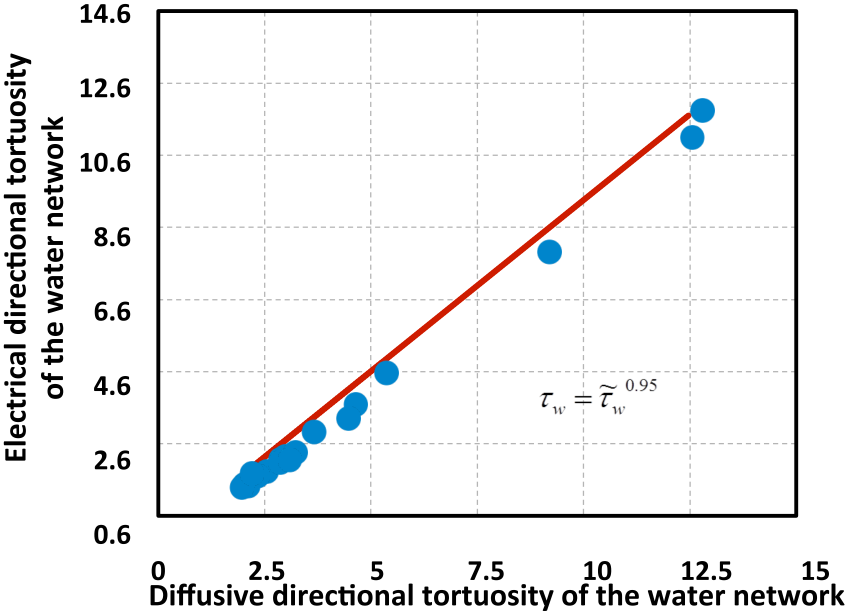

Figure 4.4: Sandstone rock samples: the correlation between the electrical directional tortuosity and the diffusive directional tortuosity of the water network in the seven rock samples (in the X, Y, and Z directions).

Figure 4.5 shows the correlation between the electrical directional tortuosity and the tortuosity-dependent coefficient. This cross plot is used to estimate the parameters e_w, b_w, and d_w in our new model as 0.68, -0.95, and 0.69, respectively. Next, the new joint model is applied to estimate the water-filled porosity of these sandstone rock samples. **Figure 4.6** compares the estimates of the water-filled porosity obtained from the new model and the ones from the CRIM.

Table 4.2: Sandstone rock samples: total porosity, ϕ_t, effective DC electrical resistivity, R_t, effective relative dielectric permittivity, ε, and electrical directional tortuosity of the water network, τ_w, in the X, Y, and Z directions.

Sample	**Dir.**	$\boldsymbol{\phi_t}$	$\boldsymbol{R_t}$ **(ohm-m)**	$\boldsymbol{\varepsilon}$	$\boldsymbol{\tau_w}$
S1	X	0.22	0.59	$12.98+1.08i$	2.90
	Y	0.22	0.50	$14.00+1.24i$	2.47
	Z	0.22	0.82	$11.50+0.86i$	4.34
S2	X	0.24	1.69	$10.45+0.77i$	8.92
	Y	0.24	2.33	$10.45+0.62i$	12.17
	Z	0.24	2.48	$10.40+0.60i$	12.41
S3	X	0.37	0.36	$18.47+1.73i$	2.78
	Y	0.37	0.35	$18.28+1.70i$	2.78
	Z	0.37	0.26	$20.67+2.11i$	1.96
S4	X	0.21	0.43	$14.26+1.32i$	2.05
	Y	0.21	0.78	$11.54+0.88i$	3.55
	Z	0.21	0.65	$12.11+0.97i$	3.13
S5	X	0.27	0.39	$15.90+1.50i$	2.27
	Y	0.27	0.33	$17.00+1.68i$	1.91
	Z	0.27	0.47	$14.68+1.29i$	3.00
S6	X	0.18	1.37	$9.62+0.63i$	5.10
	Y	0.18	1.38	$9.63+0.63i$	5.20
	Z	0.18	0.61	$12.06+1.01i$	2.14
S7	X	0.21	0.98	$11.22+0.80i$	4.42
	Y	0.21	0.97	$11.30+0.83i$	4.50
	Z	0.21	0.96	$11.36+0.81i$	4.60

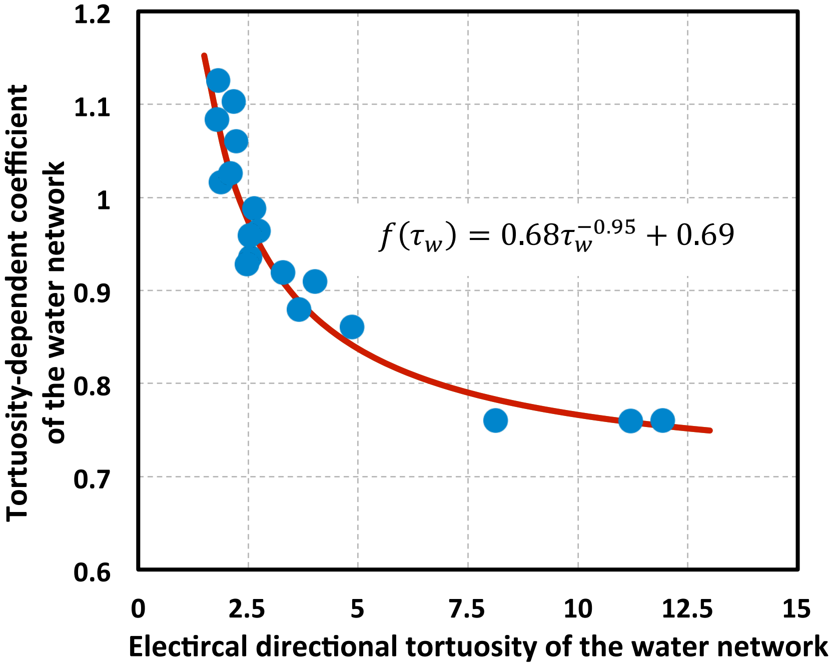

Figure 4.5: Sandstone rock samples: the correlation between the estimated tortuosity-dependent coefficient and the simulated electrical directional tortuosity of the water network in the seven rock samples (in the X, Y, and Z directions).

The errors in estimates of water-filled porosity using the new model are less than those obtained from the CRIM. The relative errors in estimates of water-filled porosity in all the samples are less than 10% when using the new model. The CRIM leads to relative errors of up to 30% in one of the cases. The largest error from the CRIM corresponds to the S2 rock sample, for which the electrical directional tortuosity values in the X, Y, and Z directions are 8.92, 12.17, and 12.41, respectively. Such large errors in estimates of water-filled porosity using the CRIM can be due to the strong anisotropic behavior of this sample and the fact that the CRIM does not take into account the anisotropic properties of the pore and grain structure. The errors observed in estimates of water-filled porosity in sandstone examples can be significantly increased in the formations with more complex pore/grain geometry and dominant anisotropic behavior.

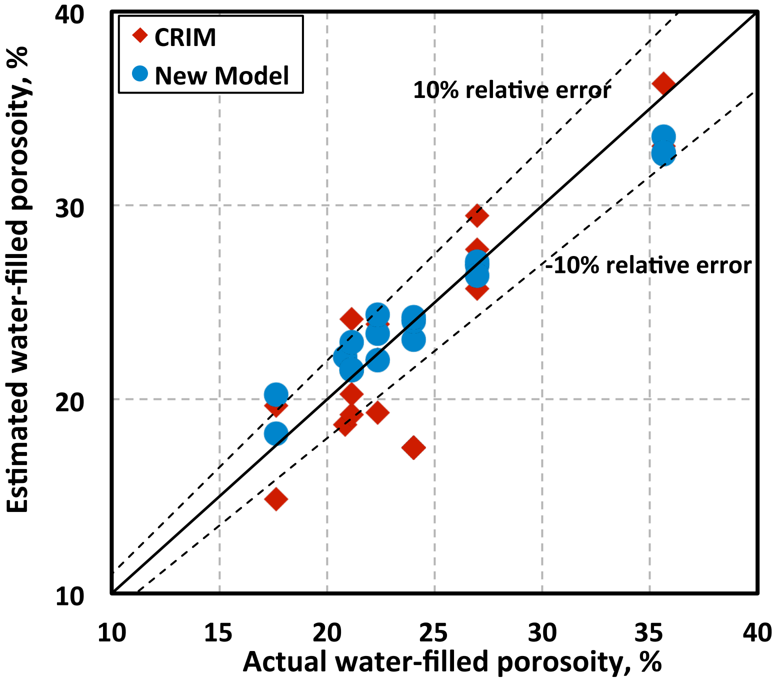

Figure 4.6: Sandstone rock samples: the comparison of the estimates of water-filled porosity obtained from the new model (blue dots) and the CRIM (red dots). The two dashed black lines represent the +10% and -10% relative error lines in estimates of water-filled porosity.

4.3.3 Synthetic organic-rich mudrock samples

Compared to conventional sandstone rocks, organic-rich mudrocks incorporate more anisotropic and heterogeneous properties. To investigate the performance of the new method on organic-rich mudrocks, organic-rich rock samples are synthesized which contain water, hydrocarbon, pyrite, non-conductive grains, and hydrocarbon-bearing kerogen components. **Table 4.3** summarizes the assumed petrophysical properties used in numerical simulations for these samples. The following subsections document the application of the new model to synthetic digital cases where (a) kerogen is not conductive, (b) kerogen is highly mature and conductive, and (c) pyrite is present. This section first compares the results from the new joint model against those from the CRIM. Next, it quantifies the impact of the tortuosity of the kerogen and pyrite networks on estimates of water saturation obtained from the new joint model and conventional models.

Table 4.3: Synthetic digital organic-rich mudrock samples: summary of the assumed petrophysical properties.

Parameters	Value	Units
Electrical conductivity of formation water at 175 ^{o}F	20	S/m
Electrical conductivity of non-conductive kerogen network at 175 ^{o}F	0	S/m
Electrical conductivity of conductive kerogen network at 175 ^{o}F	0.015	S/m
Electrical conductivity of pyrite at 175 ^{o}F	0.5	S/m
Electrical conductivity of non-conductive grains at 175 ^{o}F	0	S/m
Dielectric permittivity of formation water at 1 GHz	$76+10i$	-
Dielectric permittivity of non-conductive grains at 1 GHz	$4.65+0.1i$	-
Dielectric permittivity of hydrocarbon at 1 GHz	1	-
Dielectric permittivity of kerogen at 1 GHz	3.3	-
Dielectric permittivity of pyrite at 1 GHz	$40+i$	-
Salt concentration of formation water	60	Kppm
Water-filled porosity	1.6 to 3.3	vol%
Kerogen porosity	30	vol%
Size of synthetic digital mudrock samples	1.2x1.2x1.2	μm
Mesh grid of synthetic digital mudrock samples	120 x 120 x 120	-

4.3.3.1 The new joint model vs. the CRIM

This section compares the results of water saturation obtained from the new joint model against those from the CRIM in synthetic digital organic-rich mudrocks. Ten synthetic digital organic-rich mudrocks examples are built with different water saturation ranging from 16% to 27% and the same volumetric concentration of kerogen network of 30%. There is no pyrite in these synthetic digital cases, and spatial distribution of the kerogen network is kept the same in all ten cases. The use of synthetic digital rock models enables better control on properties of the rock for sensitivity analysis. The numerical simulations are performed for both situations: (a) kerogen is not conductive and (b) kerogen is conductive. To implement the new joint model, the coefficients, e_w, b_w, and d_w need to be first estimated. The results from numerical simulations (**Figure 4.7**) in the case of non-conductive kerogen are used to calculate e_w, b_w, and d_w. **Figure 4.7** shows the correlation between the electrical directional tortuosity and the tortuosity-dependent coefficient of the water network. This cross-plot provides the parameters e_w, b_w, and d_w in the new joint model as 0.95, -0.68, and 0.93, respectively. There shows a significant difference between these constant parameters in the sandstone and organic-rich mudrock samples (parameters e_w, b_w, and d_w are equal to 0.68, -0.95, and 0.69, respectively, for the sandstones samples), which is due to the difference in their pore structure.

Figure 4.8 compares the water saturation estimated by the CRIM against to that from the new model. The absolute relative errors in estimates of water saturation using the new model for all ten samples are less than 10%, no matter whether the kerogen is conductive or non-conductive. When using the CRIM, the relative errors in six of the ten samples are beyond 10%, and the relative errors in four samples are larger than 30%. In the previously described sandstone samples, the CRIM provided reasonable results in the estimates of water saturation with relative errors of less than 10% in most of the cases. However, the CRIM did not provide reliable estimates of water saturation in organic-rich mudrocks because of their strong anisotropic properties.

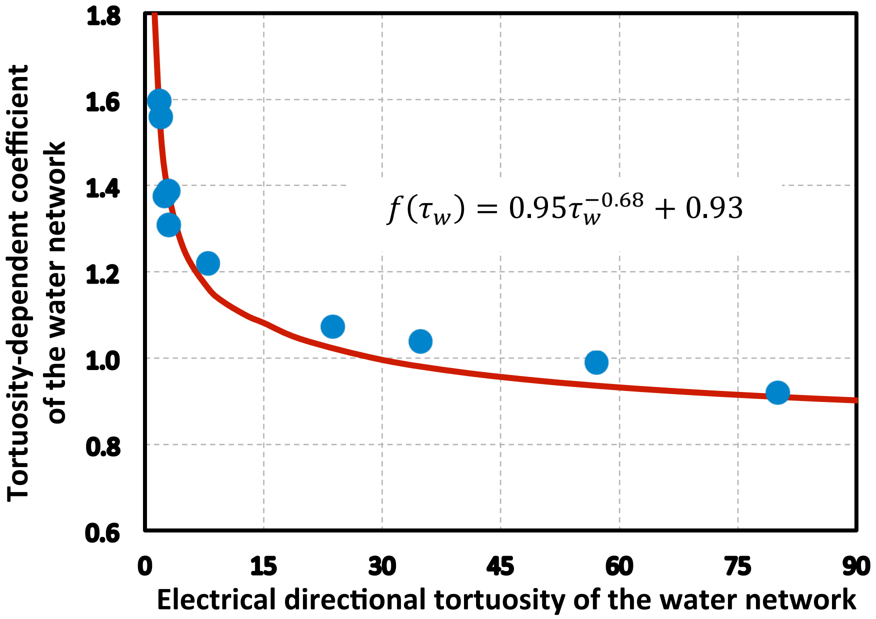

Figure 4.7: Synthetic digital organic-rich mudrock examples including non-conductive kerogen: the correlation between the estimated tortuosity-dependent coefficient and the simulated electrical directional tortuosity of the water network.

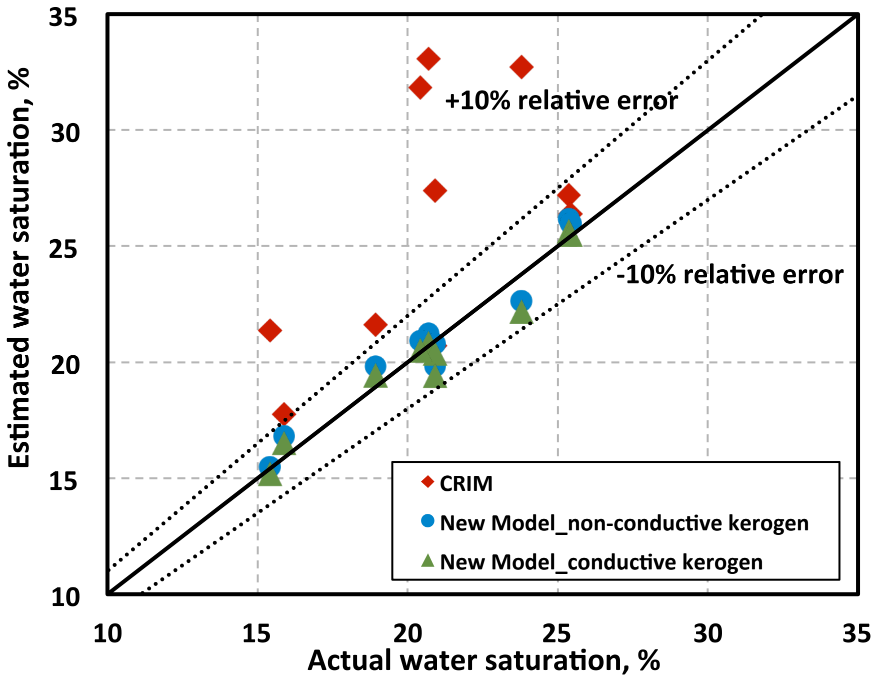

Figure 4.8: Synthetic digital organic-rich mudrock examples including conductive or non-conductive kerogen: the comparison of the new model (blue and green dots) and the CRIM (red dots) in estimates of water saturation. The two dashed black lines represent the +10% and -10% relative error lines in estimates of water saturation.

4.3.3.2 Impact of tortuosity of the kerogen network on estimates of water saturation

A set of digital organic-rich mudrocks is synthesized with the same water saturation (i.e., 21%) and spatial distribution, but different diffusive directional tortuosity of the kerogen network. The volumetric concentration of kerogen network is 30% in all the samples. **Figure 4.9** shows the electrical resistivity and the relative dielectric permittivity values for this set of rock samples in the cases where (a) kerogen is highly mature and conductive and (b) kerogen is not conductive. It is observed that the diffusive directional tortuosity of the kerogen network affects the electrical resistivity measurements when kerogen is conductive. The electrical resistivity of the rock samples increases from 87 ohm-m to 98 ohm-m (i.e., 13% increase), with the increase of the diffusive directional tortuosity of the kerogen from 1.9 to 4.3. In the case of non-conductive kerogen, the electrical resistivity remains constant, when the diffusive directional tortuosity varies in different samples. Furthermore, it is observed that the diffusive directional tortuosity of the kerogen network has a negligible impact on dielectric permittivity of the rock. With an increase of the diffusive directional tortuosity of the kerogen network from 1.9 to 4.3, the relative dielectric permittivity decreases slightly from 4.61 to 4.58 (1% decrease).

Next, the impact of the directional tortuosity of the kerogen network is investigated on estimates of water saturation by using the new dielectric permittivity model (**Equation 4.9**). **Figure 4.10** shows the impact of the diffusive directional tortuosity of the kerogen network on the relative errors in estimates of water saturation by the new dielectric permittivity model and the CRIM in ten synthetic digital samples. It is observed that with the increase of the diffusive directional tortuosity of the kerogen network from 1.9 to 4.3, the relative error in estimates of water saturation using the new model decreases from a 2.3% overestimation to a 1.5% underestimation, if kerogen is assumed to be conductive. These errors are significantly less than those obtained using the CRIM (i.e., in the range of 13% to 9%). The difference between the errors from the CRIM and the new joint model is associated with the water network structure, which is not taken into account in the CRIM. This difference if not significantly affected by the presence of kerogen, because of the negligible impact of kerogen network on dielectric permittivity compared to the water network.

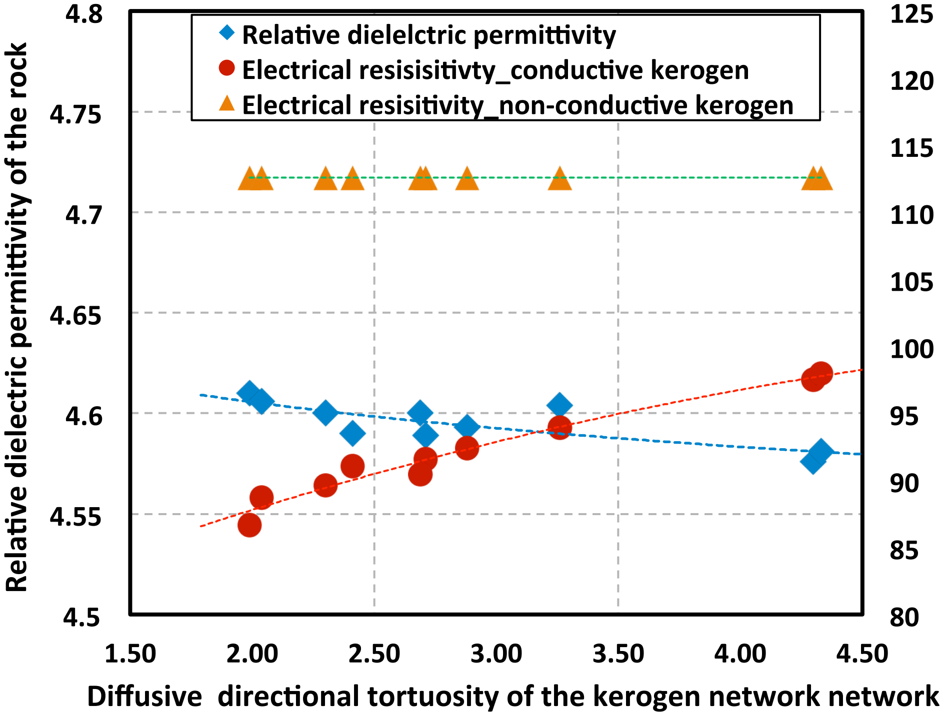

Figure 4.9: Synthetic digital organic-rich mudrock examples including conductive or non-conductive kerogen: impact of diffusive directional tortuosity of the kerogen network with 21% water saturation on electrical resistivity (orange and red dots) and relative dielectric permittivity (blue dots).

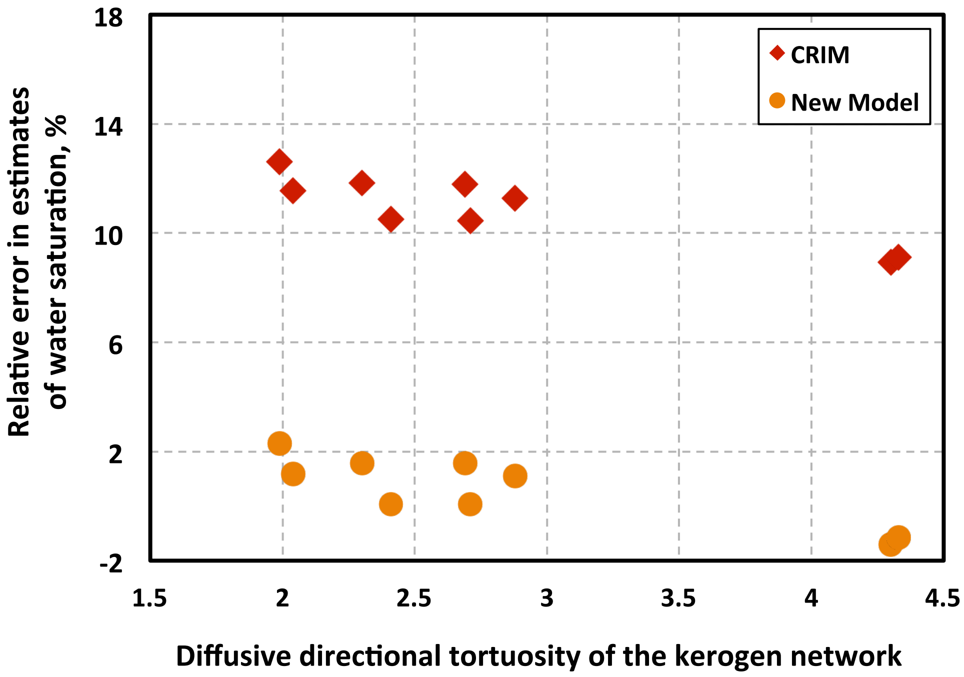

Figure 4.10: Synthetic digital organic-rich mudrock examples including conductive kerogen: the comparison of the water saturation estimates using the new model (orange dots) and the CRIM (red dots).

4.3.3.3 Impact of tortuosity of the pyrite network on estimates of water saturation

A third set of digital organic-rich mudrock samples is synthesized to investigate the impact of the diffusive directional tortuosity of the pyrite network on estimates of water saturation. The nine synthetic digital organic-rich mudrocks used to pursue this objective, all contain the same water saturation (i.e., 21%), the same volumetric concentrations of kerogen network (i.e., 30%) and pyrite (i.e., 2%). The same spatial distribution of water and kerogen networks is kept in all the synthetic examples which have the different diffusive directional tortuosity of the pyrite network. This is achieved by assigning different existence probability of connected pathways in different directions, while keeping the total volume of pyrite constant. It is assumed that kerogen is not conductive in these examples. **Figure 4.11** depicts the correlation between the tortuosity-dependent coefficient and the diffusive directional tortuosity of the pyrite network. The coefficients, e_w, b_w, and d_w, in our new model are calculated as 0.72, -1.877, and 1.05, respectively, using the cross-plot shown in **Figure 4.11**.

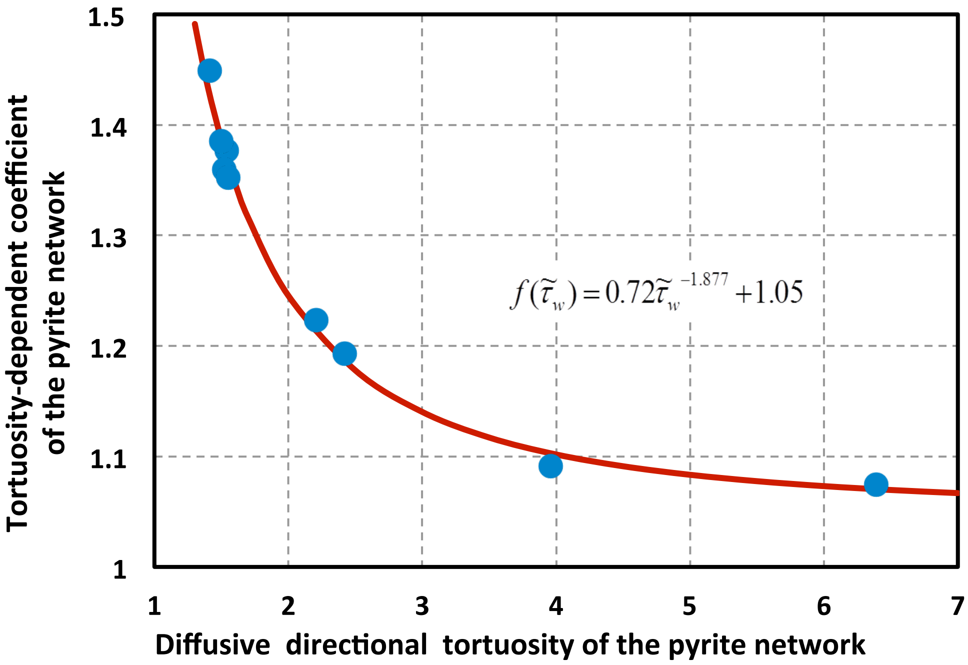

Figure 4.11: Synthetic digital organic-rich mudrock examples including pyrite and non-conductive kerogen: the correlation between the tortuosity-dependent coefficient and the diffusive directional tortuosity of the pyrite network for organic-rich rock samples.

After calculating the tortuosity-dependent coefficient of the pyrite network, the new joint model is applied to estimate water saturation. **Figure 4.12** shows the impact of the diffusive directional tortuosity of the pyrite network on the relative errors in estimates of water saturation by the new dielectric permittivity model and the CRIM. It is observed that with the increase of the diffusive directional tortuosity of the pyrite network, the relative errors in estimates of water saturation decrease from 27% to 4% overestimation by applying the CRIM. However, the relative errors from the new dielectric permittivity model are within the range of 3% overestimation to 3% underestimation, which are smaller than those obtained from the CRIM.

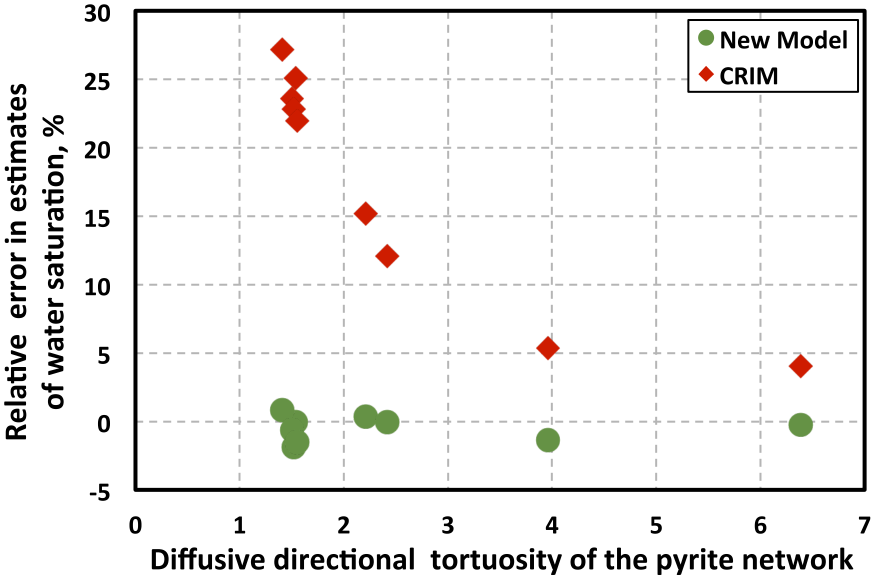

Figure 4.12: Synthetic digital organic-rich mudrock examples including pyrite and non-conductive kerogen: the comparison of the new model (green dots) and the CRIM (red dots) in estimates of water saturation with different diffusive directional tortuosity of the pyrite network.

4.4 Discussions

A new method is introduced that combines interpretation of electrical resistivity and dielectric permittivity of saturated rocks for assessment of water-filled porosity and hydrocarbon saturation based on 3D digital pore-scale images. Unlike the conventional interpretation techniques for dielectric permittivity and electrical resistivity measurements, the new joint model takes into account the anisotropic properties of the rock samples such as directional tortuosity of the conductive rock components. In the case of organic-rich mudrocks, in addition to incorporating the complex anisotropic water network, the new method takes into account the presence of kerogen and pyrite networks in interpretation of electrical resistivity and dielectric permittivity measurements for assessment of water-filled porosity and hydrocarbon saturation.

This chapter focuses on the pore-scale evaluation of electrical and dielectric properties of the rocks for better understanding the rock physics and for model development. The new joint model can be further applied for interpretation of core-scale and log-scale measurements in certain cases where upscaling is not a concern. The introduced method can directly be applied to well-log measurements for improved assessment of water saturation and water-filled porosity in homogeneous and anisotropic formations. For application of the introduced method to core-scale and log-scale measurements, numerical simulations will be performed in pore-scale 3D rock images at different rock types to estimate effective electrical resistivity and dielectric permittivity of each rock sample. Through the pore-scale numerical simulations, the method described in this chapter is used to find the correlation between tortuosity-dependent coefficient and tortuosity for each rock type in the formation. This correlation is then used as an input to our new model to analyze the dielectric and electric core-scale and log-scale measurements for assessment of water-filled porosity. In the case of heterogeneous and anisotropic formations, upscaling can be a challenge in application of the developed model to larger-scale measurements. Further upscaling of electrical and dielectric properties of the rocks is required for a reliable application of the developed method to core-scale and log-scale measurements.

The new joint model is most reliable for assessment of water-filled porosity in measurement frequency of 1 GHz and above, where dipolar polarization of water molecules is the dominant polarization mechanism in the rock. There will be uncertainties in the proposed evaluation method as well as other conventional methods for evaluation of dielectric permittivity (e.g., CRIM) in frequencies of less than 1GHz where other polarization mechanism such as interfacial polarization affects dielectric permittivity. At low frequency range, the impact of clay minerals and salt on dielectric measurements can be significant and needs to be taken into account.

Furthermore, the authors would like to emphasize that estimating an accurate matrix dielectric permittivity is essential for the success of the new model. Schmitt et al. (2011) showed that variation of +/- 1 unit in the matrix permittivity can results in about +/-2pu changes in water-filled porosity. Additionally, the accuracy of the introduced dielectric permittivity model depends on reliable estimation of total porosity, which can be estimated through joint interpretation of well logs such as nuclear logs.

Mud-filtrate invasion is another factor that needs to be taken into account, because of the relatively shallow radial length of investigation of the borehole dielectric tools (i.e., approximately 2-4 inches). In cases where mud-filtrate invasion is deep (deeper than the radial length of investigation of the tool) dielectric measurements will fully or partially detect properties of the invaded zone. In such cases, further corrections for mud-filtrate invasion are required through numerical simulations of well logs and the process of mud-filtrate invasion (Heidari et al., 2012).

4.5 Conclusions

This chapter documented a successful application of the new method of joint interpretation of the electrical resistivity and dialectical permittivity measurement in actual digital rock samples from a conventional sandstone formation and synthetic digital samples of unconventional organic-rich mudrocks. In the case of actual digital sandstone rocks, the new joint model provided reliable estimates of water-filled porosity with absolute relative errors of less than 10%. In this case, where pores structure was not complex and the only conductive component of the rock is formation water, the CRIM provided reasonable estimates of water-filled porosity, with only four out of twenty-one estimates beyond 10% relative error, with the largest absolute relative error of 30%. In the case of organic-rich mudrocks, however, the errors in estimates of water-filled porosity increased when the CRIM method was used. The absolute relative errors from six out of ten estimates for water-filled porosity in these samples were beyond 10%, with the maximum error of 40%. The results from the new method yielded absolute relative errors of less than 10% for both cases where kerogen was assumed conductive and non-conductive.

Furthermore, it was shown that in the presence of highly mature conductive kerogen, the spatial distribution of the kerogen network affects the resistivity measurements, but does not have a measureable impact on the dielectric permittivity measurements. The electrical resistivity increases by 13% with the increase of the diffusive directional tortuosity of the kerogen from 1.4 to 4.3, while the relative dielectric permittivity decreases by only 1%. Although conductive mature kerogen can significantly affect electrical resistivity measurements, the new joint model can still be applied successfully to organic-rich mudrocks for assessment of water-filled porosity and hydrocarbon saturation.

Finally, the impact of pyrite's spatial distribution on estimates of water saturation was discussed. It was shown that by taking into account the structure of pyrite network, the new model provided estimates of water saturation with relative errors of less than 3%. However, the CRIM method resulted in significantly larger (i.e., in the range of 4% to 27%) relative errors in estimates of water saturation. Thus, the new joint model is more reliable for assessment of water/hydrocarbon saturation in the presence of pyrite compared to conventional methods such as the CRIM. In general, the results are promising for a possible of joint interpretation of electrical resistivity and dielectric permittivity measurements in improving the assessment of water/hydrocarbon saturation.

CHAPTER V

IMPACT OF WATER SALINITY ON HIGH-FREQUENCY DIELECTRIC MEASUREMENTS IN BRINE-SATURATED ROCKS

Dielectric measurements have become attractive candidates for assessment of water-filled porosity and hydrocarbon saturation in formations such as carbonates and organic-rich mudrocks. Dielectric permittivity measurements are sensitive to water-filled porosity, especially in the high-frequency range (e.g., GHz frequency range), because of the higher dielectric permittivity of water compared to other rock matrix components. However, in the presence of saline water, water molecules lose their orientation freedom partially due to hydration with ions. Thus, the salinity of water affects dielectric measurements. The impacts of water salinity on the real part (i.e., dielectric constant) and the imaginary part (i.e., dielectric loss proportional to electrical conductivity) of dielectric permittivity are different and have not yet been quantitatively studied in high-frequency measurements. To accurately estimate water-filled porosity from dielectric permittivity measurements, the impact of water salinity on the measurements needs to be quantified at high frequencies.

This chapter has two objectives: (a) quantifying the impact of water salinity on dielectric permittivity measurements and (b) investigating the impact of water-salinity and water-filled porosity on the critical frequency (> 1 GHz) at which interfacial polarization is completely negligible.

The dielectric permittivity of brine is measured at frequencies ranging from 1 MHz to 3 GHz at ambient temperature and pressure, where water salinity varies from 0 Kppm to 160 Kppm. Then, dielectric permittivity of dry and brine-saturated rock samples is measured under the same frequency range. To investigate the impact of water salinity on dielectric permittivity of fully and partially brine-saturated rock samples, brine water is first injected to fully saturate the rock samples and then the dielectric permittivity of the samples at high frequencies (from 1 MHz to 3 GHz) is measured. Next, the centrifuge is used to partially saturate the rock samples, and the water salinity impact on the dielectric permittivity of brine-saturated rocks of with different water-filled porosity is compared.

This experimental method is applied on carbonate and sandstone samples with different pore structures to quantify the sensitivity of dielectric permittivity to water salinity, water-filled porosity, and frequency. The results confirm that there exists a critical frequency above which water salinity does not affect the dielectric constant, and this critical frequency increases as the water-filled porosity and water salinity increase. At high frequencies where the dielectric constant is independent of the frequency, there exists a critical water-filled porosity below which water salinity has negligible impact on the dielectric constant. However, when water-filled porosity is higher than this critical value, the dielectric constant slightly decreases by increasing water salinity. Furthermore, it is shown that at frequencies above this critical frequency, there is critical water salinity below which the dielectric loss increases as water salinity increases, while the dielectric loss decreases if water salinity exceeds this critical value. The quantitative results on the impact of water salinity on dielectric measurements can potentially improve interpretation of dielectric permittivity measurements for reliable assessment of water-filled porosity.

5.1 Introduction

Dielectric permittivity of porous media is the ability of materials to polarize and store electric charge. Complex relative dielectric permittivity of porous media is expressed as

$$\varepsilon^*(f) = \varepsilon'(f) + j\varepsilon''(f) = \varepsilon'(f) + j\frac{\sigma(f)}{2\pi\varepsilon_0 f}, \tag{5.1}$$

where ε_0 is the free space permittivity which is equal to $8.854\text{x}10^{-12}$ F/m, $\varepsilon'(f)$ is the real part which is usually referred to as the dielectric constant, $\varepsilon''(f)$ is the imaginary part of dielectric permittivity, which is referred to the dielectric loss and is a function of the conductivity of materials, σ, at the frequency f. Dielectric measurements are widely used in the petroleum (Gilmore et al., 1987; Hizem et al., 2008), agriculture (Lawrence, et al., 1998c; Nelson 1991) industry, and soil science (Shao, et al., 2003) for assessing water-filled porosity of formations, sensing the moisture in grain and seed, and investigating the impact of the soil salinity on the backscattering coefficient, respectively.

Dielectric permittivity of rock-fluid systems is controlled by three main dielectric mechanisms: (a) interfacial polarization, (b) molecular orientation polarization, and (c) electronic polarization. Interfacial polarization, which is attenuated at high-frequency external electric fields, is usually controlled by (a) rock texture, (b) cation exchange capacity (CEC) (Lasne et al., 2008; Sen, 1981a, 1981b, 1984; Wong et al., 1984), and (c) ions (e.g., the Maxwell-Wagner effect). In the presence of an external electric field, water molecules align their individual electric dipole along the external electric field, which results in molecule orientation polarization. Compared to water molecule orientation polarization, electric polarization is relatively weak and usually relates to rock matrix permittivity. Hizem et al., (2008) introduced a multi-frequency dielectric dispersion tool to measure the formation dielectric constant and conductivity at multiple frequencies from 20 MHz to 1 GHz. They used the 1 GHz results to estimate the formation water-filled porosity, believing that interfacial polarization at 1 GHz is negligible and water molecule polarization makes the most important contribution to dielectric permittivity.

Although, dielectric measurements are widely used in the petroleum industry, their interpretation still remains challenging, because the dielectric properties of porous media are sensitive to pore network structure, matrix dielectric permittivity, water-filled porosity, and cation exchange capacity. Several studies have been conducted on the interpretation of the dielectric property of a porous medium such as volumetric models (Calvert and Wells, 1977; Dahlberg and Ference, 1984; Linde et al., 2006; Wharton et al., 1980), Stroud-Milton-De (SMD) (Stroud et al., 1986), and the Complex Refractive Index Model (CRIM) (Feng and Sen, 1985; Pirrone et al., 2011). To better estimate the water-filled porosity of rocks through dielectric measurements, Seleznev et al. (2006) developed the dispersion dielectric model by incorporating textural characteristics (e.g., the aspect ratio of grains and pores). Chapter III of dissertation proposes a new dielectric permittivity model that incorporates the spatial distribution of pore network structure.

Furthermore, the salinity of brine can influence dielectric measurements, and needs to be taken into account when interpreting these measurements. Rankin et al. (1985) discussed the effect of clay and salinity on the dielectric properties of sand-clay mixtures and consolidated sandstone, showing that fluid content rather than salinity is a determining factor to the dielectric constant above 0.4 GHz, while increment of salinity results in the reduction of the dielectric constant due to the tendency of increased crystallization in the presence of salt. Teheran et al. (1990) conducted an extensive set of measurements of brine-saturated rock samples in frequencies between 10 MHz to 1.3 GHz and found that salinity impacts the dielectric loss of different rock samples in that frequency range. Wu et al. (2015) measured the dielectric properties of saline soil and improved the conventional dielectric models by taking into account the salinity in the C-band frequency range (i.e., 4-8 GHz). Shao et al. (2003) showed that soil moisture and salinity affect the dielectric loss, and that the salinity of soil has little influence on the dielectric constant. However, the aforementioned publications did not investigate the impact of water-filled porosity on the sensitivity of dielectric permittivity to water salinity. Furthermore, they did not quantify the frequency at which interfacial polarization is negligible when conducting dielectric measurements. In this chapter, we conducted dielectric measurements in three rock types saturated with brines of different salinity to quantify the impact of salinity on dielectric properties of rocks with different water-filled porosity, and then further investigated whether interfacial polarization is negligible at high frequency (> 1 GHz) for saturated rocks of different water salinity and water-filled porosity.

The upcoming sections describe the experimental design for dielectric measurements of brine-saturated rocks and the results. The impact of salinity is first quantified on the dielectric properties of brine, as well as on the dielectric constant and dielectric loss of three brine-saturated rock samples. The critical frequency of brine-saturated rock samples is quantified above which interfacial polarization is minimized at different values of water salinity and water-filled porosity.

5.2 Method

This section describes the laboratory experiment setup and procedures. The dielectric permittivity laboratory measurements were conducted using the end-loaded transmission line method (Burdette, 1980 and Stuchly, 1980). This method, which applies an inversion algorithm for the coaxial transmission line against the surface of the rock, is rapid and convenient, and can also measure the drill cutting or past form (Leung and Steiger, 1992). This dissertation research used the dielectric high temperature probe kit HP 85070E with the HP Agilent impedance analyzer E4991A. The general regularly distributed information in binary form (GPIB) connection was used to connect the E4991A to the computer following the IEEE488 standard. Both the impedance analyzer and the dielectric probe were calibrated before the measurements. The typical permittivity measurement accuracy is about ±5%, whereas the loss tangent is about ±0.05%.

The experimental procedures, including rock sample preparation, are described in detail in the following subsections, which state the procedures for the preparation of rock samples and brine, and then explain the method applied for fully and partially saturating the rock samples. Finally, the subsections introduce the NMR measurement technique which is used to quantify water-filled porosity, as well as the experimental procedures for dielectric measurements.

5.2.1 Preparation of rock samples and brine

Three different types of dry and clean rock samples purchased from Kocurek Industries INC. were selected for water salinity investigation: Berea sandstone A101, and Indiana limestone B101A and B101C. All samples were cut as cylindrical core plugs of 1-inch diameter and 0.5-inch length. Both the top and bottom faces of the plugs were carefully smoothed to eliminate air gaps between the dielectric sensor and rock samples. These rock samples are initially put in the oven at 150˚C for 12 hours to ensure that they were completely dry. **Figures 5.1(a)**, **5.1(b)**, and **5.1(c)** show the three rocks used in the experiments. **Table 5.1** lists the petrophysical properties of these rock samples. The Berea sandstone, A101, and Indiana limestone, B101C, have similar porosity, of approximately 18%. The porosity of Indiana limestone, B101A, is 15%.

(a) (b) (c)

Figure 5.1: The rock samples prepared for dielectric measurements: (a) Berea sandstone, A101, (b) Indiana limestone, B101A, and (c) Indiana limestone, B101C.

As for the brine preparation, controlled amounts of sodium chloride (NaCl) were added to distilled water, and an ultrasonic system and a stir bar were used to dissolve the salt. Brine samples were prepared with salinities of 1, 10, 20, 40, 80, 100, 120, and 160 Kppm.

Table 5.1: Petrophysical properties of the Indiana limestone, B101A, B101C and Berea sandstone, A101.

Rock Samples	**Formation**	**Brine permeability (MD)**	**Porosity (%)**	**Grain density (g/cc)**
Indiana limestone B101A	Bedford	2-4	15	2.686
Indiana limestone B101C	Bedford	70	18	2.685
Berea sandstone A101	Kipton	60-100	18	2.635

5.2.2 Preparation of fully and partially brine-saturated rock samples

A core flood system and vacuum pressure pump were used to fully saturate the rock samples with brine. To ensure full saturation of the rock samples, the core flood experiments were first conducted at low flow rate until 10 times the pore volumes of brine passed through the rock samples. After core flooding the rock samples, the samples were saturated in brine, and the vacuum pressure pump system was kept running until there was no change in the weight of the brine-saturated rock sample to guarantee 100% brine saturation. Next, centrifuge was used to remove certain amounts of water and partially saturate the rock samples. To achieve different partial saturation conditions, the rock samples were spun in the centrifuge at different speeds and waiting times. Both sides of the rock samples were spun at the same speed and waiting time to uniform saturation. To change injected brine salinity for the same rock sample, the core flood system was used again to flush the sample using different brine salinity, and the vacuum pressure pump system was continually used to ensure that the samples achieved 100% brine saturation. **Figure 5.2** shows the core flood system used for saturating the rock samples. **Figure 5.3** shows the procedure for preparing the fully and partially brine-saturated rock samples. The water-filled porosity and air-filled porosity in the rock samples are estimated via

$$\phi_w = V_w / V_R \tag{5.2}$$

and

$$\phi_{air} = V_a / V_R, \tag{5.3}$$

where V_w, V_a, and V_R are volumes of water, air, and rock, respectively. The volume of water in the rock samples was obtained using Nuclear Magnetic Resonance (NMR) measurement.

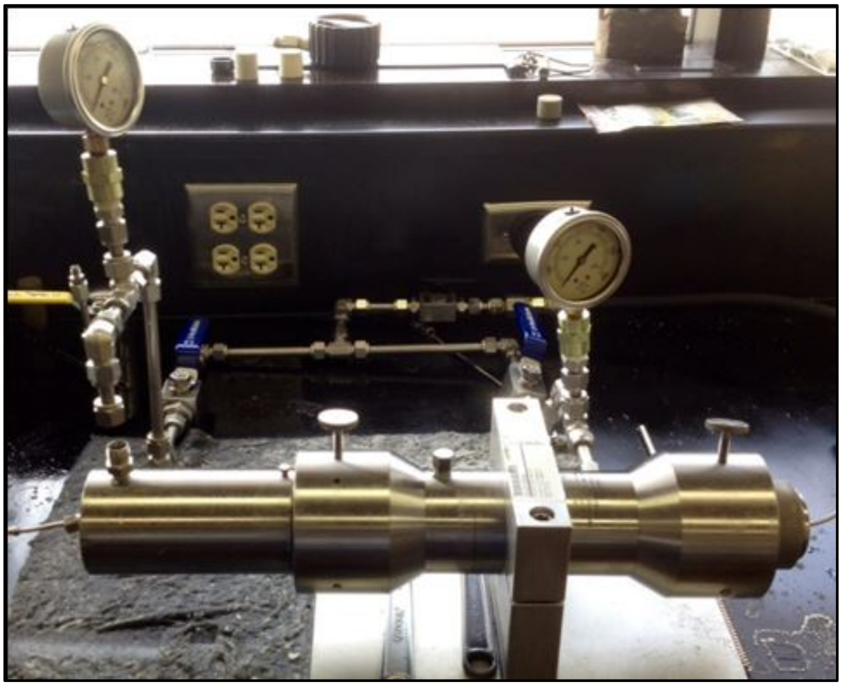

Figure 5.2: Core flood system for fully and partially saturating the rock samples.

5.2.3 Assessment of water-filled porosity using NMR measurements

Nuclear Magnetic Resonance (NMR) measurements were used to quantify water-filled porosity of the brine-saturated rock samples. NMR laboratory measurements were conducted using a 2 MHz NMR benchtop spectrometer (e.g., GeoSpec2 Core Analyzer) and the T_2 relaxation time (i.e., spin-spin or transverse relaxation time) was measured by the Carr-Purcell-Meiboom-Gill (CPMG) pulse sequence. The initial measurement parameters assumed for the NMR measurements included: (a) 200 μsec of CPMG inter-echo spacing time (TE); (b) 256 scans; (c) signal-to-noise ratio of 200.

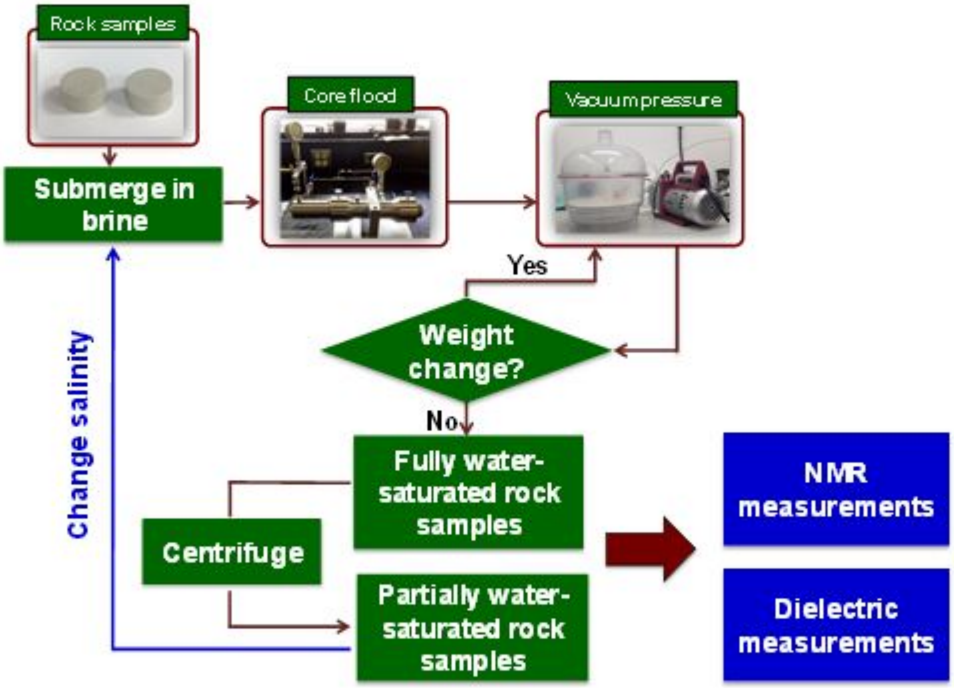

Figure 5.3: The procedure for preparation of the fully and partially brine-saturated rock samples.

5.2.4 Dielectric measurements in the brine-saturated rock samples

An open-ended transmission line method was used to measure dielectric permittivity of the cylindrical brine-saturated rock plugs. **Figure 5.4** shows the dielectric high temperature probe kit HP 85070E used with the HP Agilent impedance analyzer E4991A. The general regularly distributed information in binary form (GRIB) connection was used to connect the E4991A to the computer following the IEEE488 standard. Both the impedance analyzer and the dielectric probe were calibrated before the measurements. The dielectric permittivity measurement accuracy was about ±5%, whereas the loss tangent was about ±0.05%. **Table 5.2** lists the required environment and accuracy for the measurements. The dielectric measurements were performed in the frequency range of 1 MHz to 3 GHz at temperature of 70ºF and pressure of 14.7 psi and repeated four times for both the faces (top and bottom) of each rock sample to minimize the experimental error.

Figure 5.4: High-temperature probe kit.

Table 5.2: Characteristic parameters and accuracy of the dielectric measurements.

Parameters	**Value**
Temperature range	-40 to 392ºF
Frequency range	1MHz to 3GHz
Diameter	> 20mm
Thickness	$> \frac{20}{\sqrt{\lvert\varepsilon^{*}\rvert}}$ mm
Grain size	< 0.3mm
Maximum recommendation ε'	< 100
Minimum recommendation $\varepsilon'/\varepsilon''$	> 0.05
Accuracy of the measurements	$\varepsilon'' \approx \varepsilon' \pm 0.05\lvert\varepsilon'\rvert$
	$\varepsilon''/\varepsilon' \approx \varepsilon''/\varepsilon' \pm 0.05\lvert\varepsilon''/\varepsilon'\rvert$

5.2.5 Workflow

Figure 5.5 summarizes the workflow of the laboratory experimental procedures to investigate the impact of salinity and water-filled porosity on the dielectric permittivity of the brine-saturated rocks. Clean carbonate rock samples were prepared and put into an oven for drying. Meanwhile, brine with different salinity was prepared to further saturate the rock samples through the core flood and vacuum pressure system. The measured samples included the brine itself, and dry and saturated rocks. At last, NMR and dielectric permittivity were conducted to investigate the corresponding properties.

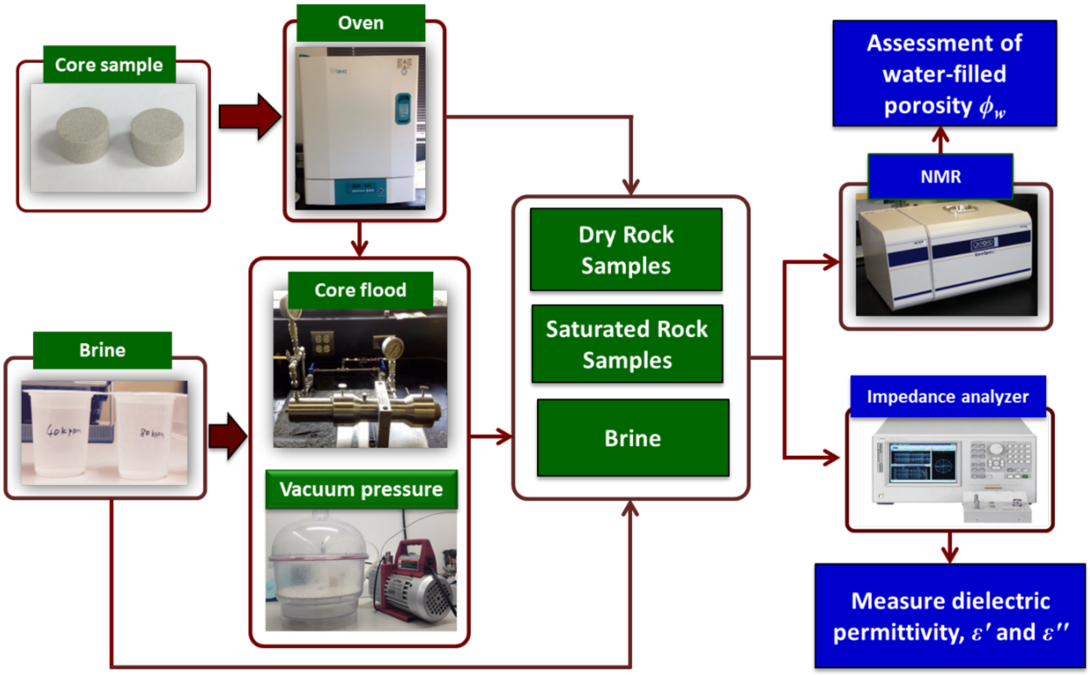

Figure 5.5: The workflow for the laboratory experimental procedures to investigate the impact of salinity and water-filled porosity on the dielectric permittivity of the brine saturated rocks.

5.3 Results

This section lists and discusses the results. It first describes the impact of water salinity on the dielectric permittivity of brine, and then quantifies the impact of water-filled porosity and water salinity on the dielectric permittivity of brine-saturated rocks. Finally, it quantifies the impact of water salinity on the critical frequency of the dielectric measurements in the brine-saturated rocks.

5.3.1 Impact of salinity on the dielectric permittivity of brine

Figure 5.6 shows the dielectric constant and dielectric loss of brine at variable water salinity ranging from 0 Kppm to 160 Kppm, at room temperature and ambient pressure. The measurements were performed in the frequency range of 1 MHz to 3 GHz. These results confirmed that with the increase of water salinity, the dielectric constant of the brine decreases and the dielectric loss increases. At the same water salinity, both the dielectric constant and the dielectric loss decrease as the measurement frequency increases. In the presence of sodium chloride, water molecules are hydrated easily. The water molecules around the ions orient themselves along the ions and lose their orientation polarization towards the external electric field direction. Furthermore, salt ions displace water molecules and results in kinetic depolarization (Lane and Saxton, 1952). Thus, an increase of salinity leads to a decrease of the dielectric constant. Alternatively, increased salinity leads to an increase of the number of ions so that the electrical conductivity of the brine increases. Chandra and Bagchi (2000) also pointed out that the reduced electric force of relaxation leads to higher ion mobility and enhancement of the conductivity at low frequencies. On the other hand, at higher frequency, the retarding effect vanishes and the central ions become motionless, resulting in decreased ionic conductivity (Chandra and Bagchi, 2000; Falkenhagen et al., 1931). At higher frequency, the decrease in ion mobility leads to more hydrated water molecules, thus decreasing the dielectric constant

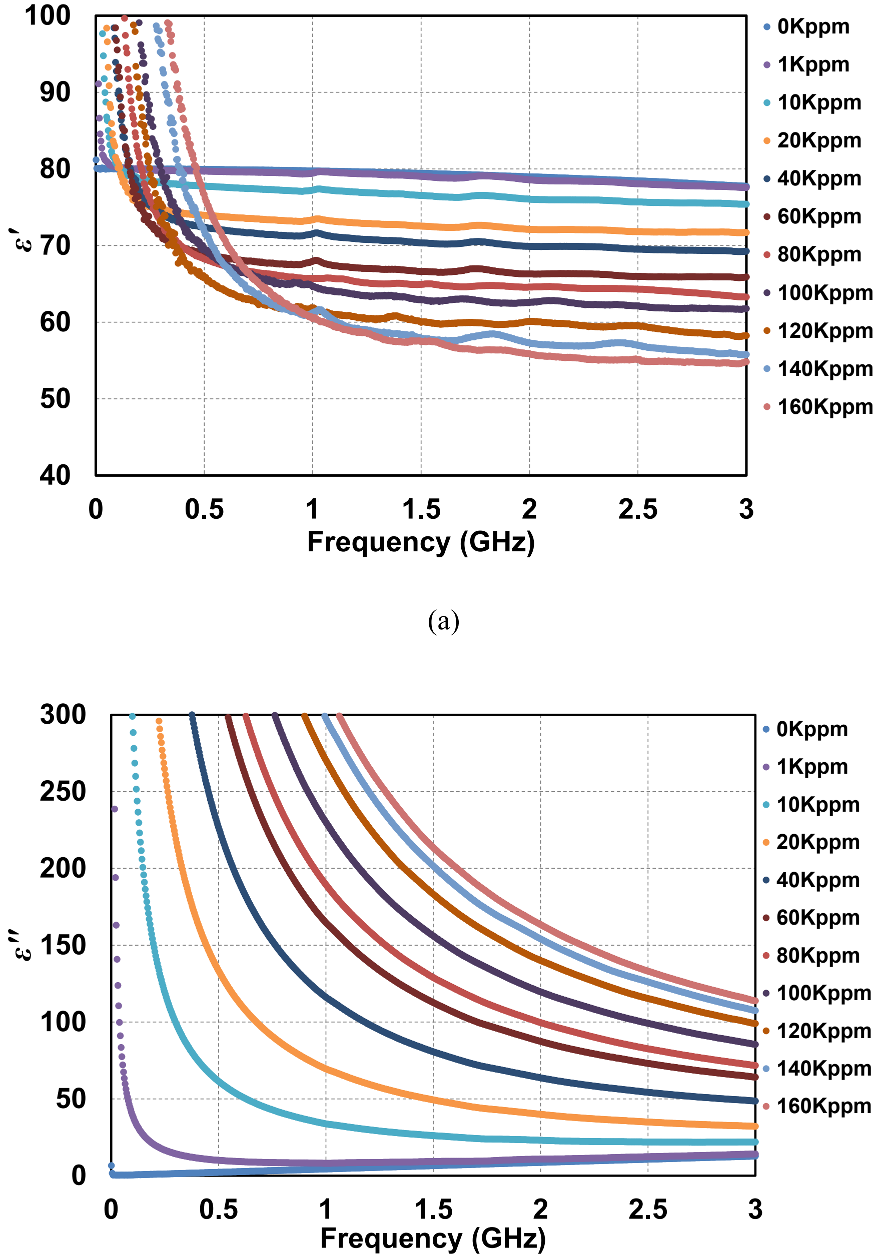

(a)

(b)

Figure 5.6: Frequency-dependent dielectric constant and dielectric loss of brine with salinity ranging from 0 Kppm to 160 Kppm.

5.3.2 Impact of salinity on the dielectric permittivity of brine-saturated rock samples

In this subsection, we first exhibit the NMR measurement results to evaluate water-filled porosity and water-filled pore size distribution for brine-saturated rock samples. We then show the results from the dielectric measurements on fully and partially brine-saturated rock samples when water salinity is kept constant at 40 Kppm and when the range varies 40-160 Kppm.

5.3.2.1 Evaluation of water-filled porosity and pore size distribution for brine-saturated rock samples

After preparing fully and partially brine-saturated rock samples, NMR measurements were conducted to evaluate the water-filled porosity and water-filled pore size distribution. **Figure 5.7** shows the NMR T_2 distribution of the fully and partially brine-saturated Indiana limestone, B101C, samples saturated with water salinity, ranging from 40 Kppm to 160 Kppm. The T_2 relaxation peaks are located at around 260 msec, 140 msec, 50 msec, and 40 msec, for 18%, 13.8%, 9.8%, and 7.8% water-filled porosity, respectively. The same T_2 distribution at different water salinity values confirmed that brine distribution in the pore network is almost the same for saturated rocks of the same water-filled porosity. The uncertainty of accumulative water-filled porosity is within 5% relative error for different levels of salinity. Similarly, NMR measurements confirmed the consistent water distribution in the cases of Indiana limestone sample, B101A, and Berea sandstone sample, A101.

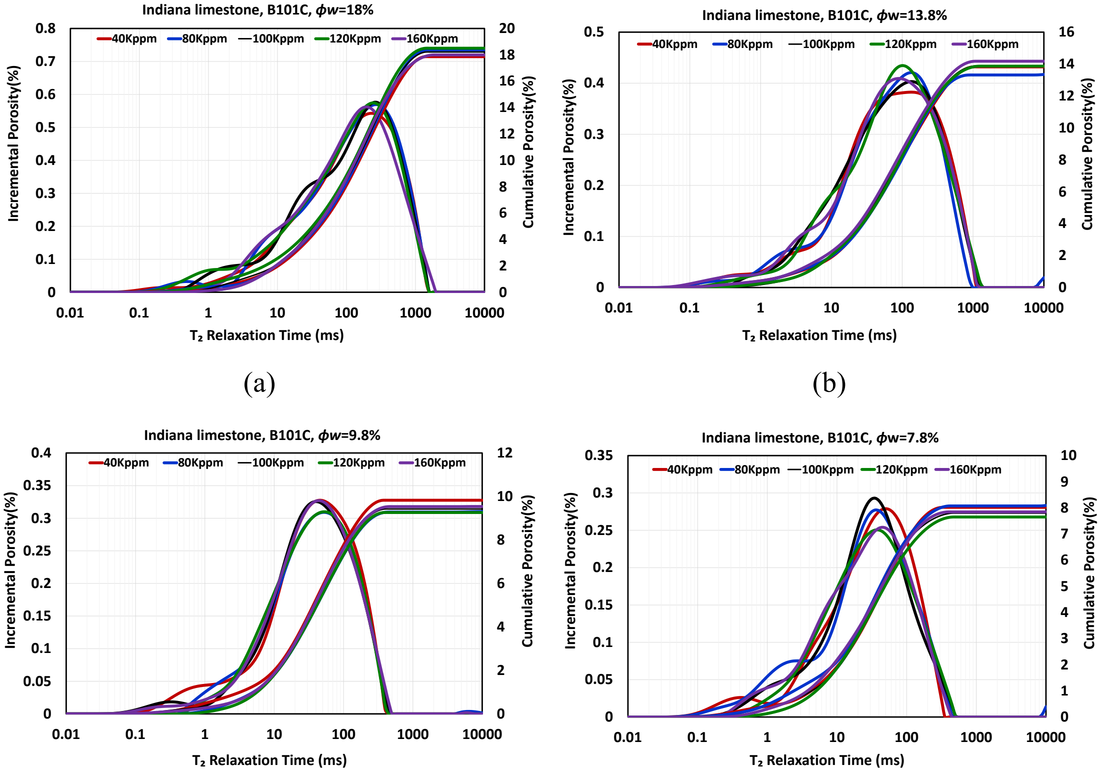

(a)

(b)

(c)

(d)

Figure 5.7: NMR T_2 distribution, incremental porosity, and accumulative porosity of Indiana limestone, B10C, rock samples with water-filled porosity of (a) 18%, (b) 13.8%, (c) 9.8%, and (d) 7.8%. Red, blue, black, green, and purple curves in each plot represent the NMR T_2 distribution for 40Kppm, 80Kppm, 100Kppm, 120Kppm, and 160Kppm water salinity, respectively.

5.3.2.2 Impact of water-filled porosity on dielectric measurements at constant salt concentration

Figures 5.8(a) and **5.8(b)** show the real and imaginary parts of the dielectric permittivity of the Indiana limestone sample, B101C, at 40 Kppm water salinity for water-filled porosity ranging from 0% to 18%. The measurements were performed in the frequency range of 1 MHz to 3 GHz. For dry samples (i.e., 0% water-filled porosity), it was observed that a constant dielectric permittivity of approximately 7.0 exists the entire frequency range. The only contribution to the dielectric constant in this case is the electronic polarization. Meanwhile, the dielectric loss of this dry sample is close to 0.

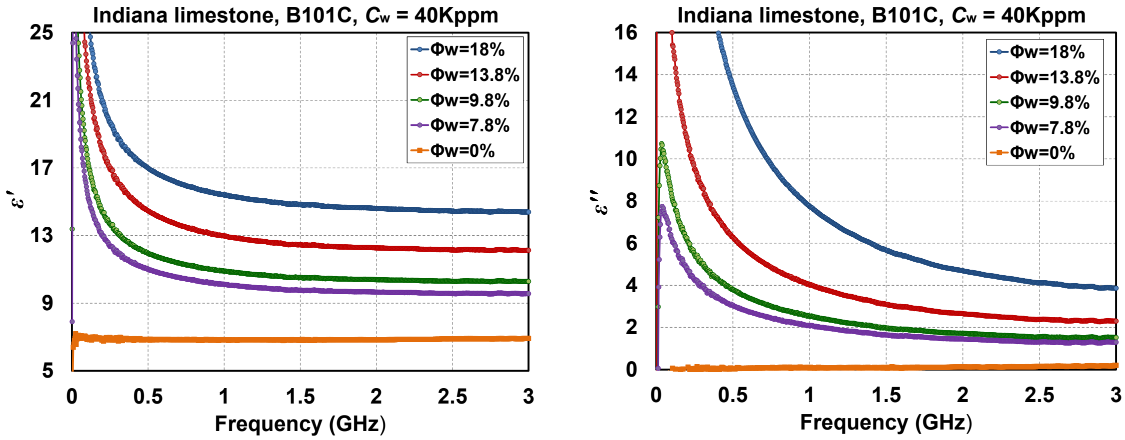

(a) (b)

Figure 5.8: Frequency-dependent (a) dielectric constant and (b) dielectric loss of Indiana limestone, B101C, at 40Kppm water salinity for water-filled porosity range of 0% to 18%. Blue, red, green, purple, and orange lines represent 18%, 13.8%, 9.8%, 7.8% and 0% water-filled porosity, respectively.

In the case of brine-saturated rock samples, as the water-filled porosity increases, both the dielectric constant and dielectric loss of these samples increase. At frequencies higher than 1.7 GHz, the dielectric constant is frequency-independent, and it tends to be a constant value. At frequencies of less than 1 GHz, the dielectric loss is more sensitive to the variation of water-filled porosity. However, at frequencies of higher than 1 GHz, the dielectric loss of the brine-saturated rock samples is not affected significantly by water-filled porosity. At a 0.5 GHz frequency and 40 Kppm water salinity, the dielectric loss of the brine-saturated Indiana limestone sample B101C, changes from 0 to 13 when the water-filled porosity varies from 0% to 18%. The same variation in water-filled porosity leads to a measureable increase of dielectric loss from 0 to 4 at frequency of 3 GHz.

Dielectric permittivity measurements were carried out on all three rock samples. The results for the other two rock samples, Berea sandstone sample A101 and Indianan limestone sample B101A, also confirmed the aforementioned observations. At 40 Kppm water salinity, in the case of the Berea sandstone sample A101, changing the water-filled porosity from 0% to 18% leads to variation of the dielectric loss from 0 to 6.3 at frequency of 0.5GHz and from 0 to 2.5 at 3 GHz. Likewise, in the case of the Indiana limestone, B101A, the dielectric loss varied from 0 to 4.9 at 0.5 GHz and 0 to 1.9 at 3 GHz due to the variation in water-filled porosity from 0% to 15%.

5.3.2.3 Impact of water salinity on dielectric measurements

Figures 5.9 and **5.10** show the frequency-dependent dielectric constant and dielectric loss of Indiana limestone B101C, at variable water-filled porosity (i.e., 18%, 13.8%, 9.8%, and 7.8%) for water salinity ranging from 40 Kppm to 160 Kppm. The measurements were performed in the frequency range of 1MHz to 3GHz. The impact of water salinity on dielectric dispersion is more significant at lower frequency measurements rather than at higher. **Figures 5.11** and **5.12** show dielectric constant and loss of brine-saturated samples with variable water-filled porosity at frequency of 3 GHz for water salinity ranging from 40 Kppm to 160 Kppm. **Figure 5.11(a)** shows that at 3 GHz, water salinity has only a small influence on the dielectric constant of Indiana limestone, B101C. When the water-filled porosity is less than 13.8%, the impact of water salinity on the dielectric constant is negligible. With the increase in water-filled porosity, water molecule polarization becomes dominant, and, consequently, leads to a decrease of the dielectric constant.

It was observed that at 18% water-filled porosity and 3GHz frequency, the dielectric constant of the rock samples decreases from 14.4 to 13.1 with increase of the water salinity from 40 Kppm to 160 Kppm. This phenomenon can also be explained with the fact that for smaller water-filled porosity, the bound water saturation is high, which makes ionic hydration of the water molecule difficult. However, large water-filled porosity has more moveable free water in the pore structure, which is easily hydrated by the salt ions, causing some water molecules to partially lose their orientation freedom.

From **Figures 5.11(b)** and **5.11(c)**, it was also observed that the critical water-filled porosity (i.e., the water-filled porosity above which water salinity has a measurable impact on the dielectric constant of the brine-saturated rocks) of Berea sandstone A101, and Indiana limestone, B101A are close to 15.5% and 15%, respectively.

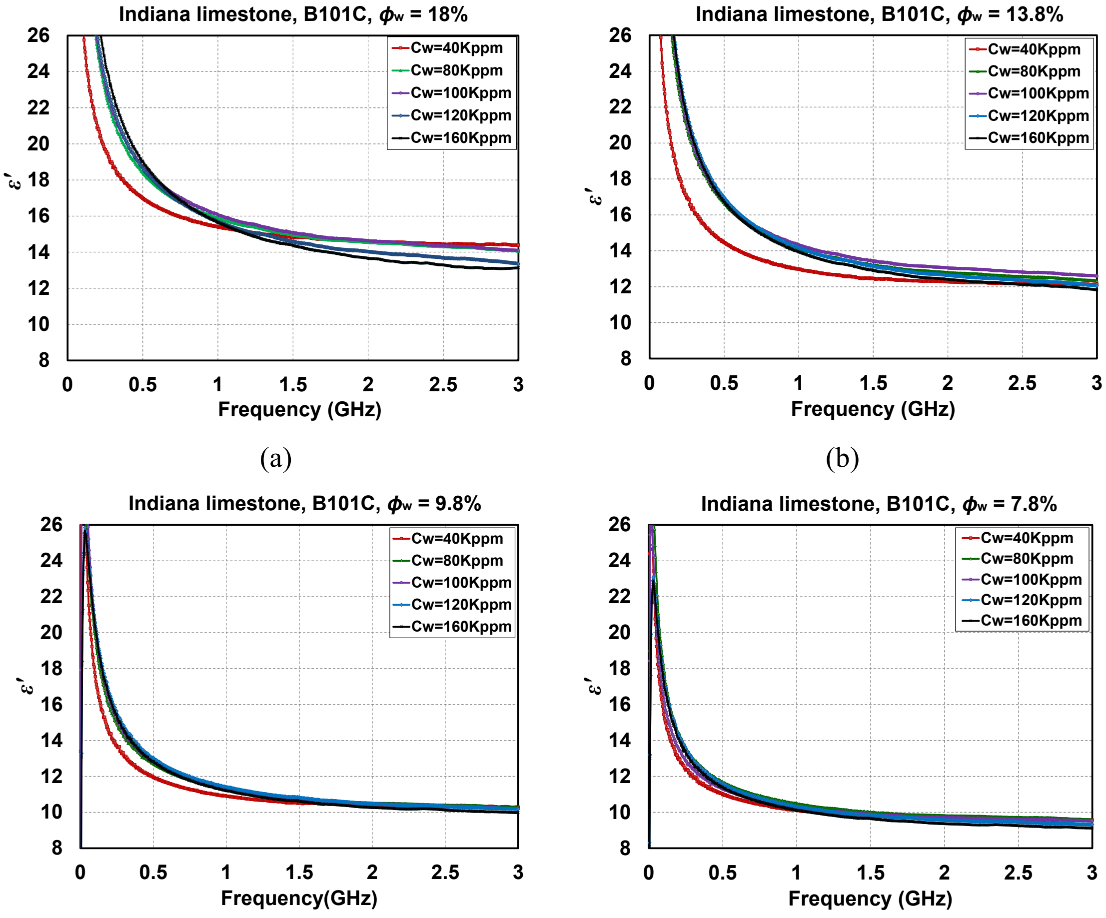

(a) (b)

(c) (d)

Figure 5.9: Indiana Limestone B101C: Frequency-dependent dielectric constant of brine-saturated rock samples with water-filled porosity of (a) 18%, (b) 13.8%, (c) 9.8%, and (d) 7.8 at water salinity of 40Kppm to 160Kppm. The measurement frequency is ranging from 1MHz to 3GHz. Red, green, purple, blue, and black lines represent water salinity of 40 Kppm, 80 Kppm, 100 Kppm, 120 Kppm, and 160 Kppm, respectively.

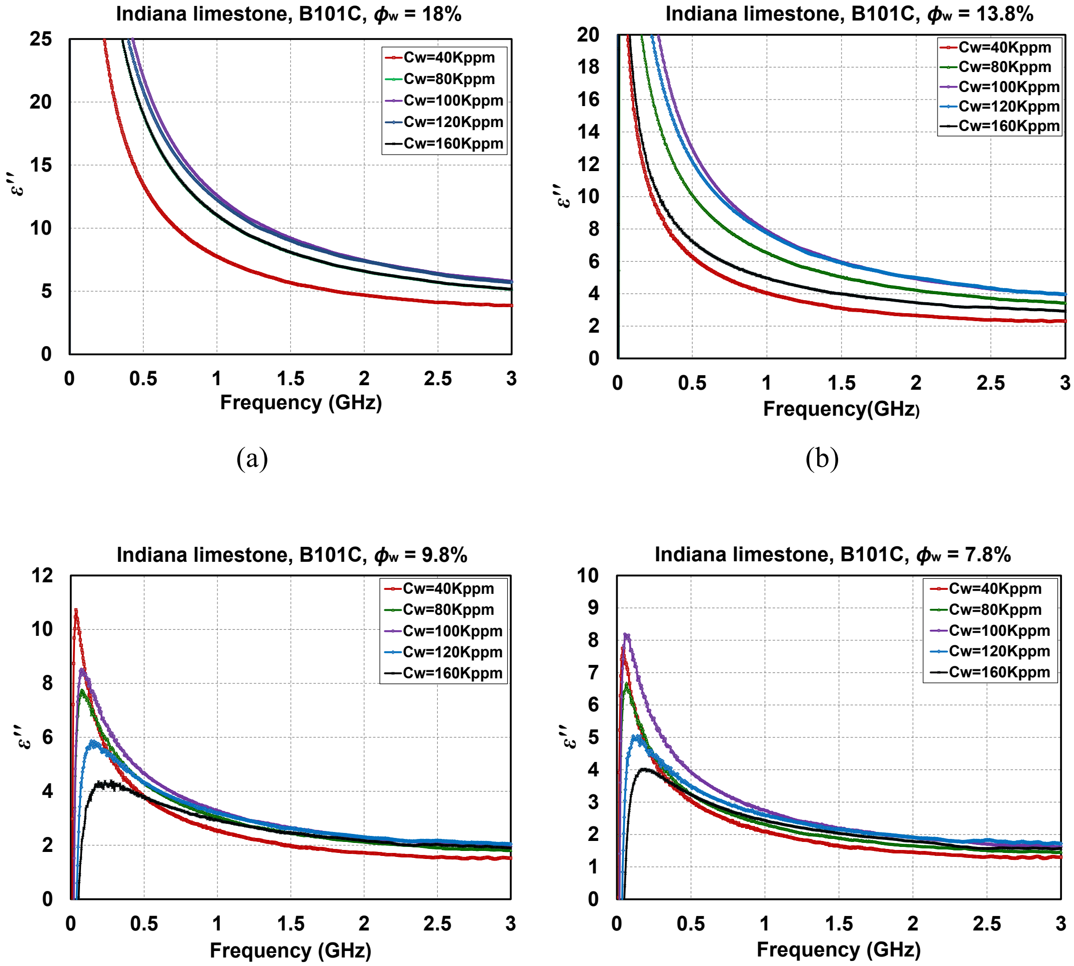

(a) (b)

(c) (d)

Figure 5.10: Indiana Limestone B101C: Frequency-dependent dielectric loss of brine-saturated rock samples with water-filled porosity of (a) 18%, (b) 13.8%, (c) 9.8%, and (d) 7.8% at water salinity of 40Kppm to 160Kppm. The measurement frequency is ranging from 1MHz to 3GHz. Red, green, purple, blue, and black lines represent 40 Kppm, 80 Kppm, 100 Kppm, 120 Kppm, and 160 Kppm water salinity, respectively.

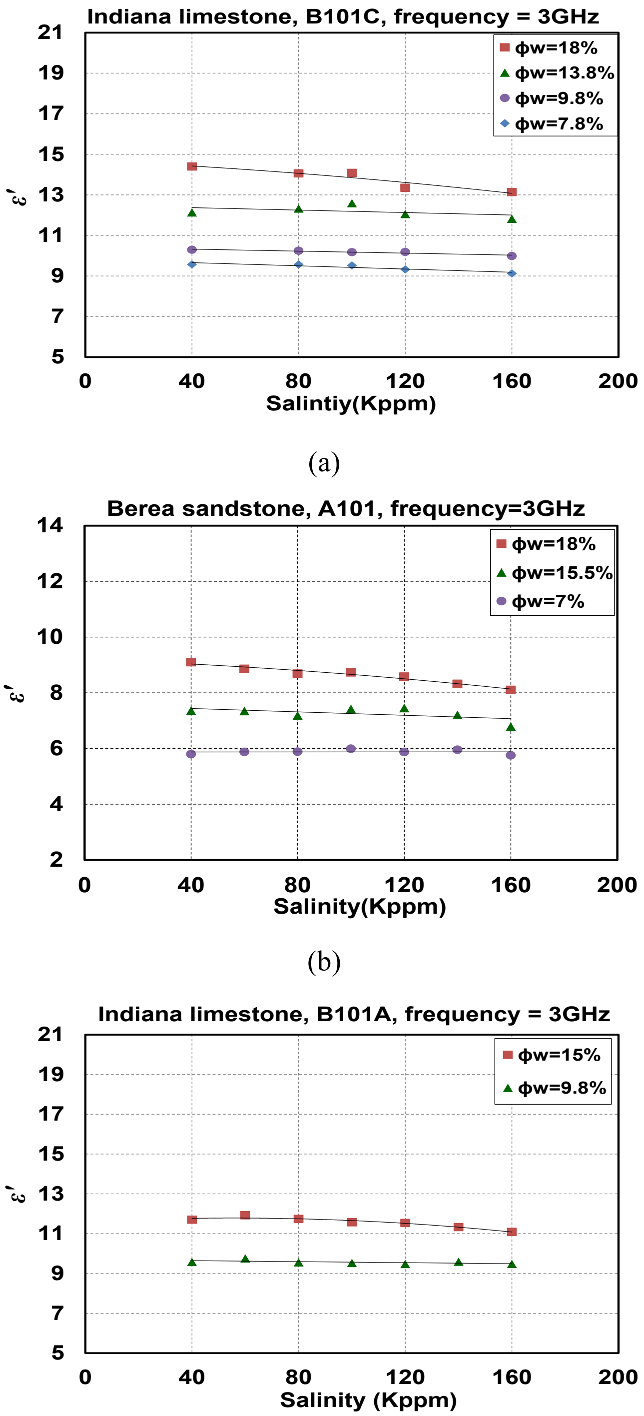

(a)

(b)

(c)

Figure 5.11: Dielectric constant measurements for (a) Indiana limestone, B101C, (b) Berea sandstone, A101, and (c) Indiana limestone, B101A, at 3 GHz. Water salinity and water-filled porosity are ranging from 40 Kppm to 160 Kppm and from 7% to 18%, respectively.

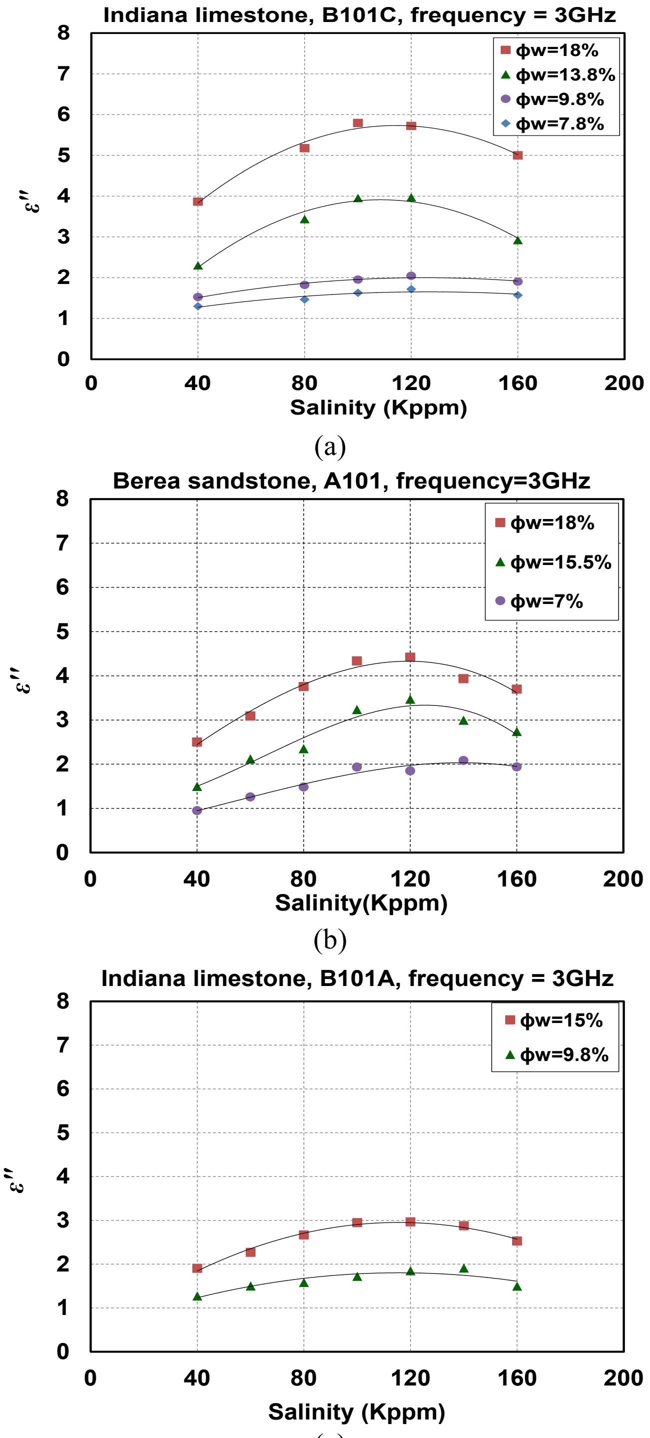

(a)

(b)

(c)

Figure 5.12: Dielectric loss measurements for (a) Indiana limestone, B101C, (b) Berea sandstone, A101, and (c) Indiana limestone, B101A, at 3 GHz. Water salinity and water-filled porosity are ranging from 40 Kppm to 160 Kppm and from 7% to 18%, respectively.

Table 5.3 lists the percentage change in the dielectric constant corresponding to the change of salinity from 40 Kppm to 160 Kppm at different water-filled porosity. In the case of Indiana limestone rock sample, B101C, we used the conventional CRIM to estimate water-filled porosity. For the rock sample of 18% water-filled porosity, a change of salinity from 40 Kppm to 160 Kppm, can result in a decrease of the dielectric constant by around 9%, which can result in a 14% difference in the estimation of water-filled porosity from the CRIM. In the case of 7.8% water-filled rock sample, the estimated water-filled porosity stays almost the same even though salinity changes from 40 Kppm to 160 Kppm. It was also observed that the change in dielectric constant is less than 5% for the change of salinity when the water-filled porosity was less than 15% for all three rock samples. The results confirmed that the salinity impact has to be taken into account in the interpretation of dielectric measurements in the cases with high water-filled porosity.

Figure 5.12 shows the measured dielectric loss in all three brine-saturated rock samples, including (a) Indiana limestone B101C, (b) Berea sandstone A101, and (c) Indiana limestone B101A, at 3 GHz. Water salinity and water-filled porosity ranged from 40 Kppm to 160 Kppm and from 7% to 18%, respectively. The results indicate that the dielectric loss of the brine-saturated rocks increases with an increase of water salinity; as more salt dissolves in the water, the electrical conductivity increases. The sensitivity of dielectric loss to salt concentration is more significant in cases of high water-filled porosity. However, when water salinity is greater than 120 Kppm, it is observed that the dielectric constant of the rock samples starts to decrease. This is explained by the start of salt precipitation at this critical water salinity (i.e., 120 Kppm) that decreases ionic conductivity. All of the described measurements were conducted at room temperature and pressure. Thus, the critical water salinity might be higher under reservoir conditions. **Figures 5.12(a)** and **5.12(b)** show that at 3 GHz frequency and 18% water-filled porosity, the variation of water salinity from 40 Kppm to 120 Kppm leads to an increase of the dielectric loss of the Indiana limestone, B101C, from 4 to 5.8, and the increase of the dielectric loss of Berea sandstone, A101, from 2.5 to 4.3, respectively. These results further underscore that the dielectric loss of the brine-saturated rocks is also influenced by the pore network structure.

Table 5.3: Percentage change in dielectric constant of brine-saturated rocks when salinity changes from 40Kppm to 160Kppm at different water-filled porosity, 18%, 15.5%, 15%, 13.8%, 9.8%, 7.8%, 7%.

Rock Samples	ϕ_w **(18%)**	ϕ_w **(15.5%)**	ϕ_w **(15%)**	ϕ_w **(13.8%)**	ϕ_w **(9.8%)**	ϕ_w **(7.8%)**	ϕ_w **(7%)**
Indiana Limestone, B101C	9%	–	–	2.6%	2.8%	3%	–
Berea Sandstone, A101	11%	7.8%	–	–	–	–	0.7%
Indiana limestone, B101A	–	–	5.1%	–	1%	–	–

5.3.3 Impact of water salinity on the critical frequency of dielectric permittivity measurements

The results presented in **Figures 5.9(a)**, **5.9(b)**, **5.9(c)**, and **5.9(d)** indicate that for each water-filled porosity and water salinity level, there exists a critical frequency above which the dielectric constant tends to be a stable value (i.e., interfacial polarization is minimized). To estimate this critical frequency, we calculated the derivative of the dielectric constant to frequency. The frequency at which the calculated derivative becomes less than 0.5×10^9 (1/GHz), is defined as the critical frequency. The assumed criterion of -0.5×10^9 (1/GHz) means that dielectric constant will decrease by 0.5 if the frequency increases by 1 GHz. **Tables 5.4** and **5.5** list the calculated critical frequencies of Indiana limestone, B101C, and Berea sandstone, A101, at different values of water salinity and water-filled porosity. The results in all three rock samples showed that 1 GHz frequency is not high enough to safely assume that the interfacial polarization is negligible, especially when dealing with formations with high water-filled porosity.

Figures 5.13(a) and **5.13(b)** illustrate the impact of water salinity and water-filled porosity on the critical frequency of Indiana limestone B101C, and Berea sandstone A101, respectively. It was observed that the critical frequency increases with the increase of both water salinity and water-filled porosity. In the case of 40 Kppm water salinity, the critical frequency increases from 1.36 to 1.7 GHz, when the water-filled porosity of this limestone increases from 7.8% to 18%. In the case of 160 Kppm water salinity, the critical frequency increases from 1.7 to 4.1 GHz. In the case of 7.8% water-filled porosity, the critical frequency increases from 1.36 to 1.7 GHz, when the water salinity increases from 40 Kppm to 160 Kppm, and in the case of 18% water-filled porosity, the critical frequency increases from 1.7 to 4.1 GHz. Although most of the field measurements are extrapolated to 1GHz, the results showed that, depending on the pore network structure, water-filled porosity and water salinity, 1GHz might not be high enough for a reliable assessment of water-filled porosity.

Table 5.4: Critical frequency of brine-saturated rock samples at different water-filled porosity (18%, 13.8%, 9.8%, and 7.8%) and water salinity (40Kppm, 80Kppm, 120Kppm, and 160Kppm) for Indiana limestone, B101C.

ϕ_w (%)	40 Kppm	80 Kppm	100 Kppm	120 Kppm	160 Kppm
18	1.71	2.24	2.56	3.57	4.07
13.8	1.59	1.94	2.18	2.58	2.58
9.8	1.42	1.70	1.77	1.85	1.85
7.8	1.36	1.59	1.53	1.70	1.70

Table 5.5: Critical frequency of brine-saturated rock samples at different water-filled porosity (18%, 15.5%, and 7%) and water salinity (40Kppm, 80Kppm, 120Kppm, and 160Kppm) for Berea sandstone, A101.

ϕ_w (%)	40 Kppm	80 Kppm	100 Kppm	120 Kppm	160 Kppm
18	1.71	1.95	2.46	3.22	4.09
15.5	1.59	1.73	1.77	2.15	2.28
7	1.36	1.52	1.61	1.62	1.76

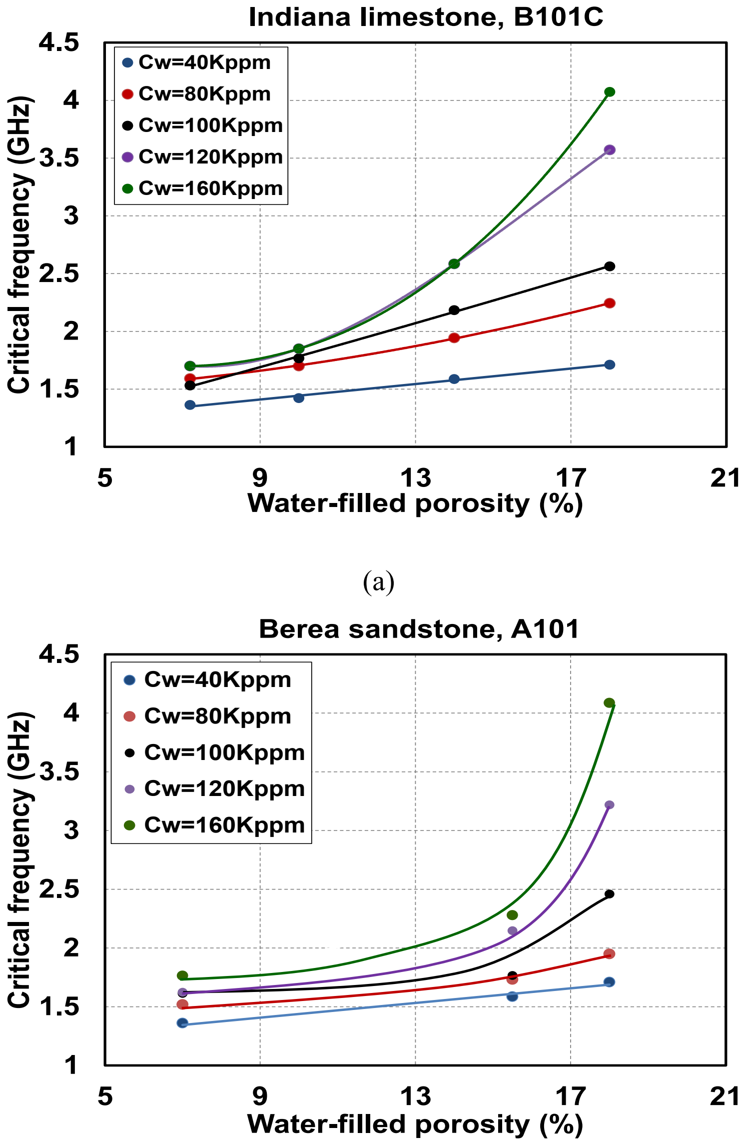

(a)

(b)

Figure 5.13: Critical frequency estimated for (a) Indianan limestone, B101C, and (b) Berea sandstones, A101, with water salinity of ranging from 40 Kppm to 160 Kppm and water-filled porosity of ranging from 7% to 18%. Blue, red, black, purple, and green lines represent 40 Kppm, 80 Kppm, 100 Kppm, 120 Kppm, and 160 Kppm water salinity, respectively.

5.4 Conclusions

This chapter documented experimental dielectric measurements and quantified the impact of water salinity on dielectric measurements in brine-saturated rock samples and brine. The measurement results in the case of brine confirmed that an increase of the water salinity increases the dielectric loss, but decreases the dielectric constant of brine. However, water salinity has only a small influence on the dielectric constant of saturated rocks. There exists a critical water-filled porosity below which the water salinity does not impact the dielectric constant of the brine-saturated rock samples. Variation of water salinity from 40 Kppm to 160 Kppm leads to a decrease from 14.4 to 13.1 of the dielectric constant (measured at 3 GHz) of Indiana limestone B101C, with 18% water-filled porosity. However, the salinity variation does not impact the dielectric constant in the case of 13.8% water-filled porosity. Similar results were observed in the cases of Indiana limestone B101A, and Berea sandstone A101, for which the impact of salinity on the dielectric constant is affected by water-filled porosity.

Furthermore, this chapter showed that water salinity substantially affects the dielectric loss of the saturated rock samples. The higher the water-filled porosity, the stronger the impact of water salinity on the dielectric loss. For instance, in the case of 18% water-filled porosity, an increase in water salinity from 40 Kppm to 120 Kppm increases the dielectric loss from 3.9 to 5.8 at 3 GHz for Indiana limestone B101C, and from 2.5 to 4.3 for Berea sandstone, A101. However, in the case of 7.8% and 7% water-filled porosity, the dielectric loss changes from 1.3 to 1.72 for Indiana limestone B101C, and from 1 to 1.85 for Berea sandstone A101, respectively. Additionally, at water salinity of above 120 Kppm (critical salinity), dissolved salt might begin to precipitate and cause a decrease in ionic conductivity. The critical water salinity might be higher than 120 Kppm in the subsurface at higher pressure and temperature than the surface, because an increase in pressure and temperature increases salt solubility in brine. The results also confirmed that both the dielectric constant and dielectric loss are influenced by water-filled porosity and frequency. For each level of water salinity, both the dielectric constant and dielectric loss decrease when water salinity and frequency increase (i.e., increase from 40 Kppm to 160 Kppm in water salinity and from 1 MHz to 3 GHz in frequency). The increase of the dielectric loss and dielectric constant is more significant at frequencies of less than 1 GHz.

Finally, it was observed that at certain water-filled porosity and water salinity, there exists a critical frequency above which interfacial polarization is minimal and dielectric constant remains constant. In the case of Indianan limestone B101C, at 40 Kppm water salinity, the variation of the water-filled porosity from 7.8% to 18% leads to an increase of critical frequency from 1.36 to 1.7 GHz, and in 18% water-filled porosity the change of water salinity from 40 Kppm to 160 Kppm results in the critical frequency varies from 1.71 to 4.07 GHz. Furthermore, it was observed that at 18% water-filled porosity and 80Kppm water salinity, the critical frequency of the Indian limestone B101C, and Berea sandstone A101, are 2.24 and 1.95, respectively. The results confirmed that the critical frequency of the brine-saturated rocks is affected by water-filled porosity and water salinity. Although porosity and salt concentration remained constant across the samples of Indian limestone B101C, and Berea sandstone A101, the critical frequency varied, confirming the impact of pore structure on critical frequency.

Based on these results and observations, we suggest the use of dielectric measurement frequency of higher than 1 GHz for reliable assessment of water-filled porosity, especially in cases of high water salinity (e.g., higher than 40 Kppm). Conventional application of frequencies of less than 1GHz for dielectric measurements can lead to significant errors in well-log-based assessment of water-filled porosity.

CHAPTER VI

SUMMARY, CONCLUSIONS, AND RECOMMENDATIONS

6.1 Summary

This dissertation quantified the impact of complex pore and grain structures on electrical resistivity and dielectric permittivity measurements of rock samples. Numerical simulation algorithms, methods, and workflows were developed to achieve the objectives of this dissertation. Through the quantification of these impacts, this dissertation proposed two models, a new dielectric permittivity model and a new joint interpretation model (combining dielectric permittivity and electrical resistivity measurements) to estimate water/hydrocarbon saturation. The two new models both take into account the spatial distribution of rock components and can provide better estimation of water/hydrocarbon saturation after comparison with conventional models like the CRIM. Furthermore, this dissertation designed and documented experiments to quantify the impact of water-filled porosity and salinity on the dielectric permittivity of brine-saturated rocks. Overall, the major contributions of this dissertation can be summarized in three stages.

The first stage (Chapter II and Chapter III) introduced diffusive directional tortuosity and directional connectivity to quantify the complexity of pore/grain network structure. In addition, a new dielectric permittivity model, which takes into account the spatial distribution of the pore/grain network, was developed to improve assessment of hydrocarbon/water saturation. The application of this new dielectric permittivity model on sandstone, carbonate, and synthetic organic-rich mudrocks confirmed that the new dielectric permittivity model is more reliable than the conventional CRIM method in the assessment of water/hydrocarbon saturation.

The second stage (Chapter IV) proposed a joint interpretation model through a combination of electrical resistivity and dielectric permittivity measurements to better estimate hydrocarbon/water saturation. This joint interpretation model is much more convenient to use than the new dielectric permittivity method proposed in Chapter III because it decreases the demand for calibration using abundant core measurements. The validation of this joint interpretation method was first established in the sandstone samples and further successively established in the organic-rich mudrock samples.

The last stage (Chapter V) designed experimental procedures to quantify the impact of water-filled porosity and salinity on the dielectric permittivity of brine-saturated rock samples. NMR, vacuum pressure/core flood systems, a centrifuge, and an impedance network analyzer were all used during these laboratory measurements. This experiment improves the understanding of the mechanism of dielectric permittivity within a broad frequency range. Ultimately, it can potentially improve the interpretation of dielectric permittivity measurements for reliable assessment of water-filled porosity.

6.2 Conclusions

6.2.1 Quantifying the directional connectivity of matrix constituents and its impact on the electrical resistivity of organic-rich mudrocks

i. Effective electrical resistivity of 3D pore-scale organic-rich mudrocks was successfully estimated through the developed simulation codes by using a finite difference method.

ii. Diffusive directional tortuosity and directional connectivity were introduced and estimated through the developed simulation codes by using a random walk algorithm.

iii. The impact of directional connectivity and diffusive directional tortuosity of mature kerogen and pyrite on the electrical resistivity of organic-rich mudrocks was quantified. The numerical simulation results confirmed that (a) the presence of conductive mature kerogen and pyrite networks impacts electrical resistivity along different directions and the corresponding estimation of the water/hydrocarbon saturation, (b) there is up to 31% and 37% variation in electrical resistivity caused by variation in directional connectivity (i.e., ranging from dispersed to layered distribution) of kerogen and pyrite networks.

iv. It was shown that the sensitivity of rock electrical resistivity to the kerogen network's directional connectivity is largely affected by the salt concentration of formation water. The increase in salt concentration decreases the sensitivity of electrical resistivity to the kerogen network's connectivity.

v. Interpretation of electrical resistivity measurement that takes into account the quantified directional connectivity of rock components at different scales can potentially improve accuracy in assessment of water/hydrocarbon saturation.

6.2.2 Pore-scale evaluation of dielectric measurements in formations with complex pore and grain structures

i. Effective dielectric permittivity of 3D pore-scale rocks in the frequency domain was successfully calculated through the developed simulation codes by using a finite difference method.

ii. The impact of pore and grain structures as well as anisotropic property on dielectric permittivity measurements of rocks were quantified by using the developed numerical simulators.

iii. It was observed that the directional permittivity of the same rock along three orthogonal directions can vary up to 16%, while the diffusive directional tortuosity changes from 1.9 to 3 in one of the sandstone samples. Compared with the tested sandstone samples, it was observed that pore space in tested carbonate samples is generally more tortuous than in sandstone samples.

iv. A new dielectric permittivity model was introduced to improve the assessment of water-filled porosity in formations with complex pore and grain structures.

Compared with the conventional CRIM, the new method can decrease the relative error in estimates of water-filled porosity from the largest relative error of approximately 27% (using the CRIM) to less than 10% relative error for both tested sandstone and carbonate samples.

v. The dielectric permittivity simulation of synthetic organic-rich much rocks revealed that (a) the presence of pyrite substantially impacts effective dielectric permittivity and water-filled porosity, and (b) the presence of the kerogen does not significantly impact the estimation of water-filled porosity.

6.2.3 Pore-scale joint evaluation of dielectric permittivity and electrical resistivity for assessment of hydrocarbon saturation using numerical simulations

i. Electrical directional tortuosity of the pore and grain network was successfully defined and calculated through a 3D pore-scale numerical simulation of electrical resistivity. The comparison between electrical directional tortuosity and diffusive directional tortuosity was conducted to confirm the applicability of the electrical directional tortuosity in describing the complexity of pore and grain structures.

ii. A new developed joint interpretation method that combines electrical directional tortuosity and dielectric permittivity was successfully developed to improve the accuracy of estimation of water-filled porosity and hydrocarbon saturation. Unlike conventional interpretation techniques for dielectric permittivity and electrical resistivity measurements, the new method takes into account the anisotropic properties of rock samples, such as directional tortuosity of conductive rock components.

iii. The new joint interpretation method was successfully applied in the actual digital sandstone and carbonate rock samples, as well as synthetic organic-rich mudrocks. For tested sandstone/carbonate samples, it was shown that the new method provides more reliable estimation of water-filled porosity with absolute relative errors within a 10% range, while the CRIM method can result in up to 30% error in estimating water-filled porosity. For organic-rich mudrock samples, it was shown that taking into account the structure of the pore and conductive components, such as pyrite, can provide better estimation of water saturation, with relative error within 10% and 3%, respectively, while the conventional CRIM method can result in a significantly larger error, up to 40% and 27%, respectively.

6.2.4 Impact of water salinity on high-frequency dielectric measurements in brine-saturated rocks

i. The impact of salinity on dielectric permittivity measurements of saline water was successfully quantified through laboratory measurements. The measurement results showed that the increase of water salinity increases dielectric loss, but decreases the dielectric constant of brine. At higher frequencies, the decrease in ion mobility results in more hydrated water molecules, leading to a decrease in the dielectric constant.

ii. The impact of salinity on dielectric permittivity measurements of brine-saturated rock samples was also quantified through laboratory measurements. It was shown that salinity has some impact on dielectric constant of brine-saturated rocks at higher water-filled porosity (greater than15 vol%), while its impact is negligible at lower water-filled porosity (less than 15 vol%) for all tested samples. It was also shown that water salinity substantially affects dielectric loss of the brine-saturated rock samples: the higher the water-filled porosity, the stronger the impact of the salinity on the dielectric loss of the brine-saturated rocks.

iii. The critical frequency of dielectric measurements, above which interfacial polarization is minimal, was defined and calculated by using a new developed method. It was shown that the critical frequency of dielectric measurements increases with the increase of both salinity and water-filled porosity of brine-saturated rocks. In the case of the Indiana limestone B101C (with 18% total porosity), it was observed that at 40-Kppm salinity, the increase of water-filled porosity from around 8% to 18% leads to an increase in critical frequency from 1.36 to 1.7 GHz, while in the case of 160 Kppm, the critical frequency increases from 1.71 to 4.07 GHz. It was also observed that the critical frequencies are different for the limestone B101C, and Berea sandstone A101, which have the same water-filled porosity and salinity, confirming the impact of pore structure on critical frequency.

iv. The critical water salinity of dielectric measurements at frequencies higher than the critical frequency is defined as the salinity above which dielectric loss begins to decrease as water salinity increases. It was shown that critical water salinity is equal to 120 Kppm for our tested samples under the ambient temperature and pressure. At water salinity above 120 Kppm, dissolved salt might begin to precipitate and cause a decrease in ionic conductivity. The critical water salinity might be even higher (e.g., greater than 120 Kppm) in the subsurface at higher pressure and temperature than the surface, because an increase in pressure and temperature increase salt solubility in brine.

v. Conventional application of frequencies of less than 1GHz for dielectric measurements might lead to significant errors in well-log-based assessment of water-filled porosity. The use of dielectric measurement frequency of higher than 1 GHz for reliable assessment of water-filled porosity is recommended, especially in cases of high water salinity conditions (e.g., greater than 40 Kppm).

6.3 Recommendations

This dissertation investigated the complexity of pore and grain structure and its impact on electrical resistivity and dielectric permittivity for both conventional and unconventional formations. However, there still remain many challenges in the petrophysics area that need to be addressed in the future. Here we discuss several recommendations for future research on the topic addressed in this dissertation.

i. Develop an upscaling technique for extrapolating petrophysical properties such as directional connectivity, tortuosity, and electrical and dielectric properties at pore-scale, core-scale, and log-scale for homogeneous and anisotropic formations.
ii. Apply the introduced electrical and dielectric models to the core-scale and log-scale measurements with the calibration of core-scale and log-scale measurements, find the correlation between tortuosity and tortuosity-dependent coefficient for different scales and different types of rocks, and apply this correlation as an input to the developed models to analyze the dielectric and electrical core-scale and log-scale measurements for estimating water-filled porosity.
iii. Integrate NMR measurements with electrical and dielectric measurements to more accurately estimate petrophysical properties such as water-filled porosity, pore geometry, wettability, and invasion-induced fluid impact.
iv. Incorporate the sonic log and laboratory measurements with electrical and dielectric measurements to more accurately characterize porosity, secondary porosity, anisotropic properties, geomechanical properties, and diagenesis processing of source rocks.
v. Carry out the electrical and dielectric measurements in the multi-frequency range to investigate the impact of clay and clay-bound water on the electrical and dielectric properties of organic-rich mudrocks, and further investigate the water-weakening mechanisms and their impact on petrophysical properties of rocks.

vi. Carry out dielectric measurements on kerogen, quantify the impact of kerogen maturity on its dielectric properties, and develop a better workflow for the reliable estimation of water-filled porosity in organic-rich mudrocks.

vii. Carry out multi-frequency dielectric measurements on brine-saturated rock samples under different temperature and pressure conditions, and quantify their impact on the dielectric properties of rocks.

ACRONYMS

3D	Three-Dimensional
CEC	Cation exchange capacity
CPMG	Carr-Purcell-Meiboom-Gill
CRIM	Complex refractive index model
CT	Computed tomography
FIB-SEM	Focused ion beam scanning electron microscope
GPIB	General regularly-distributed information in binary form
HC	Hydrocarbon
Kppm	Kilo parts per million
NMR	Nuclear magnetic resonance
SMD	Stroud-Milton-De
TOC	Total organic content

NOMENCLATURE

a	Archie’s factor，( )
C_k	Volumetric concentration of kerogen, (%)
C_p	Volumetric concentration of pyrite, (%)
Cw	Connate water salt concentration, (Kppm)
f	Frequency of dielectric measurements, Hz
f_g	Tortuosity-dependent coefficient for non-conductive grains
f_{HC}	Tortuosity-dependent coefficient for hydrocarbon
f_k	Tortuosity-dependent coefficient for kerogen network
f_{matrix}	Tortuosity-dependent coefficient for rock matrix
f_p	Tortuosity-dependent coefficient for the pyrite network
f_w	Tortuosity-dependent coefficient for the water network
h	Dimension of a cubic voxel, (m)
$i_\alpha(t)$	Position in i direction at time t for the α^{th} random walker
$i_\alpha(0)$	Initial position in i direction for the α^{th} random walker
l_X	Length of the digital rock sample in the X direction, (m)
l_Y	Length of the digital rock sample in the Y direction, (m)
l_Z	Length of the digital rock sample in the Z direction, (m)
m	Archie’s cementation exponent, ( )
M	Total number of the connected conductive clusters, ( )
n	Archie’s saturation exponent, ( )
N	Grid size in the digitized pore-scale rock images

R_t	Total electrical resistivity of the bulk rock
R_h	Electrical resistivity in the horizontal direction, (ohm-m)
R_v	Electrical resistivity in the vertical direction, (ohm-m)
R_w	Electrical resistivity of formation water
S_{HC}	Hydrocarbon saturation, (%)
S_w	Total water saturation, (%)
S_{wb}	Clay-bound water saturation, (%)
S_{wt}	Total water saturation, (%)
T_2	NMR spin-spin relaxation time, (ms)
TE	Inter-echo spacing time, (μs)
U	Electrical potential field, (V)
U_0	Initial electrical potential difference, (V)
v_k	Volume of kerogen, (m^3)
Va	Volume of air, (m^3)
$V_{HC,k}$	Volume of hydrocarbon inside kerogen pore space, (m^3)
$V_{HC,nk}$	Volume of hydrocarbon outside kerogen pore space, (m^3)
V_k	Volume of kerogen, (m^3)
V_R	Volume of rock, (m^3)
V_w	Volume of water, (m^3)
ε	Relative dielectric permittivity of rock
ε'	Real part of relative dielectric permittivity of rock
ε''	Imaginary part of relative dielectric permittivity of the rock

ε_0	Dielectric permittivity of the vacuum, (F/m)
ε_{eff}^{Y}	Effective dielectric permittivity along the Y direction
ε_g	Relative dielectric permittivity of non-conductive grains
ε_{HC}	Relative dielectric permittivity of hydrocarbon
ε_k	Relative dielectric permittivity of kerogen
ε_{matrix}	Relative dielectric permittivity of rock matrix
ε_p	Relative dielectric permittivity of pyrite
ε_w	Relative dielectric permittivity of water
ε_w'	Real part of relative dielectric permittivity of brine
ε_w''	Imaginary part of relative dielectric permittivity of brine
ω	Frequency of dielectric measurements, (Hz)
ϕ_{air}	Air-filled porosity of rock, (%)
ϕ_c	Interconnected porosity of rock, (%)
ϕ_k	Porosity of kerogen, (%)
ϕ_t	Total porosity of rock, (%)
ϕ_w	Water-filled porosity, (%)
σ	Electrical conductivity, (S/m)
σ_k	Electrical conductivity of kerogen network, (S/m)
σ_t	Total electrical conductivity of rock sample, (S/m)
$\sigma_{t,j}$	Electrical conductivity contributed by the *j*th conductive network, (S/m)
$\sigma_{t,w}$	Electrical conductivity contributed by water network, (S/m)

σ_w	Electrical conductivity of water network, (S/m)
Ψ_h	Directional connectivity in the horizontal direction
Ψ_i	Directional connectivity in the *i* direction
$\mathit{\Psi}_{j,i}$	Directional connectivity of the *j*th conductive component along the *i* direction (X, Y, or Z)
$\Psi_{k,h}$	Directional connectivity of kerogen network in the horizontal direction
$\Psi_{\mathrm{k,v}}$	Directional connectivity of kerogen network in the vertical direction
$\Psi_{p,h}$	Directional connectivity of pyrite network in the horizontal direction
Ψ_v	Directional connectivity in the vertical direction
τ	Electrical tortuosity
$\tau_{j,i}$	Electrical directional tortuosity of the *j*th conductive component along the *i* direction (X, Y, or Z)
τ_x	Electrical directional tortuosity in the direction X
τ_y	Electrical directional tortuosity in the direction Y
τ_z	Electrical directional tortuosity in the direction Z
$\tilde{\tau}$	Diffusive tortuosity
$\tilde{\tau}_h$	Diffusive directional tortuosity in the horizontal direction
$\tilde{\tau}_i$	Diffusive directional tortuosity along the *i* direction
$\tilde{\tau}_{j,i}$	Diffusive directional tortuosity of the *j*th conductive component

	along the *i* direction (X, Y, or Z)
$\tilde{\tau}_{k,h}$	Diffusive directional tortuosity of kerogen network in the horizontal direction
$\tilde{\tau}_{k,v}$	Diffusive directional tortuosity of kerogen network in the vertical direction
$\tilde{\tau}_{v}$	Diffusive directional tortuosity in the vertical direction
$\tilde{\tau}_{w,i}$	Diffusive directional tortuosity of the water network along the *i* direction (X, Y, or Z)

REFERENCES

Abraitis，P.K., Pattrick，R.A.D., and Vaughan，D.J. (2004). Variations in the compositional, textural, and electrical properties of natural pyrite: A review. International Journal of Mineral Processing 74(1:4): 41–59.

Alfred, D. and Vernik, L. (2013). A new petrophysical model for organic shales. Petrophysics 54(3): 240–247.

Archie， G.E. (1942). The electrical resistivity log as an aid in determining some reservoir characteristics. Transactions of the American Institute of Mining Metallurgical Engineers 146(1): 54–62.

Baea，W., Sungb， W., Kimb， S., and Jeona， E. (2006). The effects of macropores in heterogeneous porosity systems on electrical resistivity behavior. Energy Sources, Part A: Recovery, Utilization, and Environmental Effects 28(9): 793-806.

Binley, A., Winship, P., Middleton, R., Pokar, M., and West, J. (2001). High resolution characterization of vadose zone dynamics using cross-borehole radar. Water Resources Research 37(11): 2639–2652. doi:10.1029/2000WR000089.

Birchak, J.R., Gardner, C.G., Hipp, J.E., and Victor, J.M. (1974). High dielectric constant microwave probes for sensing soil moisture. Proceedings of the IEEE 62(1): 93–98.

Bittar, M., Li, J., Kainer, G., Cherry, R., Torres, D., Coy, D.M. (2010). A modern microwave formation evaluation sensor and its application in reservoir evaluation. SPWLA 51th Annual Well Logging Symposium, Perth, Australia, June 19–23.

Bond, C. (2011). An efficient and versatile flood fill algorithm for raster scan displays. PDF file. http://www.crbond.com/papers/fldfill_v2.pdf

Brovelli, A. and Cassiani, G. (2011). Combined estimation of effective electrical conductivity and permittivity for soil monitoring. Water Resources Research 47(8): W08510. doi: 10.1029/2011WR010487.

Burdette, E.C., Cain, F.L., and Seals, J. (1980). In Vivo Probe Measurement Technique for Determining Dielectric Properties at VHF Through Microwave Frequencies. IEEE Transactions on Microwave Theory and Techniques 28(4): 414–427.

Bussian, A.E. (1983). Electrical conductance in a porous medium. Geophysics 48(9): 1258–1268.

Calvert, T.J. and Wells, L.E. (1977). Electromagnetic propagation: a new dimension in Logging. SPE California Regional Meeting, Bakersfield, California, USA, April 13-15.

Chandra, A. and Bagchi, B. (2000). Frequency dependence of ionic conductivity of electrolyte solutions. Journal of Chemical Physics 112(4): 1876–1886.

Chen, H., Firdaus, G., and Heidari, Z. (2014). Impact of anisotropic nature of organic-rich mudrocks on electrical resisitivity measurements. SPWLA 55th Annual Well Logging Symposium, Abu Dhabi, UAE, May 18–22.

Chen, H. and Heidari, Z. (2014). Pore-scale evaluation of dielectric permittivity of rock-fluid mixture with complex pores and grain structures. Petrophysics 55(6): 587–597.

Clavier, C., Coates, G., and Dumanoir, J. (1984). Theoretical and experimental bases for the dual-water model for the interpretation of shaly sands. Society of Petroleum Engineers Journal 24(2): 153–168.

Clennell, M.B., Josh, M., Esteban, L., Piane, C.D., Schmid, S., Verrall, M., Hill, D., Woods, C., and McMullan, B. (2010). The influence of pyrite on rock electrical properties: A case study from NW Australian gas reservoirs. SPWLA 51st Annual Logging Symposium, Perth, Australia, June 19–23.

Curtis, M.E., Ambrose, R.J., and Sondergeld, C.H. (2010). Structural characterization of gas shales on the micro- and nano-scales. SPE Canadian Unconventional Resources and International Petroleum Conference, Calgary, Alberta, Canada, Octorber 19-21.

Dahlberg, K.E. and Ference, M.V. (1984). A quantitative test of the electromagnetic propagation (EPT) log for residual oil determination. SPWLA 25th Annual Logging Symposium, New Orleans, Louisiana, USA, June 10–13.

Dobson, M.C., Ulaby, F.T., Hallikainen, M.T., and El-Rayes, M.A. (1985). Microwave dielectric behaviour of wet soils – part II: dielectric mixing models. IEEE Transactions on Geoscience and Remote Sensing 23(1): 5–46.

Donadille, J.M. and Faivre, O. (2015). Water complex permittivity model for dielectric logging. SPE Middle East Oil & Gas Show and Conference, Manama, Bahrain, March 8–11.

Dong, H. (2007). Micro-CT imaging and pore network extraction: Ph.D. Dissertation. Imperial College London, London, UK.

Doveton, J.H. (1994). Geological log interpretation: Reading the rocks from wire-line logs: SEPM Short Course 29: 169.

Ellis， M., Sinha, M., and Parr, R. (2010). Role of fine-scale layering and grain alignment in the electrical anisotropy of marine sediments. First Break 28(9): 49–57.

Falkenhagen, H. (1931). The principal ideas in the interionic attraction theory of strongelectrolytes. Review of Modern Physics 3(3): 412–426.

Feng, S. and Sen, P.N. (1985). Geometrical model of conductivity and dielectric properties of partially saturated rocks. Journal of Applied Physics 58(8): 3236–3243.

Garing, C., Luquot, L., Pezard, P., Gouze, P. (2014). Electrical and flow properties of highly heterogeneous carbonate rocks. Bulletin of the American Association of Petroleum Geologists 1(98): 49–66.

Gilmore, R.J., Clark, B., and Best, D. (1987). Enhanced saturation determination using the EPT-G endfire antenna array. SPWLA 28th Annual Logging Symposium, London, England, June 29–July 2.

Hamed, Y., Persson, M., and Berndtsson, R. (2003). Soil solution electrical conductivity measurements using different dielectric techniques. Soil Science Society of America Journal 67(4): 1071–1078.

Heidari, Z. and Torres-Verdín, C. (2012). Estimation of dynamic petrophysical properties of water-bearing sands invaded with oil-based mud from multi-physics borehole geophysical measurements. Geophysics 77(6): 209–227.

Heimovaara, T.J., Bouten, W., and Verstraten, J.M. (1994). Frequency domain analysis of time-domain reflectometry waveforms: a four component complex dielectric mixing model for soils. Water Resources Research 30(2): 201–209. doi: 10.1029/93WR02949.

Hizem, M., Budan, H., Deville, B., Faivre, O., Mosse, L., and Simon, M. (2008). Dielectric dispersion: A new wireline petrophysical measurement. SPE Annual Technical Conference and Exhibition, Denver, Colorado, USA, September 21–24.

Jouniaux L., Zamora M., and Reuschlé T. (2006). Electrical conductivity evolution of non-saturated carbonate rocks during deformation up to failure. Geophysical Journal International 167(2): 1017–1026.

Kethireddy, N., Chen H., and Heidari Z. (2014). Quantifying the effect of kerogen on resistivity measurements in organic-rich rocks. Petrophysics 55(2): 136–146.

Kimmich, R. (1997). NMR: Tomography, diffusometry, relaxometry. Berlin Heidelberg: Springer-Verlag.

Klein, L. A. and Swift, C. T. (1977). An improved model for the dielectric constant of sea water at microwave frequencies. IEEE Transactions on Antennas and Propagation 25(1): 104–111.

Lane, J.A. and Saxton, J.A. (1952). Dielectric dispersion in pure polar liquids at very high radio frequencies. III. The effect of electrolytes in solution. Proceedings of Royal Society 214(1119): 531–545.

Lasne, Y., Paillou, P., Freeman, A., Farr, T., McDonarld, K.C., Ruffie, G., Malezieux, J.M., Chapman, B. and Demontoux, F. (2008). Effect of salinity on the dielectric properties of geological materials: Implication for soil moisture detection by means of radar remote sensing. IEEE Transactions on Geoscience and Remote Sensing 46(6): 1674–1688.

Lawrence, K.C., Windham W.R., and Nelson S.O. (1998). Wheat moisture determination by 1 to 110MHz swept frequency admittance measurements. Transactions of the ASAE 4(1): 135–142.

Leung, P.K. and Steiger, R.P. (1992). Dielectric Constant Measurements: A new, rapid method to characterize shale at the wellsite, IADC/SPE Drilling Conference, New Orleans, Louisiana, USA, February 18–21.

Li, L., Meller G., and Kosina, H. (2007). Temperature and field-dependence of hopping conduction in organic semiconductors. Microelectronics Journal 38(1): 47–51.

Linde, N., Binley, A., Tryggvason, A., Pedersen, L.B., and Revil, A. (2006). Improved hydrogeophysical characterization using joint inversion of cross-hole electrical resistance and ground-penetrating radar traveltime data. Water Resources Research 42(12): W12404. doi:10.1029/2006WR005131.

Moore, C. H. (2001). Carbonate resevoirs: Porosity evolution and diagenesis in a sequence-stratigraphic framework. Developments in Sedimentology, 55.

Malicki, M.A. and Walczak, R.T. (1999). Evaluating soil salinity status from bulk electrical conductivity and permittivity. Eur. J. Soil Sci. 50 (3): 505–514.

Mao, J., Fang, X., Lan, Y., Schimmelmann, A., Mastalerz, M., Xu, L., and Schmidt-Rohr, K. (2010). Chemical and nanometer-scale structure of kerogen and its change during thermal maturation Investigated by advanced solid-state 13C NMR spectroscopy. Geochimica et Cosmochimica Acta 74(7): 2110–2127.

Meng, D., Ma, T.M., Geng, C.W., and Sun, Y. (2012). Test method and experimental research on resistance of oil shale under high temperature. Global Geology 15(3): 245–251.

Miller, M.N. (1969). Bounds for effective electrical, thermal, and magnetic properties of heterogeneous materials. Journal of Mathematical Physics 10(11): 1988–2004.

Musharfi, N., Almarzooq, A., Eid, M., Quirein, J., Witkowsky, J., Buller, D., Rourke, M., Truax, J., and Praznik, G. (2012). Combining wireline geochemical, NMR, and dielectric data for formation evaluation and characterization of shale reservoirs. SPWLA 53rd Annual Logging Symposium, Cartagena, Colombia, June 16–20.

Myers, M.T. (1991). A saturation interpretation model for the dielectric constant of shaly sands. 5th Annual Society of Core Analysts Conference, San Antonio, Texas, USA, August 20–21.

Myers, M. T. (1996). Pore geometry dependent dispersion model for the dielectric constant. Society of Core Analysts Conference, Washington, D.C., USA, July 18–21.

Nabawy B.S., Rochette P., Géraud, Y. (2010). Electric pore fabric of the Nubia sandstones in south Egypt: characterization and modelling. Geophysical Journal International 183(2): 681–694.

Nakashima, Y. and Kamiya, S. (2007). Mathematica programs for the analysis of three-dimensional pore connectivity and anisotropic tortuosity of porous rocks using X-ray computed tomography image data. Journal of Nuclear Science and Technology 44(9): 1233–1247.

Nelson, S.O. (1991). Dielectric properties of agricultural products measurements and applications. IEEE Transactions on Electrical Insulation 26(5): 845-869.

Passey, Q.R., Bohacs, K., Esch, W.L., Klimentidis, R., and Sinha, S. (2010). From oil-prone source rock to gas-producing shale reservoir – geologic and petrophysical characterization of unconventional shale gas reservoirs. SPE International Oil and Gas Conference and Exhibition, Beijing, China, June 8–10.

Pfleiderer, S. and Halls, H. C. (1990). Magnetic susceptibility anisotropy of rocks saturated with ferrofluid: A new method to study pore fabric. Physics of the Earth and Planetary Interiors 65(1 and 2): 158–164.

Pirrone, M., Han, M., Bona, N., Borghi, M., Galli, M. T., Pampuri, F., Faivre, O., Hizem, M., Kerroubi, J., and Mossé, L. (2011). A novel approach based on dielectric dispersion measurements to evaluate the quality of complex shaly-sand reservoirs. SPE Annual Technical Conference and Exhibition, Denver, Colorado, USA, October 30–November 2.

Press, W., Teukolsky, S.A., Vetterling, W.T., and Flannery, B.P. (2007). Numerical recipes in C: the art of scientific computing (3rd ed.). New York: Cambridge University Press. ISBN 978-0-521-88068-8.

Pride, S. (1994). Governing equations for the coupled electromagnetics and acoustics of porous media. Physics Review Bulletin 50: 15678–15696.

Quirein, J.A., Murphy, E.E., Praznik, G., Witkowsky, J.M., Shannon, S., and Buller, D. (2012). A comparison of core and well log data to evaluate porosity, TOC, and hydrocarbon volume in the Eagle Ford shale. SPE Annual Technical Conference and Exhibition, San Antonio, Texas, USA, October 8–10.

Rajeshwar K., Das M., and Dubow J. (1980). D.C. electrical conductivity of Green River oil shales. Nature 287:131–133.

Rankin, D. and Sing, R.P. (1985). Effect of clay and salinity on the dielectric properties of rock. Journal of Geophysical Research 90(B10): 8793–8800.

Roth, K., Schulin, R., Fluhler, H., and Attinger, W. (1990). Calibration of time domain reflectometry for water content measurement using a composite dielectric approach. Water Resources Research 26(10): 2267–2273. doi:10.1029/90WR01238.

Schmitt, D.P., Al-Harbi, A., Saldungaray, P., Akkurt, R., and Zhang, T. (2011). Revisiting Dielectric Logging in Saudi Arabia: Recent experiences and applications in development and exploration wells. SPE/DGS Saudi Arabia Section Technical Symposium and Exhibition, Al-Khobar, Saudi Arabia, May 15–18.

Seleznev, N., Habashy, T.M., Boyd, A.J., and Hizem, M. (2006). Formation properties derived from a multi-frequency dielectric measurement. SPWLA 47th Annual Logging Symposium, Veracruz, Mexico, June 4–7.

Seleznev, N.V., Kleinberg, R.L., Herron, M.M., Machlus, M., Pomerantz, A.E., Reeder, S.L., and Allix, P.C. (2011). Applications of dielectric dispersion logging to oil shale reservoirs SPWLA 52nd Annual Logging Symposium, Colorado Springs, Colorado, USA, May 14–18.

Schlumberger. (1972). Log interpretation, Vol. I: Principles: New York, Schlumberger Limited: 113.

Schlumberger. (1974). Log interpretation, Vol. II: Applications: New York, Schlumberger Limited: 116.

Sen, P.N. (1981a). Relation of certain geometrical features to the dielectric anomaly of rocks. Geophysics 46(12): 1714–1720.

Sen, P.N. (1981b). Dielectric anomaly in inhomogeneous materials with application to sedimentary rocks. Applied Physics Letter 39(8): 667–668.

Sen, P.N. (1984). Grain shape effects on dielectric and electrical properties of rocks, Geophysics 49(5): 586–587.

Sen, P.N., Scala, C., and Cohen M.H. (1981). A self-similar model for sedimentary rocks with application to the dielectric constant of fused glass beads. Geophysics 46(5): 781–795.

Shao, Y., Hu, Q., Guo, H., Lu, Y., Dong, Q., and Han, C. (2003). Effect of dielectric properties of moist salinized soils on backscattering coefficients extracted from RADARSAT Image. IEEE Transactions on Geoscience and Remote Sensing 41(8): 1879–1888.

Siegesmund, S., Kern, H., and Vollbrecht, A. (1991). The effect of oriented microcracks on seismic velocities in an ultramylonite. Tectonophysics 186(3,4), 241–251.

Stroud, D., Milton, G.W., and De, B.R. (1986). Analytical model for the dielectric response of brine-saturated rocks. Physics Review B 34(8): 5145–5153.

Stuchly, M.A., and Stuchly, S.S. (1980). Coaxial Line Reflection Methods for Measuring Dielectric Properties at Radio and Microwave Frequencies–A Review. IEEE Transactions on Instrumentation and Measurement 29(3):176–183.

Teheran, M.R., Kenyon, W.E., and Safinya, K.A. (1990). Measurement of dielectric response of water-saturated rocks. Geophysics 50(12): 1530–1541.

Toumelin, E. and Torres-Verdin, C. (2009). Pore-scale simulation of KHz-GHz electromagnetic dispersion of rocks: effects of rock morphology, pore connectivity, and electrical double layers. SPWLA 50th Annual Logging Symposium, Woodlands, Texas, USA, June 21–24.

Verwer, K., Eberli, G.P., and Weger R.J. (2011). Effects of pore structure on electrical resistivity in carbonates. AAPG Bulletin, 95(2): 175–190. doi:10.1306 /06301010047.

Walters, C.C., Kliewer, C.E., Awwiller, D.N., Rudnicki, M.D., Passey, Q.R., and Lin, M.W. (2014). Influence of turbostratic carbon nanostructures on electrrical conductivity in shales. International Journal of Coal Geology 122 (1): 105–109.

Waxman M.H. and Smits L.J. (1968). Electrical conductivities in oil-bearing shaly sand. SPE Journal 8(2): 107–122.

Wei, Z.B., Gao, X.X., Zhang, D.J., and Da, J., (2005), Assessment of thermal evolution of kerogen geopolymers with their structural parameters measured by solid-state C-13 NMR spectroscopy: Energy & Fuels 19: 240–250.

West J.L., Handley K., Huangye Y., and Pokar M. (2003). Radar frequency dielectric dispersion in sandstone: Implications for determination of moisture and clay content. Water Resources Research 39 (2): 1026-1037. doi:10.1029/2001WR000923.

Wharton, R.P., Hazen, G.A., Rau, R.N., and Best, D.L. (1980). Electromagnetic propagation logging, Advances in technique and interpretation. SPE Annual Technical Conference and Exhibition, Dallas, Texas, USA, 21-24 September, SPE-9267-MS.

Winsauer W.O., Shearin H.M., Masson P.H., and Williams M. (1952). Resistivity of brine-saturated sands in relation to pore geometry. Bulletin of the American Association of Petroleum Geologists 36(2): 253–277.

Wong, P., Koplik, J., and Tomanic, J.P. (1984). Conductivity and permeability of rocks. Physics Review B 30(11): 6606–6614.

Wu, Y., Wang, W., Zhao, S., and Liu, S. (2015). Dielectric properties of saline soil and an improved dielectric model in C-Band. IEEE Transactions on Geoscience and Remote Sensing 53(1): 440–452.

Young, D. (1954). Iterative methods for solving partial difference equations of elliptic type. Trans. Amer. Math. Soc. 76: 92–111.